



Characterization of metals for Cochlear Implants

Joost van Driel, BSc
#1322621

Daily supervisor:
Nishant Lawand, MSc.
Supervisor:
Prof. Dr. Paddy French

April 25, 2013

CHARACTERIZATION OF METALS FOR COCHLEAR IMPLANTS

Thesis

submitted in partial fulfillment of the requirements for the degree of

MASTER OF SCIENCE

in

ELECTRICAL ENGINEERING

in the department of Microelectronics, EEMCS

by

Joost Willem van Driel

Committee members:

Prof. Dr. P.J. French (TU Delft: Electronic Instrumentation Laboratory)

Dr. A. Bossche (TU Delft: Electronic Instrumentation Laboratory)

Dr. ir. J.F.L. Goosen (TU Delft: Precision and Microsystems Engineering Department)

N.S. Lawand, MSc. (TU Delft: Electronic Instrumentation Laboratory)

Electronic Instrumentation Laboratory

Faculty of Electrical Engineering, Mathematics and Computer Science

Delft University of Technology

Abstract

The need for Cochlear Implants (CI's) with improved functionality and quality requires new techniques to be used to manufacture the electrode array. Titanium nitride (TiN) is one of the contenders for use as metal in the future CI's, but its characteristics need to be verified, measured and tested. A metal should comply to certain requirements like the ability to deliver enough charge to the nerve ending in the saline environment of the cochlea. TiN is able to withstand a high current density ($2.8 \frac{mA}{\mu m^2}$), while aluminium failed due to electromigration; even when coated with TiN. The resistance of a $10mm$ long and $5\mu m$ wide track decreases from $1.08 \cdot 10^4 \Omega$ to $6.9 \cdot 10^2 \Omega$ when a combination of Al and TiN is made. This solves the reasonably high resistance of TiN. The self-heating and the change in resistance due to temperature changes (TCR) are measured, because the amount of dissipated heat should stay as low as possible. TiN has a low TCR, $5.9 \cdot 10^{-4}$. Furthermore, the metal must not dissolve in the environment, which can be checked by a (cyclic) voltammetry and by endurance tests. TiN was able to withstand the harsh tests. The improved functionality and quality asks for the addition of transistors to the electrode array. Furthermore, this thesis shows that it is possible to create working npn, NMOS and PMOS transistors with TiN using only 5 masks.

Acknowledgments

This thesis could not be realized without the help of multiple people. First of all, I like to thank Piet Trimp for his technical expertise and help with finding the correct measurement equipment. Secondly, Nishant Lawand for the supply of a large amount of papers and reading material, the design and fabrication of the test dies and correcting of the thesis. Henk van Zeijl was also a big help while doing my graduation project, because of his enthusiasm about the BiCMOS process. I would also like to thank Paddy French for his mental support during the project and for his stimulation to write papers so I could go to a conference in Milan. My family helped with finding grammatical errors and corrected them. Finally, I would like to thank all of the other supporting staff of the Electronic Instrumentation department and my friends at the Electrotechnische Vereeniging for their support.

Contents

Abstract	i
Acknowledgments	ii
1 Introduction	1
2 Background	4
2.1 The anatomy of the human ear	4
2.1.1 External ear	4
2.1.2 Middle ear	5
2.1.3 Internal ear	7
2.2 Cochlear implants	10
2.3 Electrode array design	13
2.3.1 Stiff design	13
2.3.2 Flexible design	15
2.4 Electromigration	16
2.5 BiCMOS process	17
3 Metal requirements	21
3.1 Charge transfer	21
3.1.1 Electromigration	22
3.1.2 TCR	23
3.1.3 Electric field distribution	24
3.2 Biocompatibility	24
3.2.1 Voltammetry	25
3.2.2 Endurance tests	27
3.3 Logic implementation	27
4 Measurements and simulations	28
4.1 Test die	28
4.2 Impedance	32
4.3 Joule heating	34
4.4 TCR	36
4.5 Electromigration	37
4.6 Electric field	39
4.7 Voltammetry	43
4.8 Endurance	43
4.9 BiCMOS	48

4.9.1	Sheet resistance	48
4.9.2	Contact resistance	49
4.9.3	NPN transistor	50
4.9.4	NMOS transistor	52
4.9.5	PMOS transistor	53
4.9.6	Inverter	54
4.9.7	Oscillator	55
5	Conclusions and future work	56
A	Material properties	59
A.1	Cochlear fluids	59
A.2	Metals	60
B	Anatomical terms	61
C	BiCMOS process layout	62
D	Additional figures for chapter 4	71
D.1	Al-TiN delamination	71
D.2	TCR graphs	73
D.3	Electromigration	76
D.4	Endurance test	77
D.5	BiCMOS	78
	Bibliography	78

Chapter 1

Introduction

Deafness and impaired hearing has been a common disorder throughout the centuries. They can occur due to exposure to high frequency noise or diseases. Mild hearing loss can be compensated by using a passive or behind-the-ear hearing aid, but the more severe deficiencies did not have a solution up till the discovery of implantable hearing aids. The Cochlear Implants (CI's) are for people that have no or very little sense of hearing. Successful implants have been done on both children and adults. The user experience quality of the current devices is however not very good. Users are able to understand conversations from one person to another in a quiet area, but this is not possible in for example a cocktail bar. Current devices are hand-made and this limits the number of electrodes, which then limits the number of tones that can be perceived. A new method of fabrication needs to be found to increase the amount of electrodes.



(a) Collapsible metal ear trumpet, made between 1855 and 1866 (b) Hard rubber speaking tube (conversation tube) of $38\frac{1}{2}$ " long, made around 1880

Figure 1.1: Passive hearing aids were the first hearing aids, pictures taken from [1].

There have been a lot of different hearing aids throughout history. It started with passive amplifiers: devices that increase the surface of the external ear and guide the sound to the auditory canal. The ear trumpet (figure 1.1a) and speaking tube (figure 1.1b) are two examples of such passive amplifiers. There are also reports of Zeppelins that use speaking tubes as intercom. These passive devices did however become too big when large amplification was needed and with the discovery of electricity new methods were found.

The first electric hearing aid that was developed in the early 1900s used carbon microphones, which were also used in the first telephones. Small carbon balls that conduct current are com-

pressed and decompressed by a diaphragm that vibrates due to sound. When compressed, more current can flow through the balls, because there are more paths from the top of the reservoir to the bottom. The sound that was produced by the first carbon microphone was however noisy and not very loud, so many people still used passive amplifiers. The discovery of the vacuum tube in 1906 did not change this much, due to the bulky nature of these new devices. Table models (introduced in 1921) were the only feasible versions until 1940, when miniature vacuum tubes were introduced on the market. That was the first year that real body-worn hearing aids were used. Two large batteries were needed to power the filaments and to power the plates and that made it very bulky.

The transistor was invented in 1948 by Bell Labs and this was quickly used in hearing aids. The first hearing aid that used a transistor was an hybrid one, using both transistors and vacuum tubes which reduced the battery life a lot. This hybrid was introduced in 1952 and the first full transistor hearing aid, called the ‘Transit-Ear’, hit the market in January of 1953. Many other models followed soon after that and the size reduced, while the functionality increased over the years. The hearing aids that are used now are mostly digital, meaning that the signals that enter the device are processed digitally. This increases the quality of the user experience, because it is possible to filter the piece of the auditory spectrum that is wanted.

CI’s were introduced in the 1970s on an experimental basis. These first devices only had a single channel, multi-channel implants were introduced in 1984, the same year that CI’s received the FDA (Food and Drug Administration) approval. From that year, the development of cochlear implants has not stood still. The number of electrodes increased, the reliability and quality improved and the devices were reduced in their dimensions. There are also other types of implantable hearing aids, like the Bone Anchored Hearing Aid (Baha[®]) or Electro-acoustic implant (both from Cochlear[®]) or the still experimental deep-brain stimulator. The first uses bone to transfer sound, bypassing the outer and middle ear, while the second works like a non-implantable hearing aid, only now it is implanted in the middle ear.

A CI consists of multiple parts, as shown in figure 1.2. The sound is converted to electrical signals using the microphone, which sends it to the sound processor. The processor used to be a large body-worn packet, but it is already possible to have just an ‘in the Ear Canal’ or Behind-the-Ear microphone with a sound processor as shown in figure 1.2. These systems also have for example, Bluetooth connectivity and an MP3-player. The processed sound signals are sent to the headpiece at the outside, which are then send wireless through the skin to the receiver/stimulator (‘Implant’ in figure 1.2). This device is also powered using this wireless link and it decodes the incoming signals into signals that can be applied to the last component: the electrode array. It depends on the manufacturer what architecture is used for the stimulator circuitry, but it is for example possible to have a current source per channel or one that is switched between channels. The electrode array delivers the charge to the nerve endings in the cochlea.

The previous paragraph already showed that the development of the CI’s has been going on since its discovery, because the bulky body-worn sound processor has for example been replaced by a much smaller and more functional device. The development will however not stop with these improvements. Companies, institutes and universities are researching the future of the CI.

The begin of this introduction described the problem that is dealt with in this thesis. The Electrical Engineering department of Delft University of Technology is researching CI’s with three different groups. The three topics are: the software of the sound processor, the (analog) stimulator circuitry and the electrode array. The latter is the research topic of the Electronic Instrumentation Laboratory: the department of the author of this thesis. It is in cooperation with

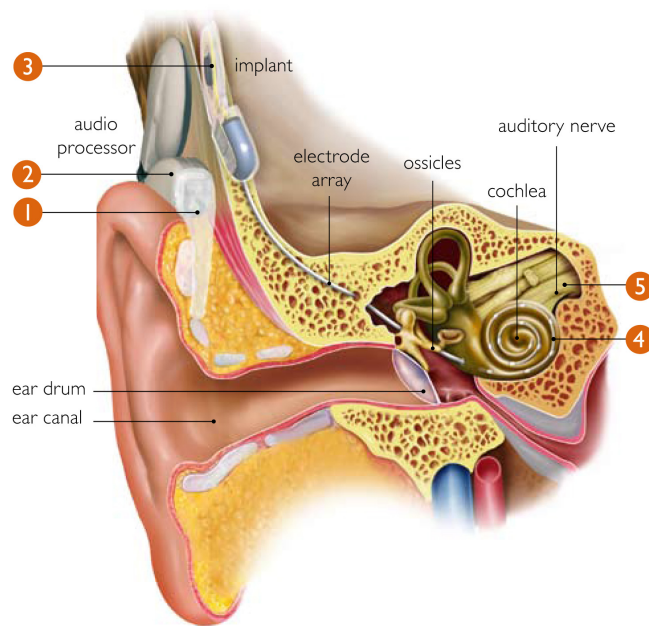


Figure 1.2: Overview of an Med-El Cochlear Implant

STW (funding agency in The Netherlands) and Advanced Bionics in the USA (user company) under the project called as SMAC-it. In the current technology the electrode arrays are hand-assembled Platinum-Iridium wires welded to Platinum strips as stimulation sites, which are then completely coated with silicone rubber for biocompatibility. These electrode arrays are limited in electrode count (16-32), due to their large size relative to the size of scala tympani (ST) of the cochlea. With lithography and biocompatible materials it is possible to create electrode arrays with much more electrodes and functionality than the devices that are available now.

There are other areas for the device that need to be researched, for example the shape, the materials, the added functionality and the number and placement of the electrodes. This thesis describes the measurements and tests needed for the characterization of the possible metal candidates for the electrode array of the cochlear implant. The material properties of Pt and Pt/Ir for long term working stability could not withstand the harsh environment inside the cochlea. Titanium nitride (TiN) is a biocompatible metal which is used in pacemakers already and it is possible to process it using these techniques. All the measurements and tests described in this thesis have been done with TiN. Other metals that have been considered are Titanium and Aluminium and combinations of them. The harsh environment of the cochlea can have a large (negative) influence on the electrode array and the other way around.

The anatomy and the sound waves pathway of a correctly working human ear are shown in the first part of chapter 2. The remainder of that chapter describes the electrode array in more detail, the phenomenon called electromigration and the BiCMOS (Bipolar/CMOS transistors) process. Chapter 3 lists what requirements needed to be fulfilled by the metal to be implemented for the fabrication of the electrode array. The thread through that chapter are the different measurements and tests that need to be done. The test and measurement results are shown and explained in chapter 4. The conclusions that can be drawn and what needs to be done after this thesis are combined in chapter 5.

Chapter 2

Background

This chapter describes the knowledge that is needed to understand this thesis. The first section shows the anatomy of the human ear and how the sound waves travel from the air to the brain. The next section explains the basic working of a Cochlear Implant (CI), while the following section is about the current research on the implanted part of the CI: the electrode array. After that the phenomenon of electromigration is described and how it affects metal. The last section is about the BiCMOS process which will be discussed further in the next chapters.

2.1 The anatomy of the human ear

The auditory system is responsible for the (correct) perception of sound, one of the five basic senses of the human body. This section deals with the human auditory system in general and more specific with the ways this system can be affected resulting in the deterioration or even loss of hearing. The information given in this section is based on [2], [3], [4] and [5].

2.1.1 External ear

The auditory system converts audible vibrations which enter the ear and are then converted into nerve impulses that are perceived by the auditory cortex of the brain. The external ear consists of the auricle (or pinna) and the external auditory canal, with the latter being separated from the middle ear by the tympanic membrane (or eardrum). The function of the external ear is to collect the external sound waves, which cause vibrations to the tympanic membrane. These vibrations are transmitted across the middle ear by a chain of ossicles (small bones): the malleus, incus, and stapes which will be described in more detail in the next section 2.1.2 about the middle ear. The middle ear acts as an amplifier that amplifies these sound waves (vibrations) which are fed to the cochlea (internal ear section 2.1.3) which converts these amplified sound vibrations into an electrical neural signal which is carried by the auditory nerve to the brain. A schematic representation of the human ear is shown in figure 2.1.

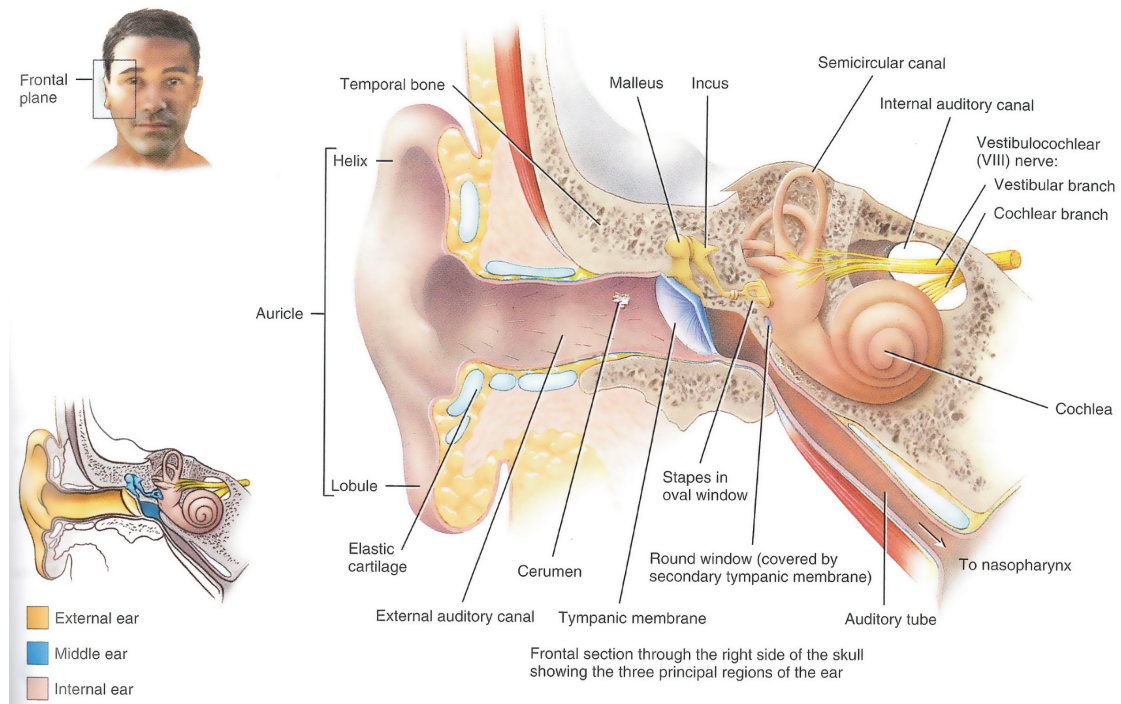


Figure 2.1: Frontal section through the right side of the skull showing the three principal regions of the ear. Reprinted with permission, figure 17.18 from [4]

2.1.2 Middle ear

The middle ear (otitis media) is an air-filled cavity which is embedded in the temporal bone. It is separated from the external ear by the eardrum and is connected to the inner ear by two membrane-covered openings in the cochlea: the oval and round window. There is also a connection to the top of the throat: the Eustachian tube. A schematic overview of the middle ear is shown in figure 2.2.

The eardrum, or tympanic membrane, transports the sound waves coming from the external ear canal to the middle ear by vibrating at the same frequency. These vibrations are then picked up by the ossicles. The ossicles are the three small bones that connect the eardrum to the cochlea: the hammer (malleus), the anvil (incus) and stirrup (stapes), in that order. The ‘footplate’ of the stirrup fits into the oval window (fenestra vestibulae) of the cochlea. This pathway will act as an amplifier in order to have a sufficient amount of signal to bridge the air-fluid border in the cochlea. Another pathway runs through the temporal bone, the portion of the skull that houses the auditory system. This does not have the amplification of the other pathway, thus the signal that finally reaches the fluid in the cochlea is weak. It does not contribute significantly to the final signal and is thus not of interest. There are, however, Bone Anchored Hearing Aids for people with a damaged middle or outer ear. In that case, the only pathway to the cochlea is the temporal bone. It works like a regular hearing aid, but the speaker that is normally placed in the auricle is replaced with a screw in the temporal bone.

Apart from the bones there are also two muscles: the tensor tympani and the stapedius

muscle, the smallest muscles in the body. When the ear is subjected to loud noises, they will contract and decrease the chance that the ear is being damaged, because the ossicles cannot vibrate as much as before. This ossicular reflex is limited, because it does not play a significant role in tones above 1 or 2 kHz and it is ineffective for impulsive noise like gunfire. Paralysis of the stapedius muscle will lead to abnormally sensitive hearing (hyperacusia), increasing the chance of damaging the inner ear.

The top of the middle ear (tympanic cavity) is a thin bone plate, the tegmen tympani; it separates the middle ear from the middle cranial fossa (the part of the skull that houses the temporal lobes). The lateral edge with the squamous temporal bone forms the petrosquamous suture, it is normally fused in adult life. This can be a route for an infection to spread from the middle ear to the brain, especially when it is not yet fused, where it can lead to meningitis.

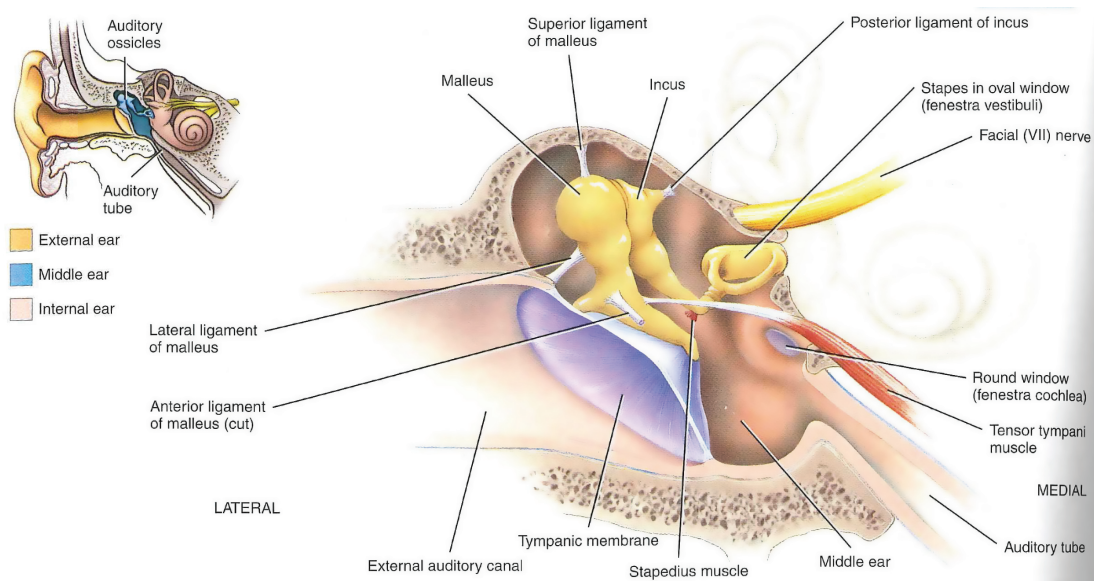


Figure 2.2: An overview of the middle ear with its three bones (ossicles) that connect the eardrum with the cochlea. Reprinted with permission, figure 17.19 from [4].

The floor of the middle ear also has a thin plate of bone that separates it from the main blood vessels in the brain: the internal carotid artery and the internal jugular vein. Damaging these vessels during surgery could be fatal. Between these two vessels lies the tympanic branch of the ninth cranial nerve (glossopharyngeal). When this nerve is stimulated electrically, it can lead to pain experienced around the ear or throat. A Cochlear Implant can do this unintentionally.

The anterior wall of the middle ear (the wall located the closest to the front of the head, also see appendix B) houses the opening to the auditory tube or Eustachian tube. The wall of this tube consists of bone and elastic material and it connects the middle ear with the superior portion (top) of the throat (nasopharynx). Normally there is no connection between the throat and ear, but the auditory tube opens when yawning or swallowing. This will equalize the pressure in the middle ear with the pressure outside the head, so the ossicles can vibrate freely. It is, however, also an easy pathway for pathogens to infect the middle ear.

The posterior wall (the wall located the closest to the back of the head) houses on others the

canal for the nerve of taste (chorda tympani) and the facial nerve. The incus is also attached to this wall. There is an entrance to the tympanic antrum (a relatively large air-filled space that communicates with the mastoid air cells).

The lateral wall (the wall located closest to the outside) is primarily occupied by the tympanic membrane (eardrum). It has a diameter of roughly 10 mm and is grey of colour. The top part is flexible and the bottom part is stiff. It fits into a groove in the tympanic bone of the external ear canal. This groove is a landmark when performing an implantation of a CI.

The medial wall (the wall located vertically closest to the centre of the skull, opposite the lateral wall) holds the cochlea. Only the basal turn (promontory) is visible in the middle ear. The top of the medial wall is called the fenestra vestibuli and it leads to the inner ear, specifically the vestibule which houses the semicircular canals. The fenestra cochleae is situated under the fenestra vestibuli, only the promontory separates the two. The cochlea has two membrane-covered openings: the oval and round window. The oval window is covered by the stapes and the round window is covered by the secondary tympanic membrane. More about this is mentioned in the next section. During surgery the facial nerve has to be avoided, the nerve has a prominent (horizontal) location in front of the fenestra cochleae.

2.1.3 Internal ear

The internal ear (see figure 2.3) is also called the labyrinth because of its complex shape. It consists of two parts: the osseous and membranous labyrinth. The first part is bony and contains the vestibule, semicircular channels and cochlea. It is filled with perilymph (more about this fluid is explained later) and surrounds the membranous labyrinth, a series of epithelial sacs and tubes. The two labyrinths are similarly shaped, though the osseous is larger than the membranous labyrinth. The last contains endolymph (another ionic fluid).

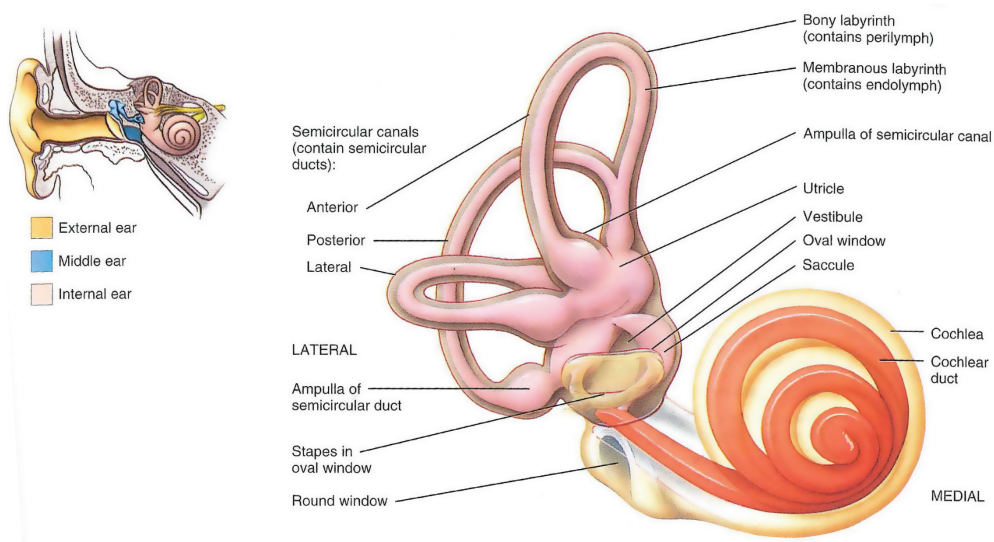


Figure 2.3: Components of the right internal ear. The complete width of the cochlea is 9 mm, and the height is 5 mm. Reprinted with permission, figure 17.20 from [4]

The vestibule is the centre portion and connects the semicircular canals with the cochlea. There are three of these canals: the lateral, anterior and posterior. Each one corresponds to one angle of rotation, the first is oriented horizontally and the other two are vertically oriented. They all have a swollen end called the ampulla. They contain hair cells that can detect fluid motion in the semicircular ducts (the portion of the membranous labyrinth). In this way a human can detect rotation of the head.

The cochlea is the final destination of the pressure wave, because it gets converted into an electrical signal there. As mentioned earlier, the outside of the cochlea is made out of bone and it looks like a snail's shell. It has about 2.5 to 2.75 rotations around the central column (modiolus) (see figure 2.5), is about 5 mm high and the base is approximately 9 mm wide. Internally there are three parallel ducts, as seen from the cross-section of the cochlea in figure 2.4:

1. Scala Media (Cochlear Duct): it is part of the membranous labyrinth and which contains endolymph. There is a connection with the membranous labyrinth in the vestibule.
2. Scala Vestibuli: it starts at the oval window (the opening that is covered by the stirrup) and is part of the osseous labyrinth, and is filled with perilymph. This is also a continuation of the osseous labyrinth in the vestibule.
3. Scala Tympani: this is the largest of the three and it starts at the round window. Like the Scala Vestibuli it is part of the osseous labyrinth and is also filled with perilymph. It connects with the Scala Vestibuli at the helicotrema (the apex of the cochlea) so the waves can travel from the oval window through the Scala Vestibuli to the helicotrema exiting at the round window via the Scala Tympani.

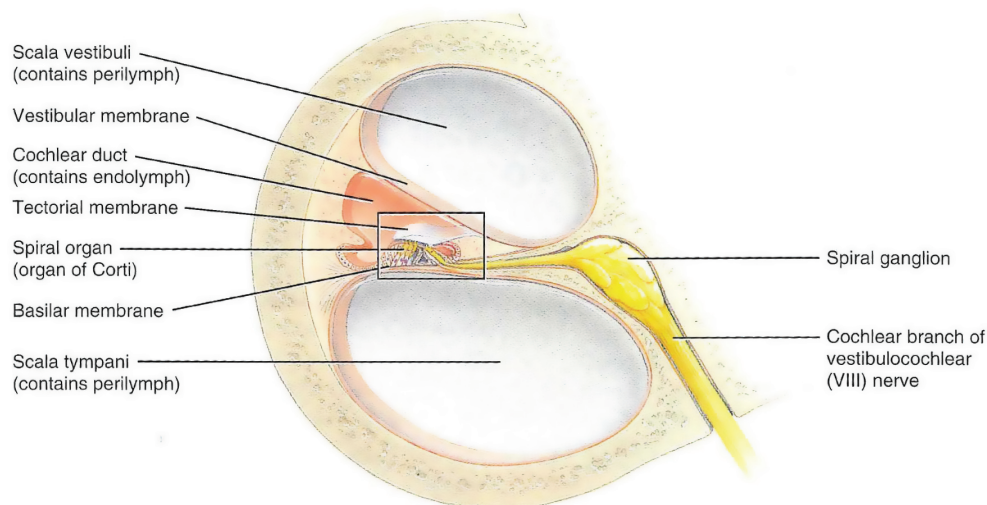


Figure 2.4: Section through one of the turns of the cochlea. The organ of Corti is shown in more detail in figure 2.6. Reprinted with permission, figure 17.21c [4]

Endolymph is a fluid that has an extraordinary high positive potential (80 – 90mV, the endocochlear potential) compared to perilymph, due to its high potassium (K^+) concentration. As mentioned previously the two liquids are separated from one another, as endolymph is only

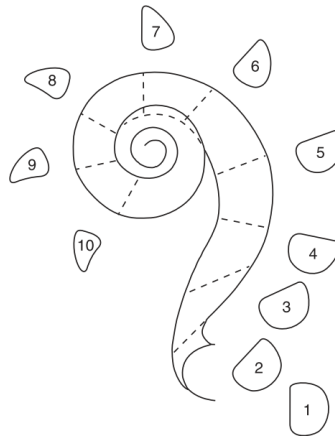


Figure 2.5: Diagram illustrating rotation of the cross section of the scala tympani. [2]

found in the membranous labyrinth and perilymph only in the osseous labyrinth. Perilymph holds a resemblance to cerebrospinal fluid, mostly because their major component is sodium (Na^+). [6] The contents of these fluids are given in table A.1 of appendix A.

Between the scala vestibuli and the scala media lies Reissner's membrane (vestibular membrane), a very delicate and thin homogeneous layer. The basilar membrane separates the scala media from the scala tympani. It also supports the organ of Corti (spiral organ). This organ contains among others, just like the ampulla in the semicircular canals, around 16.000 hair cells. There are two types of hair cells in the organ of Corti: the inner and the outer hair cells, where the first ones are arranged in a single row and the latter in three rows. Each hair cell has 40 to 80 stereocilia at their apical tip that extend into the endolymph of the scala media.

The basal ends of both kinds of hair cells synapse both with first-order sensory neurons and with motor neurons from the cochlear branch of the vestibulocochlear nerve (VIII). This is shown in figure 2.6. The sensory neurons are connected for 90-95% to the inner hair cells, while the motor neurons are mostly (90%) connected to the outer hair cells. The tectorial membrane (membrana tectoria) covers the organ of Corti and some of the outer hair cell stereocilia ends are embedded in this flexible gelatinous membrane. The outer hair cells can put extra energy in the vibrations, amplifying the incoming signal.

Each location along the scala media corresponds to a certain frequency, starting with higher frequencies at the base of the cochlea. The basilar membrane is smaller and stiffer at the base than at the end and its resonance frequency determines which tone is processed. The frequency range lies between 20 Hz and 20.000 Hz.

When the basilar membrane vibrates, the stereocilia slide against each other. When a smaller cilium touches a taller one it creates a tip link so a transduction channel exists. The further the stereocilia bend (a larger vibration), the more K^+ ions of the endolymph flow through the channel. This will depolarize the hair cell which will open Ca^{2+} channels and that will trigger exocytosis of synaptic vesicles containing a neurotransmitter. When more neurotransmitters are released, then the frequency of impulses on the sensory neurons will increase too, creating the sense of louder tones. The release of the neurotransmitters will decrease when the stereocilia bend less, because there is less inflow of K^+ ions, resulting in hyperpolarization. A cross-section of the organ of Corti with its hair cells is shown in figure 2.7.

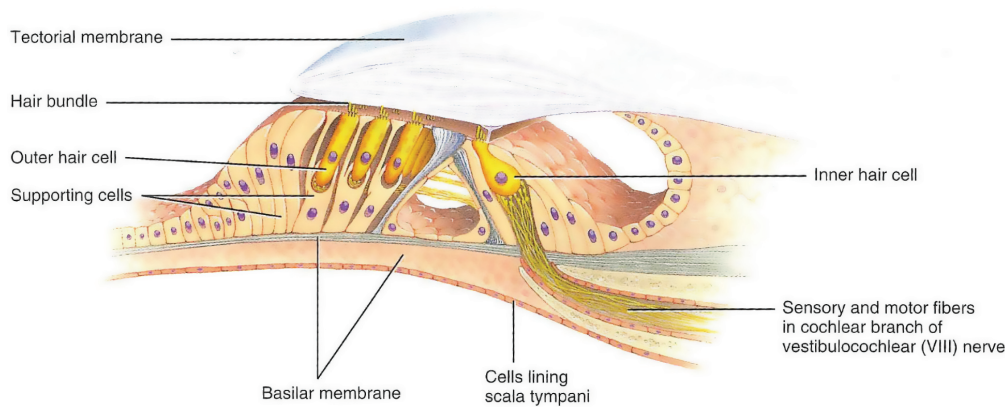


Figure 2.6: *Enlargement of the spiral organ (organ of Corti). Reprinted with permission, figure 17.21d from [4]*

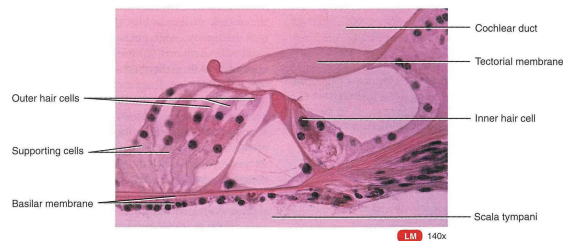


Figure 2.7: *Histology of the organ of Corti. Reprinted with permission, figure 17.21e from [4]*

2.2 Cochlear implants

Cochlear implants (CI's) have been used since the 1980's and the concept of nerve stimulation has not been changed. The functionality and quality of the CI did improve over the years. This section explains the working of the CI.

People who need CI's are completely deaf or still have some residual hearing and hear at the most some muffled sounds. This can happen due to a congenital defect, disease (genetic or non-genetic) or trauma. Not everyone who is deaf can benefit from a CI. For example, when the cochlea has only partly developed or is not present at all, because its development was hindered by some disease. Also, extra care has to be taken when implanting a CI into an underdeveloped cochlea, because it can be more fragile than a regular one. Furthermore, these patients can have a higher risk of meningitis.

In the early days of CI the electrode array was implanted in the cochlea into the scala tympani through the round window, but nowadays a hole in the wall of the cochlea is made at the beginning of the basal turn. This has the advantage of having a straight piece at the beginning of the implant and after that only the spiral shape. The electrode array is placed with the help of an insertion tool, which is straight. The electrode array is most of the times pre-curved and flexible. During the placement, the array is pushed off the insertion tool, curling itself into the scala tympani. Contact with the walls should be avoided to minimize trauma.

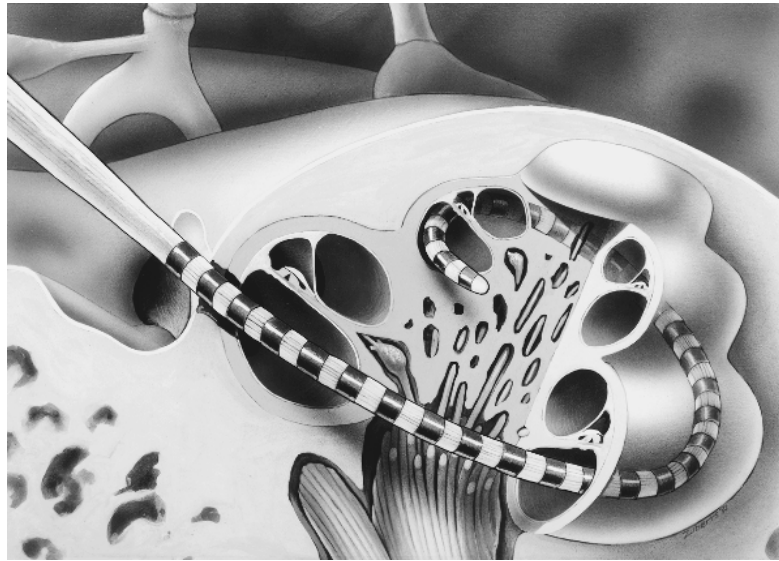


Figure 2.8: An electrode array used in CI's showing the placement inside the spiral shaped Cochlea. [2]

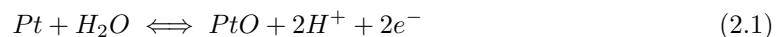
However, 10-20% of the patients receiving a CI lose their residual hearing during surgery due to unwanted physical contact [7]. The placement of a CI is illustrated in figure 2.8.



Figure 2.9: An uncurled electrode array from MED-EL, the titanium wires are wave-shaped and coated with silicone, making the device flexible. [8]

A cochlear implant is made of titanium wires, attached to approximately 20 titanium electrodes, which are coated with a soft bio-compatible polymer. The amount of electrodes and material choices are different per manufacturer and model, but this is the common factor in all of them. There are three major CI manufacturers: Advanced Bionics, Cochlear and MED-EL. An electrode array from the latter is shown in figure 2.9.

The stimulation circuitry used in a CI is beyond the scope of this thesis, the signals that are supplied to the electrodes are not. The auditory nerve is stimulated by a CI with electrical charge. When platinum is used, this charge travels from electrode to nerve via a series of reversible electrochemical reactions at the electrode-tissue interface. This is called faradaic charge injection and it is usually capable of delivering more charge to the nerve ending than capacitive charge injection. The latter does not work with the electrochemical reactions, because it works electrostatic (charge separation or dipole orientation) or electrolytic (charge storage). It depends on the material of the electrode which type of charge injection is performed. Like stated earlier, platinum (Pt) utilizes faradaic charge injection, because it makes use of electrochemical reactions. These reactions are:



Titanium Nitride is a material that utilizes capacitive charge injection. A layer of dissolved

positive ions, e.g. Na^+ , forms a layer above the electrode. Both capacitive and faradic charge injection will transfer charge to the organ of Corti, specifically the inner hair cells which hold the sensing nerve endings. Some sites at the neural population depolarize when the charge passes its membrane, making it permeable to sodium ions. This goes on until a threshold level is reached and when that happens, an avalanche of ions comes across the membrane, triggering an action potential.

The charge is created using a current source and when it is pulsed, a finite amount of charge is fed, every pulse. Most manufacturers use a biphasic charge-balanced current pulse (figure 2.10) to avoid building up toxic materials due to irreversible electrochemical reactions. These kind of reactions can change the pH, create hydrogen and oxygen, dissolve metal or can lead to complex combinations of metal with proteins. This happens when the charge at the electrode interface is too high, either due to the build-up of residual charge or due to a too high stimulus voltage.

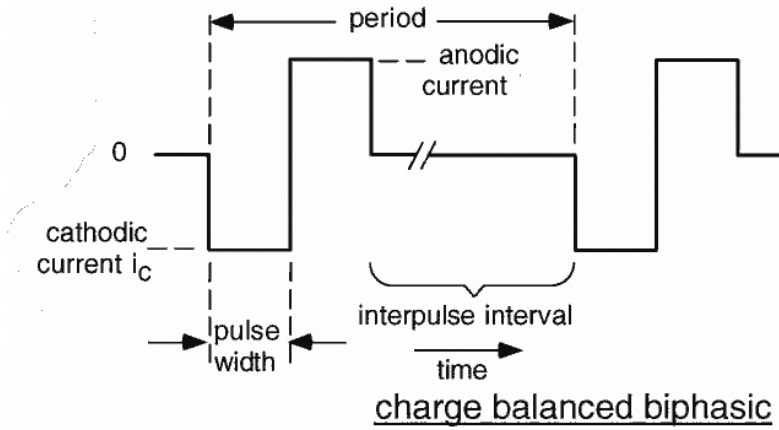


Figure 2.10: A charge-balanced biphasic current pulse consists of an anodic and a cathodic pulse which can be symmetric, like shown here or can be asymmetric [9]. The integral over time of both types is still 0 to maintain charge neutrality. The charge per phase is defined as: $I_c[C/s] \times t_c[s] = q_c[\mu C/phase]$, where I_c is the absolute current level of the cathodic pulse and t_c the duration of the cathodic pulse (pulse width). Furthermore, a charge per density can be defined as $q_c/GSA[\mu C/cm^2]$, where the GSA is the geometric surface area. This is not the Electrochemical Surface Area (ESA) that also takes the surface roughness into account.

Every patient is different and the placement of the CI also changes per person. This will also affect the amount of charge that needs to be delivered to each electrode. Moller et al. [7] states that this ranges from less than $10^{nC/phase}$ up to more than $200^{nC/phase}$ using charge-balanced pulses of $300\mu s$ in duration. This value is calibrated during the first turn-on of the CI and will remain the same for a long time. No large variations will occur after the surgery. This minimal charge per phase to trigger an action potential is called the *threshold charge/phase*. This also introduces the term *threshold charge density* which is defined as the minimum charge per surface area per phase that triggers an action potential. Another parameter that needs to be introduced is the *stimulus rate*, which is defined as the amount of pulses per second. This nowadays ranges from $100pulses/s$ up to $2000pulses/s$ [10]. Exact numbers are not available publicly. Note that the stimulation rate is not the tone that is perceived.

There are three types of stimulation modes: bipolar, common ground and monopolar. Bipolar

stimulation occurs when a current is passed from one electrode to the next. It is also possible to pass current through multiple electrodes simultaneously to other electrodes. In that way the electric field can be guided more accurately, stimulating a certain nerve ending more accurately. This technique is called current steering [11]. Using that technique the same amount of current that should be delivered to one electrode is now transported to two electrodes. The charge is the same, but is now delivered to a place between the two electrodes. The location where the charge is to be delivered depends on the ratio of the two currents. With common ground, every electrode is kept as ground, only the stimulated electrode is put on a certain voltage. monopolar stimulation means that there are one or more fixed ground electrodes and a potential difference is created between the stimulated electrode and the ground electrode(s).

The *water window* is a very important factor in electrode design. It is the range of voltages that can be used to stimulate without creating hazardous materials, such as electrolysis of water. This factor depends mostly on the material being used and can be determined with Cyclic Voltammetry (CV) (section 4.7). TiN has a safe water window between $-1V$ and $1.2V$ [12]. That has however been tested with a slow CV ($5mV/s$) and [13] states that these values can be up to $-3V$ and $1V$, respectively, with a fast CV ($> 10V/s$). There is a large variation of values, as written in [14]. There are also reports of a water window of $-0.3V$ to $0.6V$ [15]. The water window depends on many factors and this needs to be evaluated for every different design and possible supplied waveform. Combining all of the parameters that have been given in the last section, the *Charge-Injection Capacity* Q_{inj} can be introduced. This is defined as the amount of charge per unit GSA (Geometric Surface Area) delivered in the leading phase of a stimulation pulse.

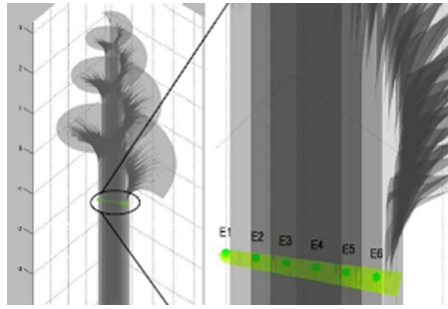
2.3 Electrode array design

Daily Supervisor Nishant Lawand has proposed multiple new designs for Cochlear Implant electrode arrays. During his PhD project he researched two different types of arrays. The stiff version which is intended to be inserted perpendicularly puncturing the cochlear auditory nerve. It gives the advantage of auditory nerve stimulation rather than stimulating the nerve endings or hair cells inside the cochlea. The flexible design is to demonstrate the fabrication capabilities and further the possibilities for in-vitro and in-vivo characterization. The flexible design has the advantage of being less invasive than the stiff probe, because it is implanted like the CI's used nowadays. The next two sections give a brief overview of the designs.

2.3.1 Stiff design

The stiff probe is designed for implanting (puncturing) the auditory nerve. This design is proposed because it does not need a flexible structure, which can improve functionality and simplicity. Also, because it does not need to fit into the narrow turns of the cochlea it can stimulate the bunch of neurons present in the nerve fibres close to the stimulation site of the stiff probe. The current CI electrode array does not get far enough inside as can be seen in figure 2.5. The tight bend and narrow part is hard to penetrate without causing damage to the walls of the Scala Tympani. That makes it hard to achieve the frequencies that are processed behind that point. It is, however, more invasive than the regular flexible implants, because it is inserted into the auditory nerve.

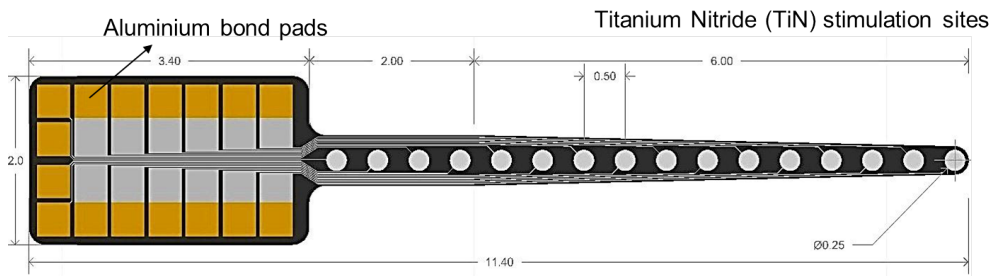
The auditory nerve which is nothing but a bundle of single nerve fibres closely packed together to form a complete auditory nerve present below the cochlea is arranged in such a manner that each single nerve fibre responds to a particular frequency. The stiff probe design consisting of silicon as a base material with titanium nitride as stimulation sites is aimed to penetrate and stimulate the bundle of nerve fibres corresponding to their respective frequencies. This design also allows the multiple types of stimulation, as mentioned in section 2.2. A model of this implant is shown in figure 2.11a.



(a) Volume conduction cochlear model with the part of stiff probe inserted in the auditory nerve model.



(b) Part of the stiff probe used for simulation.



(c) Design of the stiff probe, dimensions are in mm

Figure 2.11: Models of the stiff probe

The design of the stiff probe, as shown in figure 2.11c, contains 16 stimulation sites. The part of the stiff probe containing 6 stimulation sites is considered for simulation taking into account the volume conduction computational model [16] of the cochlea. The 16 circular electrodes are made of Titanium Nitride. They have a diameter of $75\mu\text{m}$ with a pitch of $500\mu\text{m}$. These stimulation sites are connected by metal tracks to the aluminium bond pads present at the base of the cochlea. These bond pads form an intermediate connection between the external circuitry and the stimulation sites. To avoid contact with the biological world the device is selectively coated with a biocompatible material like Parylene keeping the stimulation sites open to perform the stimulation process.

2.3.2 Flexible design

The flexible electrode array is inserted into the scala tympani, as explained in 2.2. The layout of the flexible array is almost the same as the stiff probe (figure 2.11c). The only difference is the addition of the recording electrodes in the close vicinity of the stimulating electrode. Recording electrodes are meant to record the neural activity, at the same time as stimulating them. Neuronal recording in most of the electrode arrays is done from the stimulation electrode site after the stimulation process has been completed [17]. Using one electrode for both stimulating and recording will result in a stimulus artifact of the stimulation process.

The device is made flexible by replacing the silicon substrate with Polyimide (PI). PI is a polymer of imide monomers and comes in different types, changing in for example curing options [18]. It is flexible, biocompatible, and a good insulator with high chemical and electrical resistance (resistivity in the order of $10^{17}\Omega\cdot cm$ and dielectric constant of 3.4). Due to these properties PI is generally been used to coat medical implants. PI can be spin coated and patterned with the same techniques as used for regular chip fabrication. This makes it ideal to create micro-electrodes and combine it with metals. The flexible electrode design in our case consists of the stimulating electrode (200nm of titanium nitride), sandwiched between two PI (10 μm 115A Durimide TM) layers. The upper PI layer is selectively patterned using dry etching to open the stimulating sites which will deliver the charge to stimulate the neurons.

It has to be noted that the designs described in this section are for research purposes only, so the dimensions and layout need to be optimized for use in humans, or even for in vivo experiments. The length of the research electrode array is 11mm, which is smaller than the current electrode arrays (the Clarion of Advanced Bionics and the Nucleus22 of Cochlear Ltd. both have a length of 25mm [19]), and the electrode size needs to be verified, because the charge-injection capacity needs to be high enough.

Rousche et al. [20] reported an electrode array based on polyimide for intracortical stimulation. Brain stimulation is very similar to cochlear nerve stimulation, both make use of the charge to stimulate the neurons. The process of creating such a flexible electrode array is always rather the same. It starts with a silicon wafer and an sacrificial layer like aluminium or oxide on top. Then the first layer of polyimide is applied and patterned. After that, the steps can differ somewhat, depending on the metals used. However, they all include metallization of biocompatible materials. The last step is to deposit another similar layer of PI - coating the whole device - and then selectively patterning the stimulation sites which would be in close proximity of the nerve endings.

The reported electrode arrays differ in their shape, size and materials, some of them are listed in Table 2.1. All of these designs make use of at least two layers of metal. Before the application of Gold there is the need for an adhesion layer. Gold has a high conductivity ($4.10 \times 10^7 S/m$) [21], is corrosion resistant and biocompatible [22] for use in the neural environment. It does not adhere to polyimide well enough, so an adhesion layer like chromium or titanium is required.

Table 2.1: Comparison of four papers that utilize polyimide in their electrode array design

Electrode Size	Electrode Pitch	Polyimide	Metals	Type of electrode array	Reference
Circular with a diameter of $15\mu m$	$200\mu m$	$10\mu m$ of DuPont Pyralin 2525 (for the bottom) and 2555 (for the top)	Gold and Titanium	Neural Recordings	[23]
Square, $40 \times 40\mu m^2$	$210\mu m$	$2\mu m$ of Hitachi PIQ 13 [®]	150\AA of Chrome and 3000\AA of Gold	Auditory cortex measurements	[24]
Unknown	Unknown	$1.3\mu m$ of polyimide, type unknown	75\AA of Chrome and $0.4\mu m$ of Gold	Neural recordings	[25]
Square, $30 \times 30\mu m^2$	Unknown	$10 - 20\mu m$ of Probimide 7520	250\AA of Chrome and $200nm$ of Gold	Intracortical neural interface	[20]

2.4 Electromigration

Electromigration is the phenomenon that will damage certain metals when the current density exceeds the safe operating limits. This failure mode is normally observed in the interconnecting metal in integrated circuits. In CI's this parameter is important while designing the metal tracks which are connecting the bond pads with the stimulation sites in the electrode arrays. Further paragraphs give more details about the electromigration.

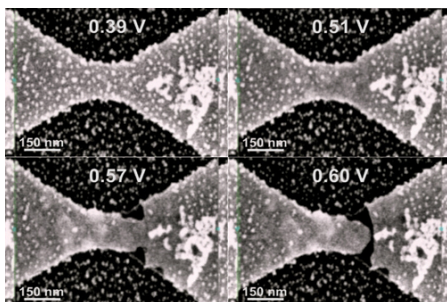


Figure 2.12: Electromigration of gold (Au) at different voltages. Study is conducted by Thiti Taychatanapat of Cornell Center for Materials Research [26]

Electromigration occurs when the dimensions shrink, but the amount of current that needs to be transported stays the same. Earlier this was only a problem in integrated circuits, but can not be neglected for the metal tracks in CI's. Instead of the platinum wires that have a diameter of $0.025mm$ (a cross sectional area of around $500\mu m^2$) now tracks of at most $10\mu m$ wide and $500nm$ thick (creating an area of $5\mu m^2$) are used in our design and generally observed in the same range as the modern microelectrode arrays. This leads to a current density increase by a factor of at least 100. It is possible to use multiple electrodes, decreasing the amount of current per channel, but there will be an increase in the current density of a single track.

Electromigration is the phenomenon which follows a forced atomic diffusion that occurs due to a large electric field [27]. Metal ions are

transported through the channel due to the large amount of charge carriers. This will physically move particles from one place to another. When it has started, it will cascade until there is no metal left at the spot where it happened, because there is a local increase of current density. Figure 2.12 shows what happens to gold when the current density is too high.

There are multiple factors that influence electromigration. One is the material; the softer it is, the easier it will damage. That is one of the reasons that gold is the material of choice for an experiment like in figure 2.12. Aluminium is a material that is widely used in integrated circuits, but is also very susceptible to electromigration [28]. Temperature is also a factor, because the diffusion constant is largely dependant on it. Diffusion is the driving force of electromigration. Finally, DC has a much larger electromigration effect than AC. With DC there is a constant electric field pushing the metal ions away from their initial position. AC only has shorter periods of maximal electric fields and it has a field in the opposite direction, which allows the ions to get back to their original position. The chance of this process occurring is quite small, however, because the current density at that position is higher. Aluminium has the rule of thumb that tells that the maximum current density is roughly $1mA/\mu m^2$ at $125^\circ C$.

2.5 BiCMOS process

The cochlear implants (CI's) used nowadays consists of platinum-iridium wires hand-soldered to small ($4 \times 4mm^2$) square platinum electrode plates. They contain only passive components and to accommodate CI's with better quality and functionality in the future an addition of active electronics in the electrode arrays can be looked upon. These transistors will control the stimulation and recording activities. A process is needed that is simple, robust and has a high design flexibility. The BiCMOS process designed by Henk van Zeijl gives us the possible directions for the integration of electronics in the electrode array. This section focuses on this path explaining the BiCMOS process developed in DIMES using a non-traditional metallization step.

The number of metal tracks that can be placed along the length of the electrode array depends on the width of the tracks, the space between the tracks and the size of an electrode site. With the current technology and the anatomical cochlear restrictions the number of stimulation sites is limited and in our current design every electrode needs to be connected directly to the receiver-stimulator via the metal tracks. A smaller number of stimulation sites results in less neurons to be stimulated, thus limiting the selectivity and the frequencies that can be perceived. To accumulate a larger number of stimulation sites on the electrode array for more functionality a probable solution would be getting rid of most of the metal tracks. This could be achieved by bringing active electronics (like transistors, multiplexers etc.) close to the stimulation site. By using the transistors a circuit could be created that only needs a few tracks. Such a circuit could be some kind of multiplexer circuit that utilizes at least three tracks: ground, power and signal. The signal line transfers a decoded signal to the circuit(s) that is/are embedded in the electrode array. The implementation of such a circuit is behind the scope of this thesis, but the transistors that are used in the circuits are the area of interest. The metal that is used as interconnect material is preferably the same as the electrode material, to minimize the steps needed to create an electrode array. Furthermore, the interconnect metal needs to meet the requirements as described in chapter 3 too, just like any other metal in the electrode array.

The BiCMOS process is a simple 5 mask process that involves both Bipolar and CMOS

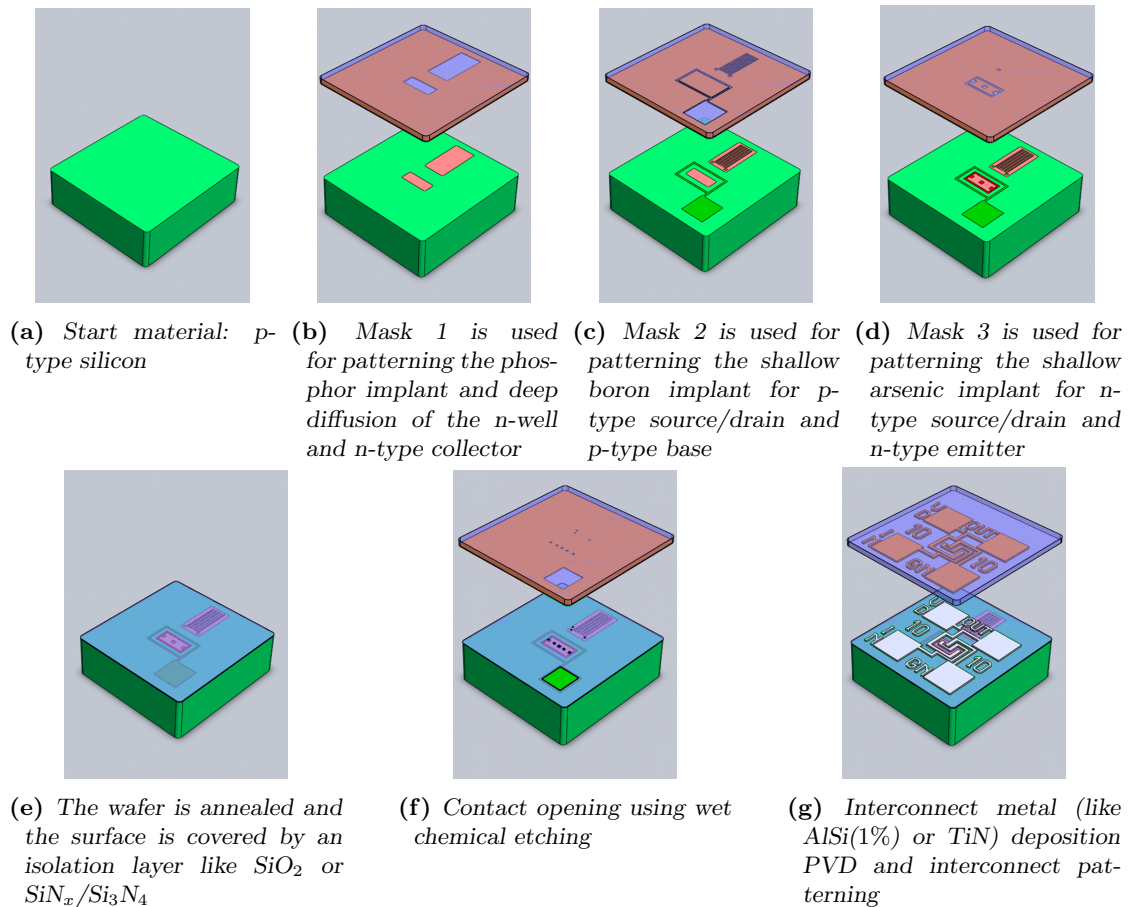


Figure 2.13: The 5 mask steps of the BiCMOS process. The structures shown in the subfigures are an npn transistor and a resistor.

transistors. This has the advantage of using both types of transistors, but the disadvantage of having a trade-off between the two optimum settings. Figure 2.13 shows this 5 masking steps needed for this process. The process is now described using the structure of the transistors. It starts with a p-type wafer that is patterned for some of the n-type regions: the n-wells of the npn and PMOS transistors. This is done with a phosphor implant and a deep diffusion. The second mask is used to create the p-type regions: the base of the npn transistors, the source and drain of the PMOS transistors and the isolating rings around the NMOS transistors. They are doped using a shallow boron implant. The third mask is for the highly doped n-regions: the emitter and (contact regions of) collector of the npn transistor, the source and drain of the NMOS and the isolating ring around the PMOS. This is done with a shallow arsenic implant. After that, the wafer is annealed for 15 minutes on 1000°C and the complete surface gets an isolation layer of 100nm of SiO_2 (by thermal oxidation) or a stack of $\text{SiN}_x/\text{Si}_3\text{N}_4$ (by deposition, $80/20\text{ nm}$ thick). This layer will both act as an isolation layer between the interconnect and the substrate and as the gate material of the PMOS and NMOS transistors. This means that a trade-off has to be made for the thickness of this layer. A transistor has the best characteristics with a low gate thickness, while the isolation layer at rest of the wafer is preferably thick to minimize parasitic

effects. The fourth mask is used to make the contact openings in the isolation layer. All of the connections to the shallow n- and p- layers need a contact opening. The fifth and final mask is used to pattern the interconnect layer. This layer exists of a metal and covers all of the contact openings and creates a circuit by combining the different components. The final result of the three types of transistors are shown in figure 2.14.

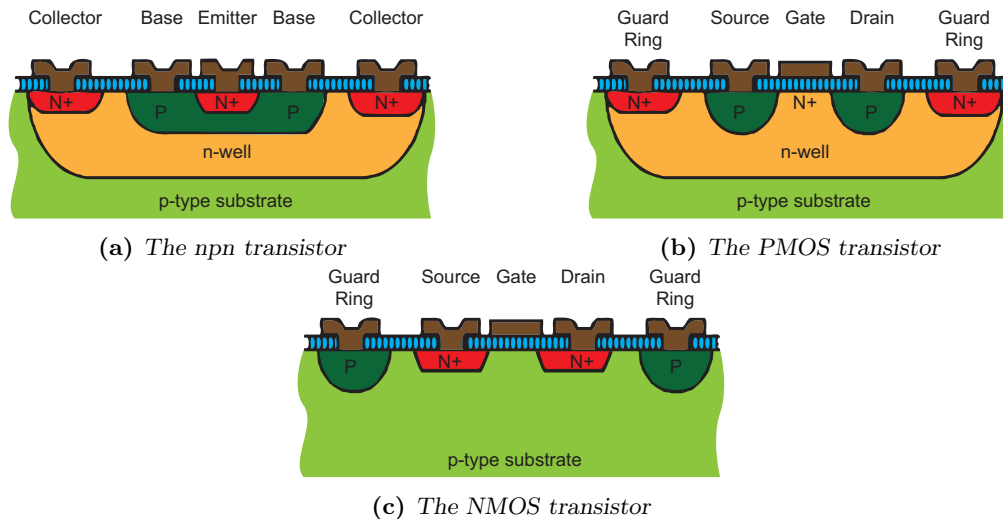
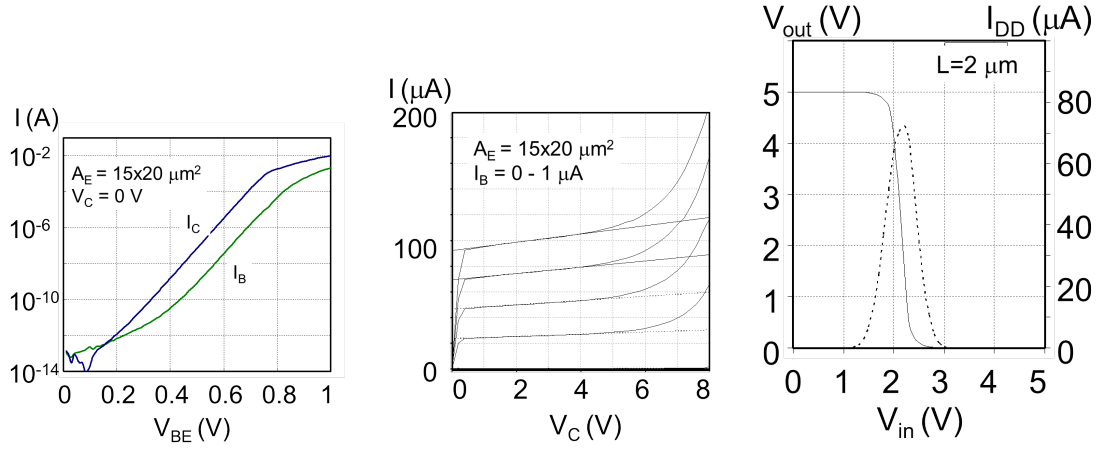


Figure 2.14: The cross-sections of the three types of transistors that can be produced using the BiCMOS process

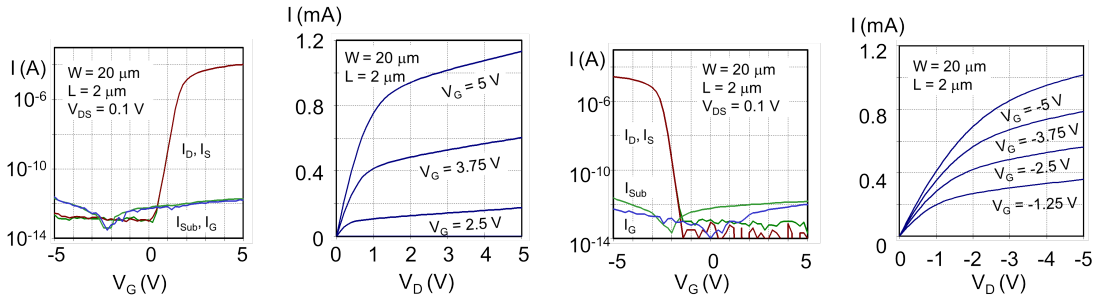
As mentioned in the previous paragraph, there are some trade-offs in the design of the BiCMOS process. The thickness of the isolation layer is a trade-off between the optimum gate layer thickness and the preferred thick layer of isolation between the substrate and interconnect. Normally there would be an extra mask to pattern the gates. Another trade-off is the dopant concentrations of the n- and p- regions. The bipolar and CMOS transistors have benefits at different concentrations. All of the parameters that characterize these transistors are dependent on the dopant concentration, for example the threshold voltage and the saturation current. These parameters are also dependent on the width and length of the gate or base. That is why there is a design for experimental purposes that includes the three types of transistors with different sizes and a lot of other structures that can characterize parameters of the process like the contact resistance. The layout of this die is explained more in section 4.9 and is shown in appendix C.

The low number of masks is also the reason that the pnp transistor cannot be created. An extra mask is needed to achieve that. Additional masks and the following processing steps are a solution to the trade-offs and the lack of the pnp transistor. That will, however, compromise the simplicity of this process. To reduce the mask cost a smaller number of masks were considered for these experiments. The early stages of the cochlear implants containing these structures are going to be highly experimental.

Previous measurements by Henk van Zeijl have shown that this process produces working devices. That wafer used an isolation layer of SiO_2 and aluminium-silicon as the interconnect metal. The graphs that show the characteristics of this particular process are shown in figure 2.15. It shows that the process is able to produce transistors with reasonable characteristics.



(a) Gummel plot of the npn transistor with a base length of $15\mu\text{m}$ and width of $40\mu\text{m}$ (b) Relationship between the collector current and voltage for different gate potentials (c) Transient characteristic of an inverter created using a PMOS and NMOS



(d) The currents in the NMOS transistor for a changing gate voltage (e) The relation of the drain current of a NMOS with the drain voltage for different gate voltages (f) The currents in the PMOS transistor for a changing gate voltage (g) The relation of the drain current of a PMOS with the drain voltage for different gate voltages

Figure 2.15: Characteristics of the BiCMOS process using SiO_2 as isolation layer and aluminium-silicon as interconnect material. A_E is the area of the gate of the npn transistor, V_C is the collector voltage, V_{BE} the voltage between the base and emitter, I_C is the collector current, I_B is the base current. V_{out} is the output voltage of the inverter, V_{in} is the input voltage of the inverter, L is the length of the gate for both the NMOS and the PMOS inverter, I_{DD} is the drain current. W is the gate width, V_{DS} is the drain-source voltage, I_D is the drain current, I_S is the source current, I_{Sub} is the current through the substrate, I_G is the gate current, V_G is the gate voltage, V_D is the drain voltage.

Chapter 3

Metal requirements

In order to use a material in a highly demanding application like CI's it needs to meet certain requirements. There are regulations set by the Food and Drug Administration (FDA) for human use, but more importantly the material has to withstand the extreme environment of the human body over a long period of time (without causing damage). This chapter deals with those requirements and all the different measurements used to test them.

Section 3.1 shows what requirements need to be met for the charge transfer characteristics. These are dependent on multiple factors, as described in its subsections. Biocompatibility, an essential requirement, and the measurements needed to characterize different metals that are candidate for usage in a CI, are described in section 3.2. Finally, section 3.3 shows what measurements can be done to characterize a good material for the logic implementation in Cochlear Implants.

3.1 Charge transfer

The charge created by the current sources needs to be transferred from the stimulation circuitry to the nerve endings. Products used nowadays consists of the electronic circuitry packaged in a housing which is carried behind the ear or in a bag that is worn from the neck. The signals are then transmitted through the skin using a magnetic coil that transmits both the audio signals and the power that is needed for the stimulation circuitry. Under the skin is a device called the receiver-stimulator that receives the signals mentioned earlier and stimulates the electrode array. The current flows from the receiver-stimulator through wires to the electrode array. The electrode array contains wires or tracks that need to carry this current to the stimulation site and which transfers the charge to the nerve ending through reactions like explained in section 2.2. The electrode array has to conduct a certain amount of current without dissipating too much heat. The electric field may not be too high, especially where there is no exposed stimulation site. Furthermore, the impedance of the material should be not too high to minimize the potential differences across the electrode array. Also, the capacitive or inductive behaviour needs to be minimized in order to have a reliable waveform at the nerve ending.

The requirements mentioned in the previous paragraph can be measured and simulated with a number of tests. The maximum amount of current that can be passed through a track at the

electrode array is defined by the electromigration and the dissipated heat, section 3.1.1. The impedance of a metal is dependent on the temperature, by a coefficient called the Temperature Coefficient of Resistance (TCR), section 3.1.2. The electric field around the electrode array can be measured or simulated and is explained in section 3.1.3.

3.1.1 Electromigration

The background information on electromigration can be found in section 2.4. Electromigration is the limiting factor for the maximum amount of current that can be passed through a conductor. The vacancy flux (J) due to the force induced by electromigration is related to multiple other parameters by equation 3.1 [27]. c is the vacancy concentration, D the diffusivity, k Boltzmann's constant, T the absolute temperature, e the electronic charge, E the applied electric field, ρ the resistivity and j the current density. Z^* is a dimensionless material parameter and consists of two components, as in equation 3.2.

$$J = -D \frac{\partial c}{\partial x} + \frac{Dc}{kT} Z^* e E = -D \frac{\partial c}{\partial x} + \frac{Dc}{kT} Z^* e \rho j \quad (3.1)$$

$$Z^* = Z_{wd} + Z_{el} \quad (3.2)$$

Z^* can be called the effective charge, Z_{wd} is attributed to momentum exchange between the electron current and the moving atom and Z_{el} is related to the direct electrostatic force on the moving atom. Z_{wd} , also called the electron wind, is the dominant factor, thus the atoms drift in the same directions as the electrons.

The steady state solution of equation 3.1 occurs when the driving force due to generated stress equals that of electromigration, like in equation 3.3. Ω is the atomic volume and σ the stress.

$$Z^* e \rho j = \Omega \frac{\partial \sigma}{\partial x} \quad (3.3)$$

The diffusivity D shows a strong temperature dependence as given in equation 3.4. E_a is the activation energy for diffusion. From this equation it can be seen that higher temperatures are more susceptible to electromigration. A test at a higher temperature than body temperature (37°C) gives the results for an accelerated test. It can be used to see if materials are affected by a certain current density at all. [29] reports that a certain amount of stress (σ_c) needs to be exceeded to start the electromigration.

$$D = D_0 e^{E_a/kT} \quad (3.4)$$

The most widely used equation to analyse electromigration is Black's equation [30], as shown in equation 3.5. The MTF is the median time to failure in hours, A is a constant which contains a factor involving the cross-sectional area of the film, J is the current density in A/cm^2 , E_a is still the activation energy in electron volts. The activation energy is largely dependent on the way how the material is deposited. [30] reports an activation energy of 0.48 eV for small crystallite aluminium, where well-ordered large-grained aluminium has an activation energy of 0.84 eV.

$$\frac{1}{\text{MTF}} = A J^2 e^{-E_a/kT} \quad (3.5)$$

As described in section 2.4 the largest amount of stress is produced under a constant electric field, thus a constant current. To accelerate the test, a higher temperature can be used. Combining

these two statements, a setup can be designed: a piece of narrow metal that transfers a certain amount of constant current. The environment of the test setup can be at an elevated temperature to speed up the results. The test will end when the metal under investigation exhibits electromigration, finally resulting in the breaking. It might occur in a few hours, days or even weeks. The failure depends on the internal material properties and its capacity to conduct the current. After the test has stopped, the tested die needs to be investigated under a microscope to observe the effects. In case of a breakdown, a void may be expected in the track and maybe some damage at other locations. Otherwise, there might be some damage already, but no fatal breakdowns have occurred yet. The damage should also be visible in the voltage characteristics of the track. When there are narrows in the track, the resistance goes up, thus the voltage goes up, because the current stays constant.

3.1.2 TCR

The Temperature Coefficient of Resistance (TCR) is a material dependent parameter that describes the change in the impedance with respect to temperature. For most materials the resistance increases with increasing temperature, some materials exhibit an opposite behaviour. These materials have a Positive Temperature Coefficient (PTC) or Negative Temperature Coefficient (NTC), respectively. In rare occasions it is possible that the resistance is close to 0Ω when it reaches a very low temperature. It depends on the material what temperature this is, but the highest temperatures reported are around $125K$. The materials that show this property are called superconductors. Such a low temperature will not occur in the human body, thus no further research will be done on this phenomenon.

The TCR of a metal can be described by a simple equation 3.6, where $\rho(T)$ is the resistivity of the material at temperature T given in $(\Omega \cdot m)$, ρ_0 is the resistivity at reference temperature T_0 and α is the TCR [31].

$$\rho(T) = \rho_0 (1 + \alpha(T - T_0)) \quad (3.6)$$

$$\alpha = \frac{1}{\rho_0} \left[\frac{\partial \rho}{\partial T} \right]_{T=T_0} \quad (3.7)$$

The resistivity ρ can be replaced with the resistance R in equations 3.6 and 3.7, the α stays the same, because its unit is $(^\circ C)^{-1}$. These (linear) equations apply to simple materials like the metals, but semiconductor materials comply to non-linear equations. They are out of scope of this thesis.

The temperature in the ear is constant, however there might be a rise in temperature due to an illness. Though minimal, the temperature range of the human body is something to keep in mind when designing and calibrating the CI. With these measurements the resistance at every temperature can be deducted. A change in temperature can happen due to the joule heating (self heating when a current is flowing) of a track. This must be kept to a minimum, because the slightest rise in temperature in the cochlea can lead to damage of the Organs of Corti.

A method to determine the TCR is to measure the resistance at different temperatures. The results can then be combined with equation 3.6 to obtain the TCR. The resistance should not be very susceptible to temperature changes, thus the TCR must be relatively low.

3.1.3 Electric field distribution

When the density of electrodes increases, it is important to know the electric field distribution through the perilymph of the scala tympani. Furthermore, the effect of changing some parameters need to be evaluated, like the thickness of the insulation layer, the depth of the cavity for the metal and the dimensions of the electrode. The electric field of one electrode should be very directional and - combined with another stimulation site - it is possible to steer the electric field to another nerve ending, like explained in section 2.2.

An electrode can have different shapes and sizes, but to achieve a high density electrode array a stimulation site with lower dimensions aiming to stimulate less population of neurons is desirable. The minimum size is specified by the charge injection capacity. Furthermore, it is not desirable to have very high (local) electric fields, e.g. at corners. Sharp angles have another disadvantage of being a possible hiding place for unwanted materials and organisms, like bacteria, thus smooth surfaces are favoured.

The electric field distribution is influenced by multiple factors. One is mentioned in the last two paragraphs: the dimensions of the electrode and the insulating layer. Not only the dimensions are important, also the dielectric constants of all materials are of interest: the insulating layer and the perilymph. Literature explains [32] [33] [34] about the electrical properties of the fluids in the human body and it can be recreated easily with purified water with some kitchen salt (NaCl, without Iodine). The other contents of perilymph can be neglected for this measurement, but for biocompatibility measurements it should be taken into account. Table A.1 shows what substances there are in perilymph.

The finite element study for the electric field distribution can be simulated with COMSOL Multiphysics 4.2[®]. A two dimensional finite element model (FEM) can be created of a cross section of the electrode array in perilymph to evaluate the electric field. It is possible to create a 3D FEM, but it is not really necessary and the complexity of the model increases dramatically. Static electric fields are also measurable with a test setup.

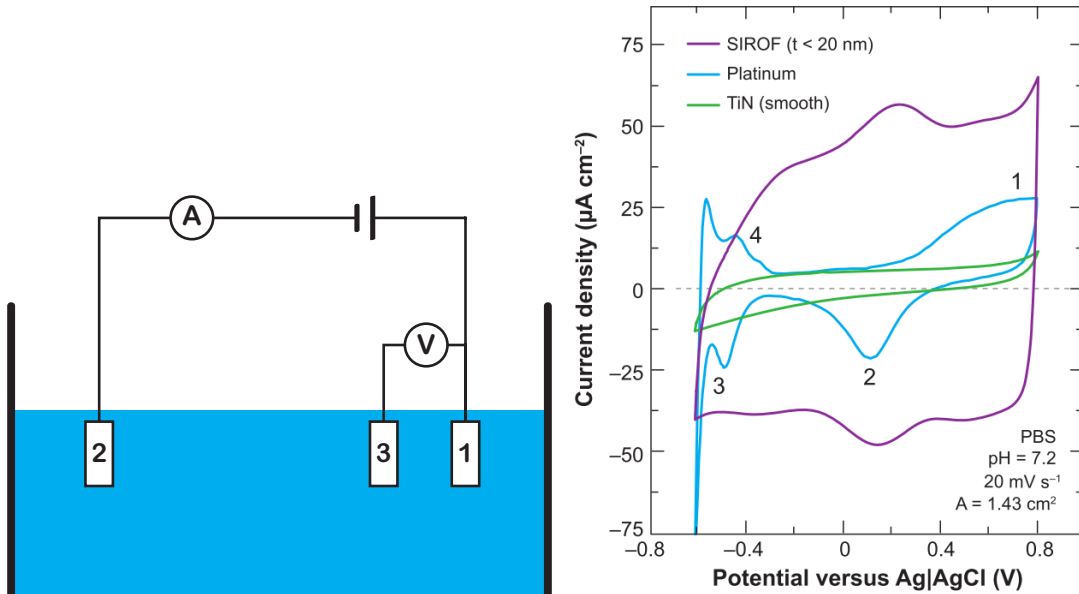
3.2 Biocompatibility

Another very important factor is the biocompatibility of the device. Does it contain toxic materials or has the ability to produce any toxic materials? When it does, under what conditions and is it reversible? Is the human body capable of including the device in the body? Are the materials of the device not dissolving in the harsh environment of the cochlea? These are some of the questions that can be asked about the biocompatibility of such a device. Before any medical device, especially implants, can be put into a human it has to not only undergo company tests, but they also need to pass the standards for human use set by the FDA (Food and Drug Administration). These standards may differ from country to country.

The tests done for this thesis are only meant to characterize the metal, not the insulating layer or the substrate material. Furthermore, only in vitro tests are carried out since for in vivo different requirements are to be fulfilled, which are out of the scope for this thesis. It is, however, possible to do in vitro experiments to see the corrosion or solubility of the different metals.

3.2.1 Voltammetry

Voltammetry is an electrochemical measurement technique that gives an indication of the contents of the material that is analysed [35]. Such a material is often a fluid, perilymph in our case, or a replacement saline solution. Every fluid has a characteristic voltammogram, thus perilymph with or without dissolved materials has different characteristics. The voltammogram is a graph that shows the applied potential versus the measured current. When some species oxidise or reduct, a spike or trough will show up in the measured current at a certain potential. This makes it an ideal technique to see if the metal is dissolving in the saline solution. It is used a lot in industrial processes to analyse specific materials that are of interest. There are also oxygen sensors that utilize voltammetry to determine the amount of oxygen in fluids like blood or sewage water.



(a) Schematic of a three electrode voltammetry measurement setup. 1 is the working electrode, 2 is the counter electrode and 3 is the optional reference electrode

(b) Comparison of cyclic voltammograms of platinum, sputtered iridium oxide films (SIROF) and smooth TiN macroelectrodes (geometric surface area (GSA) = 1.4 cm^2) in phosphate buffered saline (PBS) at a sweep rate of $20 \text{ mV} \cdot \text{s}^{-1}$. 1, 2 indicate Pt oxidation and reduction; 3, 4 indicate hydrogen atom plating and stripping on Pt, respectively. The cathodic charge storage capacities (CSC_c) of the films are $0.25 \text{ mC} \cdot \text{cm}^{-2}$, $0.55 \text{ mC} \cdot \text{cm}^{-2}$, and $2.8 \text{ mC} \cdot \text{cm}^{-2}$ for TiN, Pt, and SIROF, respectively. [9]

Figure 3.1: A typical (cyclic) voltammetry setup with reference electrode and its resulting voltammogram

A basic voltammetry setup has two or three electrodes: a working electrode, counter electrode and optionally a reference electrode. All of these are submerged in the fluid that needs to be analysed. A schematic overview is shown in figure 3.1a. To analyse the contents of the fluid,

3.2.2 Endurance tests

One of the important parameters for which the current manufacturers are aiming is to develop the future CI's with long term stability and error free functioning for more than 20 years. That means that every single component should at least last these 20 years, including the electrode array and its metal. Corrosion is one of the major factors in damaging metals, also without stimulation of the electrodes. Also the stress levels are high due to various processes in micro-fabrication and due to the changing electric field at the surface of the metal during the stimulation process.

An accelerated test is proposed with a continuous stimulation with different waveforms, for example: a sine, square or sawtooth wave. This test has to be run for a sufficient amount of time, but within the limits of a master thesis. During the test, the current through the metal track is measured. A change in the amount of current indicates an alteration in the circuit, which could be metal damage. This can be verified by an extended impedance measurement and an inspection with a microscope.

If the impedance does not change over time during the test, then this property is an important parameter for the long term stability of the metal. More (longer duration) tests, especially in a saline environment, are needed to verify the integrity of the materials. If it does change over time, then it is clear that it should not be used in real products.

3.3 Logic implementation

The need for the addition of active components is described in section 2.5. The characteristics shown there are just for aluminium and SiO_2 , thus additional measurements need to be done for the other metals that will be proposed. Over time SiO_2 can lead to fatal diseases such as cancer [37], which is why another isolation material is used: $\text{SiN}_x/\text{Si}_3\text{N}_4$.

A change of material can influence the characteristics of the different devices. The isolation layer can contain trapped surface charges, changing the threshold voltage of the metal oxide semiconductor (MOS) transistors. The dielectric constant is different for $\text{SiN}_x/\text{Si}_3\text{N}_4$ and SiO_2 : 7.5 and 3.9, respectively. The resistance of the metal can be very high, limiting the amount of current. The charge transfer between the metal and the dopant regions can be very low, in other words, a high contact resistance. But not only the change in materials influences the characteristics. The fabrication recipe for deposition and patterning the materials can change too, for example the temperature and the duration of curing the final wafer can change the structure of the materials.

All of the characteristics described need to be checked by measurements of different metals and fabrication processes. This needs to be verified by measuring devices with different dimensions, i.e. the gate or base width and length. The devices should have reasonable characteristics, but the inverter should at least work properly. A bipolar transistor can be characterized by its Gummel plot and the relation between the collector voltage and collector current. A MOS transistor also has a characteristic relation between the gate voltage and the drain current and one between the drain voltage and drain current. These characteristic relationships determine important parameters, such as in case of the MOS transistor the threshold voltage V_t and the saturation voltage V_{DSAT} and in case of the bipolar transistor the common-emitter current gain β_F and the common base current gain α_F .

Chapter 4

Measurements and simulations

Titanium nitride (TiN) and titanium (Ti) are the metals that are considered as the candidates for use in cochlear implants (CI's). Aluminium (Al), due to its toxic behaviour in human fluids is considered in our tests for comparison purposes. Also Al, which is being used widely in microelectronic industry as an interconnect, shows lower resistivity when combined with TiN. In this chapter simulations, experimental setups, measurements and results are explained that give the comparison between the properties for the different metals considered.

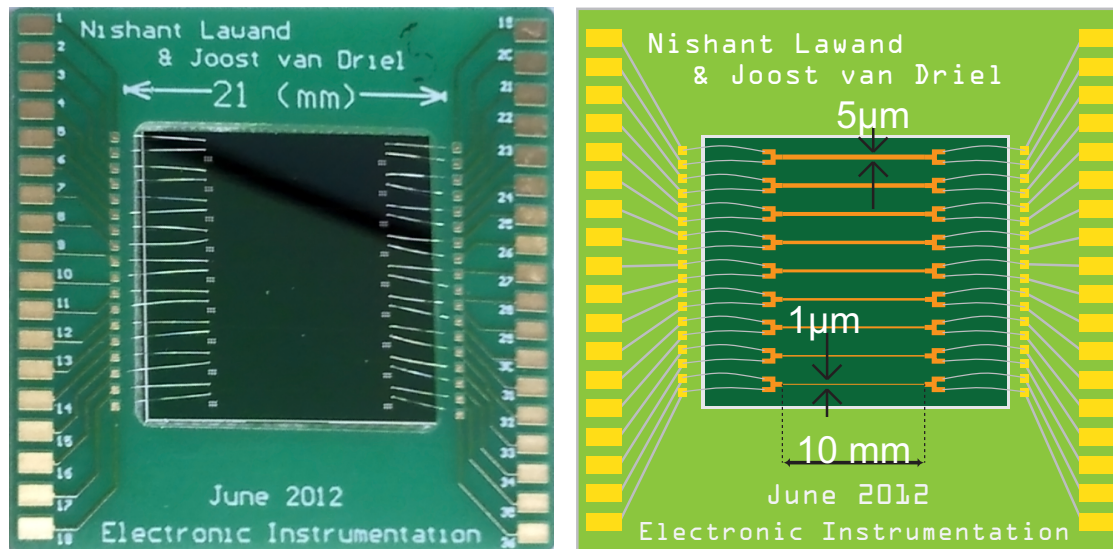
All of the measurements, apart from the BiCMOS tests, are done on the same type of test die. There are four batches of this die, all of them are processed with different metals: Al, TiN, Ti and one has aluminium covered with titanium nitride (Al-TiN). Section 4.1 goes into detail about this test die.

The test die was subjected to several tests and measurements: the impedance of the different materials, the self-heating characteristics, the temperature coefficient of resistance (TCR), electromigration and endurance in a saline solution have all been measured. The last section describes the different devices and results of the measurements on the BiCMOS wafers.

4.1 Test die

To characterize the different metals described in the introduction of this chapter a test die (figure 4.1) has been designed. The substrate of the die is a silicon (Si) wafer. This test die contains nine parallel tracks of the material that needs to be characterized. These tracks have different widths, the smallest is $1\mu m$ and the largest is $5\mu m$. The other seven tracks are increments of $0.5\mu m$ on the $1\mu m$ track. They are all $10mm$ long and the thickness of the material that needs to be characterized is $200nm$. The TiN needs an additional Ti layer of $40nm$ under it for adhesion purposes. The track ends with two Al covered bonding pads at each side. Aluminium bond wires are used to connect the die to the printed circuit board (pcb). The pcb is only used as an adapter for the measurement equipment.

The processing steps of the TiN version are as follows [38]: the substrate is a 100 p-type Si wafer of $525\pm 15\mu m$ thick and with a diameter of $100mm\pm 0.2mm$. It has a resistivity of $2 - 5\Omega \cdot cm$. The isolation layer consists of silicon nitride (Si_3N_4) and was deposited using



(a) A photo of the test die bonded to a printed circuit board (pcb) that has been used for most of the measurements (b) Artistic impression of the test die with pcb which shows the 9 parallel lines changing in width from $1.0\mu\text{m}$ to $5.0\mu\text{m}$ in increments of $0.5\mu\text{m}$

Figure 4.1: The test die

Low Pressure Chemical Vapour Deposition (LPCVD). This layer is 500nm thick. The Ti and TiN layers are deposited using Physical Vapour Deposition (PVD) techniques using a Sigma 204 (Trikon) DC magnetron sputtering machine at 300°C with a base pressure of $1.332 \cdot 10^{-5}\text{Pa}$ and a working pressure of $0.0133 \cdot 10^{-5}\text{Pa}$. Both TiN and Ti use a 99.999% high-purity Ti target for sputtering. The vacuum chamber is filled with nitrogen of 99.99% purity and argon of 99.9% purity in order to deposit the TiN layer. The distance between the Ti target and the wafer is 27.5cm . The thin Ti layer under the TiN is 40nm , the TiN is 200nm thick and an additional sacrificial Ti layer is 100nm thick. The last $1.5\mu\text{m}$ of pure Al that will be the bonding material is deposited similarly at 400°C . The first mask is used in the micro-fabrication process to pattern the Al layer. This patterning is done by wet etching with a PES solution (770ml concentrated phosphoric acid (H_3PO_4 , 85%), 14ml concentrated nitric acid (HNO_3 , 65%), 140ml concentrated acetic acid (CH_3COOH , 100%) and 76ml deionized water). The remaining metal stack (Ti and TiN) is patterned using the second mask and positive photoresist and then etched using Reactive Ion Etching (RIE) in order to have desired widths. The resulting layers are shown in figure 4.2a.

The Al, Ti and Al-TiN versions differ from the TiN version process. The build-up of the layers of these test dies are shown in figure 4.2. The techniques described in the previous paragraph are also used to create the other versions. Only the Al-TiN test die uses another technique to prevent the usage of an extra mask. Al is deposited like the first metal and it is patterned using the same mask used for patterning Ti-TiN metal stack. The only different thing that is done during the exposure process in the exposure machine (*ASML PAS 5500*), is that the same mask is exposed three times before development. In the first exposure the mask is exposed without any shift (displacement). In the second and the third exposure the mask is shifted by $1\mu\text{m}$ in the y-direction, in the upward and in the downward direction, respectively. This will shrink the widths of the each track by $2\mu\text{m}$. For example the $5\mu\text{m}$ line will be reduced to a $3\mu\text{m}$ line, the $4.5\mu\text{m}$ to $2.5\mu\text{m}$ and so on. After these three exposures the wafers were developed and the Al was

patterned to have the desired dimensions. After this the second metal stack (40nm Ti, 200nm TiN and 1.5 μ m Al) is deposited and patterned. The first patterning of Al for bond pads was done using wet etching with PES (described earlier) by the bondpad-mask and the remaining Ti-TiN metal stack was patterned without any shift with the same mask used for patterning the underneath Al. This step was done to ensure that the Ti-TiN metal layer has an uniform coating over the Al underneath as shown in figure 4.2d.

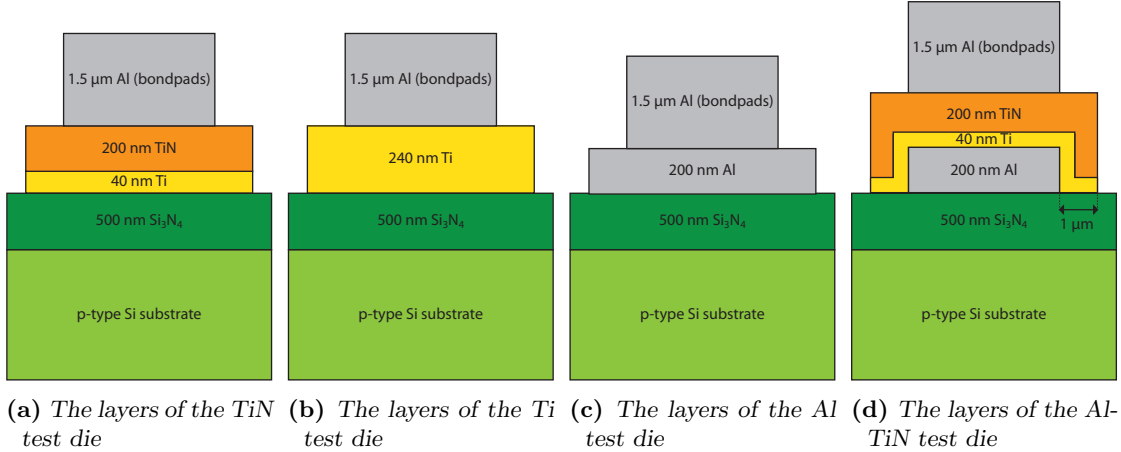


Figure 4.2: The build-up of layers of the different test dies used

In addition to the nine parallel lines there are extended ‘Greek cross’ structures (more about the ‘Greek Cross’ in section 4.9.1). A schematic of a ‘Greek Cross’ with 4 connection terminals is shown in figure C.2, the ones on the test die contain 6 connection terminals (see section 2.2.4 of [39]). These have been added to measure and study the sheet resistance of the TiN-Ti metal stack. They are visible in figure 4.1a, between the ends of the bond wires at the die. The structures can be used to measure the sheet resistance of the material with that particular width. The track in the ‘Greek cross’ has the same width as the track across the complete test die close to it. They have however not been used during the time period of this thesis, because among other things the need for a high precision probe station.

Three wafers of Al-TiN (figure 4.2d) have been micro-fabricated. The first wafer has some adhesion problems with the substrate and aluminium, so it was not considered for measurements. Measurements were done on the other two wafers, where the desired structures are fabricated. The Scanning Electron Microscope (SEM) and regular light microscope pictures show the problem of the first wafer. These pictures are shown in figure D.1. The SEM pictures are taken of one die that has been diced in the y-direction through the centre (see figure 4.1b). Metal delamination for the first wafer occurred due to fabrication problems. The other two wafers - with ID: 1528 and 1530 - have two and three lines of the Al-Ti-TiN stack, respectively. A SEM picture of the widest line that should have a complete width of 5 μ m and an Al-width of 3 μ m is shown in figure 4.3.

It is possible to test the combination of the metal with the (analog of) perilymph by glueing a glass container to the die. The glue that is used is silicon gel and the surface of the glass has been treated with a silicon primer. The top of the glass container can get covered by a Polyvinyl chloride (PVC) cap which has three holes for electrodes and holes for screws to fixate the cap. This final setup is shown in figure 4.4.

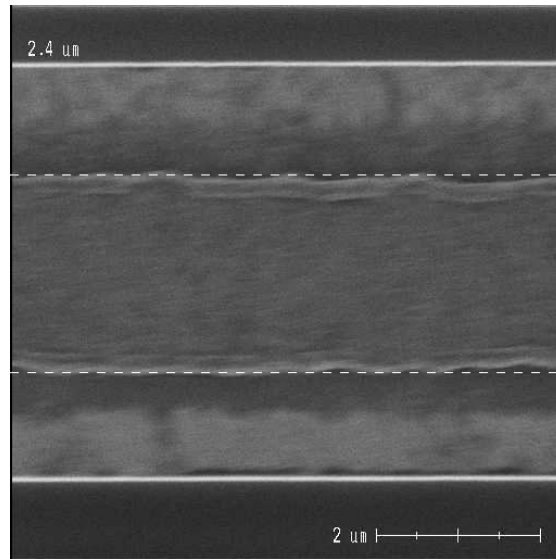


Figure 4.3: SEM picture of the $4.5\mu\text{m}$ line of the Al-TiN test die. It is shown that the width of the Al track is $2.4\mu\text{m}$ and there can be measured that the width of the complete track is $4.5\mu\text{m}$.

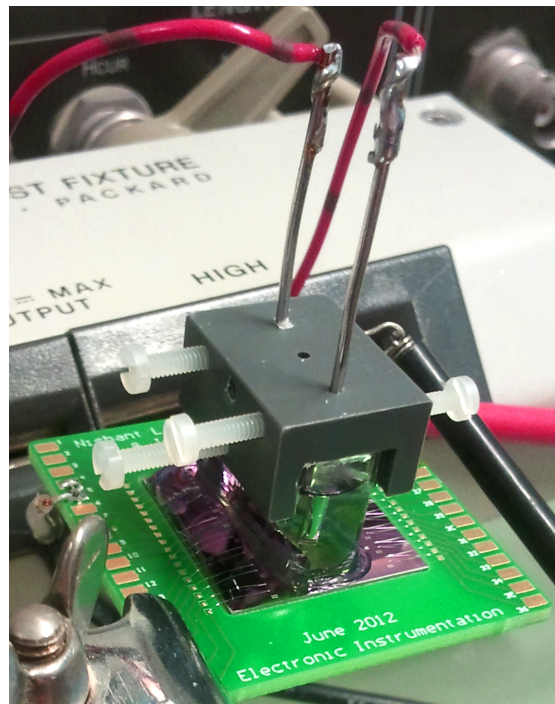


Figure 4.4: The test die with a filled glass container, a PVC cap, two platinum electrodes and screws to fixate the cap

4.2 Impedance

The first measurements that needed to be done were the regular characterization steps for every metal. An impedance measurement is done to see if the metal is purely resistive. If this is not the case, then it could indicate that signals (especially square waves) are distorted due to capacitive or inductive behaviour. It is also interesting to know the sheet resistance of the material to use in further calculations. The impedance characteristics are shown as a Bode plot, including both the impedance and the phase angle. The measurements have been done with a *HP 4194A Impedance/Gain Phase Analyzer* at room temperature, using a short integration time ($500\mu s$), no averaging and a sweep from $100Hz$ to $40MHz$. This is the complete range of the device. A GPIB link from the device to a PC with Labview[®] has been used to transfer the data.

The Bode plots of the four different test dies are shown in figures 4.5, 4.6, 4.7 and 4.8. The characteristics can be modelled as a resistor with a capacitor in parallel. The value of the resistor is the horizontal part of the impedance magnitude in the Bode plot and the capacitor defines the cutoff frequency. The capacitor acts as an open circuit at lower frequencies, but its impedance magnitude decreases with higher frequencies. The cutoff frequency is taken at the point where the phase is at -45° . There was a problem when determining the cutoff frequency for some of the aluminium tracks, because the phase did not get to -45° . The slope downwards was extrapolated at its linear piece to obtain a ‘virtual cutoff frequency’. This gives an indication, but is not as reliable as a real measurement. The modelled resistor and capacitor values of aluminium, titanium and titanium nitride are shown in table 4.1.

The Bode plot of the Al-TiN test die with ID 1530 (figure 4.8) shows that 3 of the 9 tracks have a combination of aluminium and titanium nitride. This can be concluded from the fact that 3 of the tracks have a much lower resistance than the regular titanium nitride test die. The other Al-TiN test die that has been considered (ID: 1528) has only two tracks containing both aluminium and titanium nitride. Its Bode plot is not shown, due to a lack of significance.

The (parasitic) capacitance is mostly from the track to substrate with silicon nitride in between. The change in impedance will not affect the working of the CI, because the cutoff frequency is much higher than the spectrum that CI’s use.

Table 4.1: *The calculated values of the resistances and capacitors of the tracks of the different materials*

Track Width	Al		Ti		TiN	
	$R (\Omega)$	$C (F)$	$R (\Omega)$	$C (F)$	$R (\Omega)$	$C (F)$
$1.0\mu m$			$3.43 \cdot 10^4$	$3.85 \cdot 10^{-11}$	$5.04 \cdot 10^4$	$4.53 \cdot 10^{-11}$
$1.5\mu m$	1488	$3.89 \cdot 10^{-11}$	$2.22 \cdot 10^4$	$3.90 \cdot 10^{-11}$		
$2.0\mu m$	1165	$2.25 \cdot 10^{-11}$	$1.64 \cdot 10^4$	$3.84 \cdot 10^{-11}$	$2.58 \cdot 10^4$	$4.50 \cdot 10^{-11}$
$2.5\mu m$	923	$3.62 \cdot 10^{-11}$	$1.32 \cdot 10^4$	$3.94 \cdot 10^{-11}$	$2.06 \cdot 10^4$	$4.50 \cdot 10^{-11}$
$3.0\mu m$	811	$3.48 \cdot 10^{-11}$	$1.09 \cdot 10^4$	$3.92 \cdot 10^{-11}$	$1.74 \cdot 10^4$	$4.53 \cdot 10^{-11}$
$3.5\mu m$	705	$2.55 \cdot 10^{-11}$	$9.32 \cdot 10^3$	$3.90 \cdot 10^{-11}$	$1.49 \cdot 10^4$	$4.36 \cdot 10^{-11}$
$4.0\mu m$	610	$2.46 \cdot 10^{-11}$	$8.11 \cdot 10^3$	$4.07 \cdot 10^{-11}$	$1.33 \cdot 10^4$	$4.28 \cdot 10^{-11}$
$4.5\mu m$	518	$2.32 \cdot 10^{-11}$	$7.35 \cdot 10^3$	$4.06 \cdot 10^{-11}$	$1.20 \cdot 10^4$	$3.91 \cdot 10^{-11}$
$5.0\mu m$	470	$1.14 \cdot 10^{-11}$	$6.53 \cdot 10^3$	$3.78 \cdot 10^{-11}$	$1.08 \cdot 10^4$	$3.59 \cdot 10^{-11}$

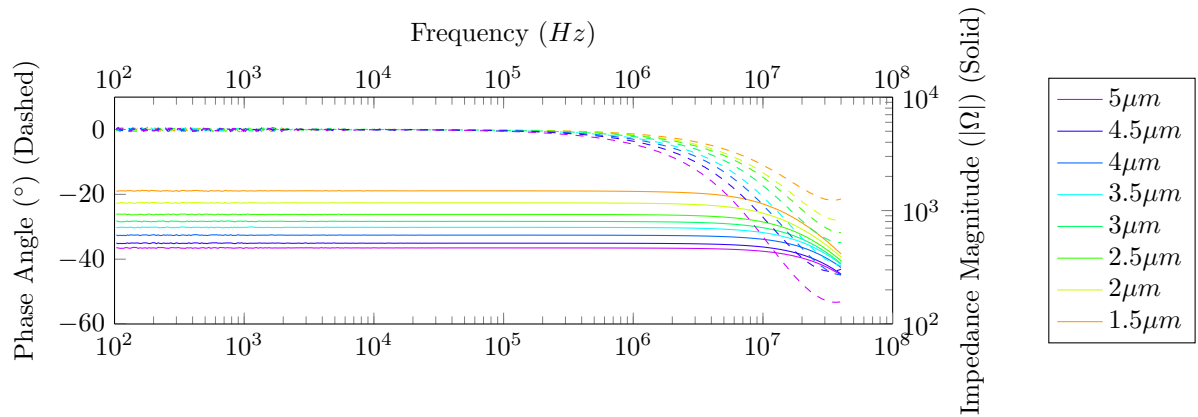


Figure 4.5: Bode plot of the different tracks on the **Aluminium** test die

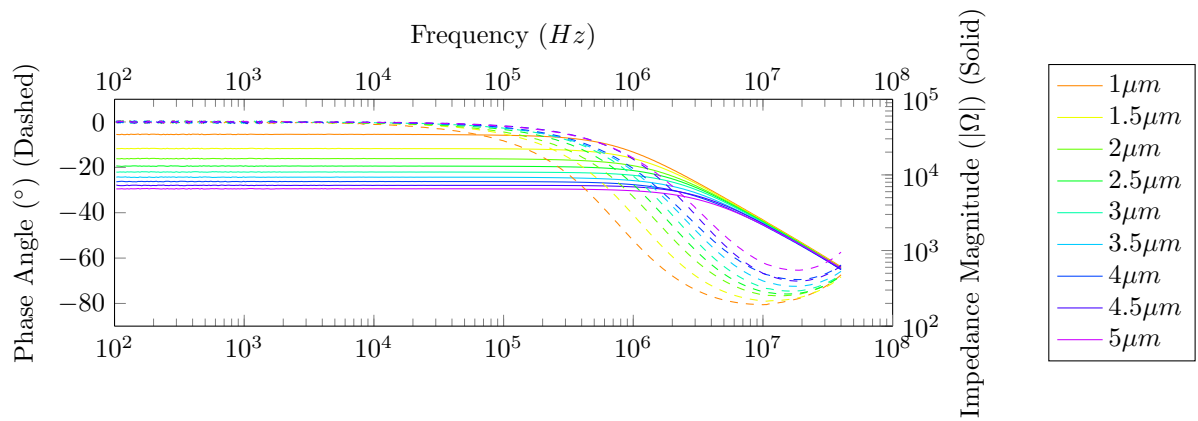


Figure 4.6: Bode plot of the different tracks on the **Titanium** test die

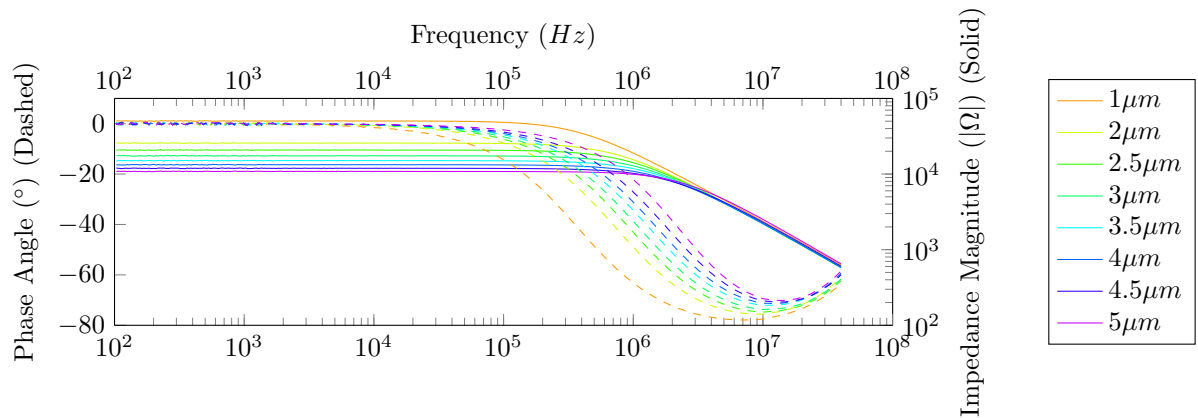


Figure 4.7: Bode plot of the different tracks on the **Titanium Nitride** test die

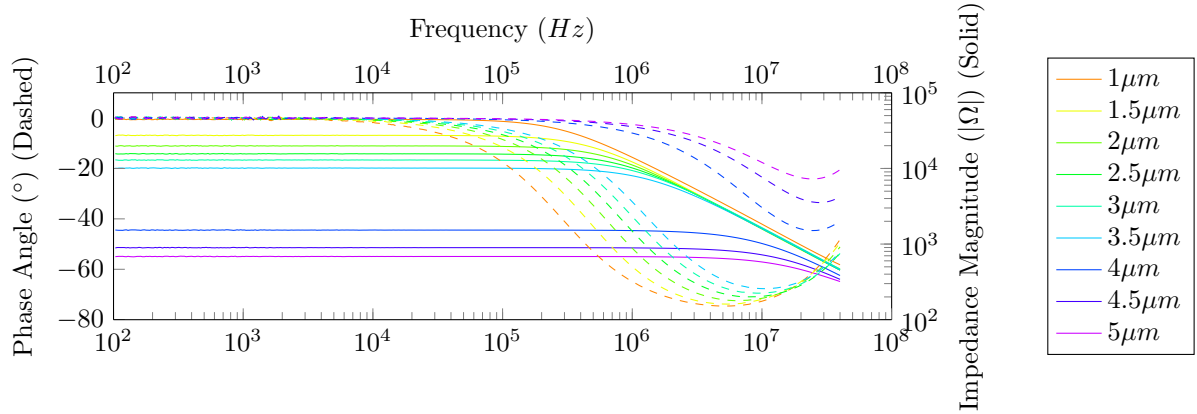


Figure 4.8: Bode plot of the different tracks on the **Aluminium covered with Titanium Nitride** (ID: 1530) test die

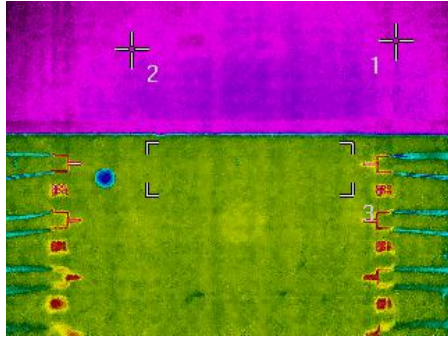
4.3 Joule heating

Another basic material parameter is the self-heating capacity. When a current flows through a material, it will dissipate heat. Every piece of track on the test die acts as a resistor, thus Ohm's law ($U = I \cdot R$) and the power dissipation formula ($P = U \cdot I$) apply. They can of course be combined to $P = I^2 \cdot R = U^2/R$. The temperature of the cochlear implant may not be too high during use, because it will degrade the quality of the surrounding tissue.

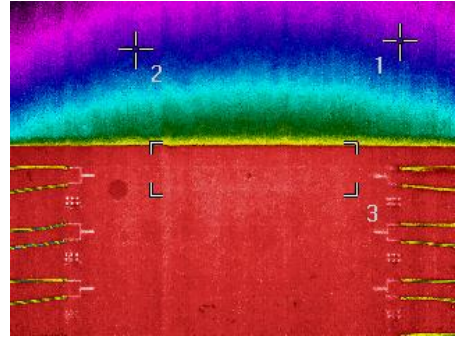
The test die lacks an isolating layer on top of the metal, exposing the tracks to the environment. The final product will have an isolation layer on top of the metal layer, which will spread the heat over a larger area. The measurement has been done with a *FLIR SC305 infrared camera* equipped with a macro lens connected to a computer using an ethernet link. The software *FLIR IR Monitor* is used to extract and analyse the images. Every material was tested using the 5μm wide track of its test die. 27.6V is applied to this track using an *Agilent E3620A Dual Output DC Power Supply*. This created a current of 4mA for the titanium and aluminium and 2mA for titanium nitride. The pictures of figure 4.9 have been extracted before and after applying the voltage. The pictures afterwards were taken after the temperature reached a constant temperature.

It is hard to determine an absolute temperature with an infrared (IR) camera, because there are many dependencies such as the defraction index of the materials, the amount of light in the room and the reflection of the lens. When all of these dependencies stay the same during a measurement and only the temperature changes, it gives an indication of the rise in temperature due to Joule Heating. This is 2.6°C for aluminium, 2.1°C for titanium and 1.7°C for titanium nitride.

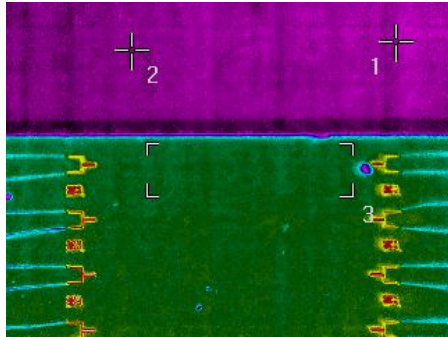
The voltage that has been applied in this measurement is not used in CI nowadays, especially not in DC. AC signals will also dissipate heat, and the Root Mean Square (RMS) values are used then in the formulas above. There will be DC when transistors are added to the design of a CI. They need a DC supply voltage and ground and the challenge will be to design a circuit that is able to deliver enough charge to the nerve, but will not give a rise in temperature.



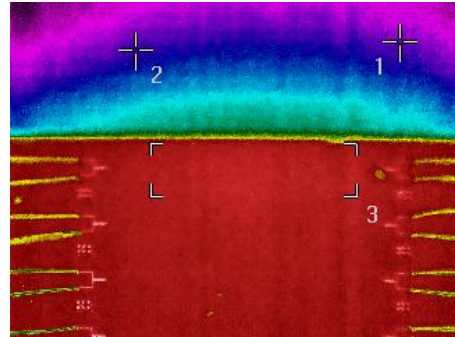
(a) Infrared picture of the **Aluminium** test die before applying a voltage



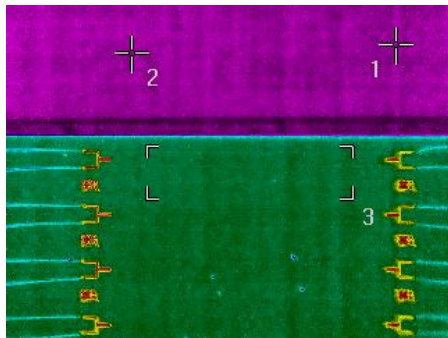
(b) IR picture of the **Aluminium** test die after applying a voltage, the temperature in square 3 rose from 27.5°C to 30.1°C , while the reference temperatures 1 and 2 were the same



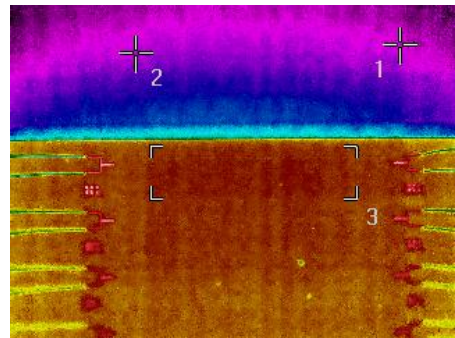
(c) IR picture of the **Titanium** test die before applying a voltage



(d) IR picture of the **Titanium** test die after applying a voltage, the temperature of the test die increased from 27.5°C to 29.6°C , the reference temperatures were also the same



(e) IR picture of the **Titanium nitride** test die before applying a voltage



(f) IR picture of the **Titanium nitride** test die after applying a voltage, this temperature increased from 27.4°C to 29.1°C , having the same reference temperature

Figure 4.9: Infrared pictures of the three different test dies used in this test

Other (smaller) tracks have been observed with the IR camera too, but the increase in temperature was minimal. This is of course logical, because $P = U^2/R$ and the voltage is kept the same, but the resistance of smaller tracks is higher.

4.4 TCR

The Temperature Coefficient of Resistance (TCR) determines the relation between resistance and temperature. Background information about this subject can be found in section 3.1.2. The three different test dies have been used to determine the coefficient for each material.

A *Yokogawa GS200 DC voltage/current source* with a GPIB link to Labview[®] and a *Binder FD53 Drying/heating oven* have been used to obtain reliable results. A current sweep from zero until the voltage limit of 30V is reached is done at different temperatures. The current step size can be adjusted in the Labview[®] front panel. Materials with a higher resistance have a smaller step size to achieve the same amount of steps per material.

The current is applied through two of the four connections of a track at the test die. The voltage is measured at the other two connections of the track. This four point measurement makes sure that the measured voltage is only the potential difference over the track. The measurements are done per test die and it is possible to switch between the tracks with the use of a knob. The applied current is plotted against the measured voltage. Ohm's Law tells us that: $U = I \cdot R$, so the slope of the (linear) graph is the resistance. The slope is obtained using the fit function of Matlab. The TCR is then calculated using equation 3.6 by plotting the calculated resistances against the temperatures. These graphs are shown in appendix D.2. The results are shown here in table 4.2.

Table 4.2: The TCRs of the different test dies ($^{\circ}C^{-1}$)

Track width	Aluminium	Titanium	Titanium Nitride
1.0 μm	$3.845 \cdot 10^{-3}$	$4.651 \cdot 10^{-3}$	$5.826 \cdot 10^{-4}$
1.5 μm	$3.656 \cdot 10^{-3}$	$4.559 \cdot 10^{-3}$	$5.818 \cdot 10^{-4}$
2.0 μm	$3.572 \cdot 10^{-3}$	$4.504 \cdot 10^{-3}$	$5.840 \cdot 10^{-4}$
2.5 μm	$3.588 \cdot 10^{-3}$	$4.457 \cdot 10^{-3}$	$5.852 \cdot 10^{-4}$
3.0 μm	$3.493 \cdot 10^{-3}$	$4.417 \cdot 10^{-3}$	$5.867 \cdot 10^{-4}$
3.5 μm	$3.311 \cdot 10^{-3}$	$4.385 \cdot 10^{-3}$	$5.871 \cdot 10^{-4}$
4.0 μm	$3.3 \cdot 10^{-3}$	$4.352 \cdot 10^{-3}$	$5.915 \cdot 10^{-4}$
4.5 μm	$3.223 \cdot 10^{-3}$	$4.321 \cdot 10^{-3}$	$5.967 \cdot 10^{-4}$
5.0 μm	$3.333 \cdot 10^{-3}$	$4.302 \cdot 10^{-3}$	$6.050 \cdot 10^{-4}$
Average	$3.5 \cdot 10^{-3}$	$4.4 \cdot 10^{-3}$	$5.9 \cdot 10^{-4}$

The results should all be the same per material, but both Ti and Al show relative large differences between the different track widths. Titanium nitride is showing linear results and has a relatively low TCR, which is favourable for a lot of applications. Aluminium changes its resistance with an increase of the current, probably due to self-heating. This is shown in figure 4.10. The notable increase in resistance of Al is probably due to self-heating, because the current is much higher than supplied to Ti and TiN and each measurement took more time. Section 4.3

also showed the largest temperature increase of Al due to self-heating.

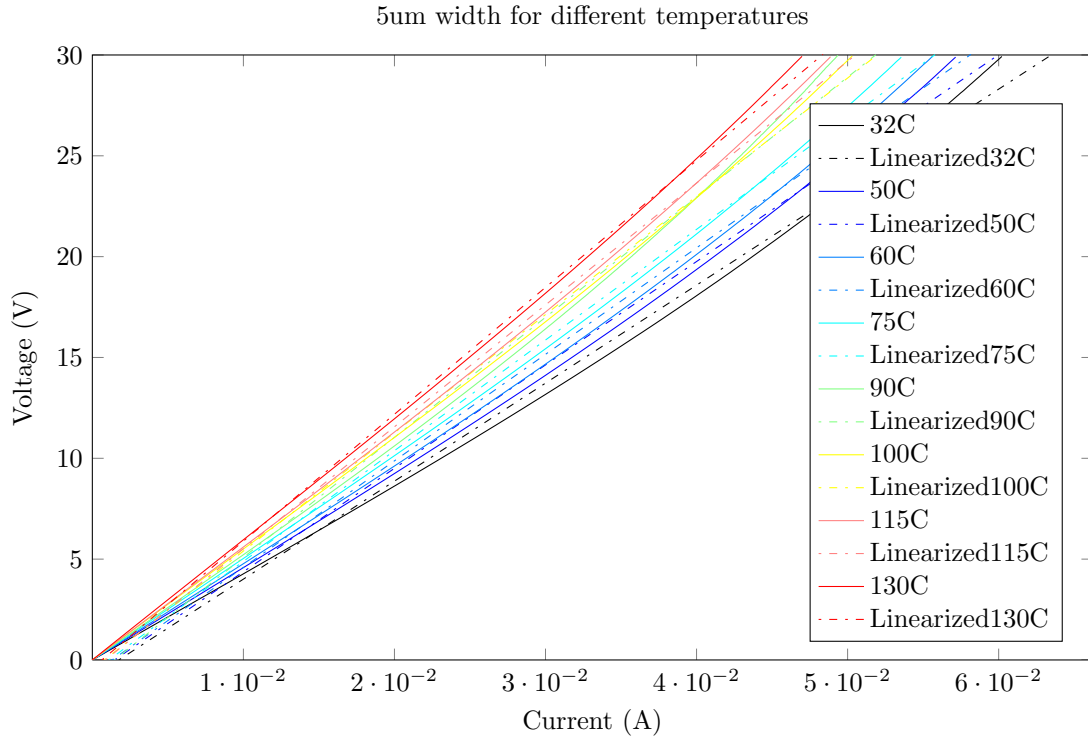


Figure 4.10: The current-voltage relationship of the $5\mu\text{m}$ track of an Aluminium test die is not linear and can be a cause of the differences in TCR in table 4.2

4.5 Electromigration

The phenomenon of electromigration is tested by passing current through the smallest (the $1\mu\text{m}$) track. The smallest track is chosen because of the high current density even though the heat dissipation stays low. This is relevant, because a failure due to a too high temperature is not the purpose of this test.

The test has been done with the three materials using the *Yokogawa GS200 DC voltage/current source* and *Binder FD53 Drying/heating oven*. The GS200 is controlled and monitored using Labview[®] through a GPIB connection. The test die is put in the oven at a constant temperature and current. The measurement stops when the voltage hits 30V , the maximum of the GS200. At this point the track will be interrupted.

Both titanium and titanium nitride did not show any problems after a week of applying approximately 28V (due to a constant current) and 37°C . The titanium nitride was also exposed to higher temperatures, but apart from the higher potentials due to the TCR, there was no effect. Aluminium did break down after 3.5 days of passing 1.1mA (current density of $5.5\frac{\text{mA}}{\mu\text{m}^2}$) and the last 30 minutes are shown in figure 4.11. The first damage to the track was done at 500s , a slight

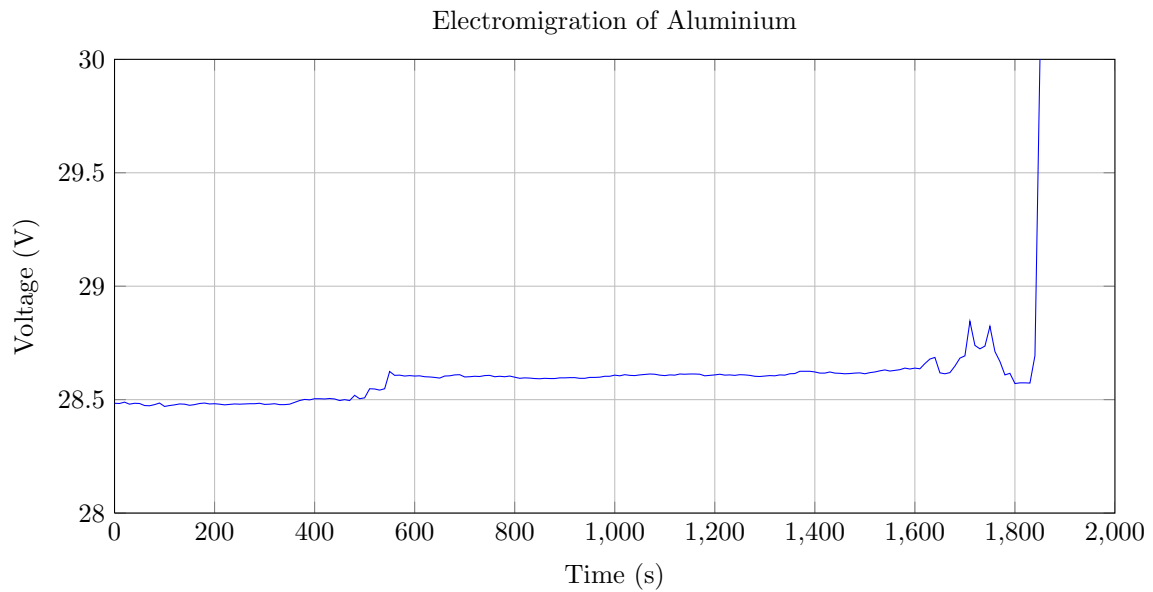


Figure 4.11: Last 30 minutes of the electromigration test on aluminium, please note that the measurement was running for 3,5 days, so there is an offset of $3 \cdot 10^5$ s. This period can be fitted with the following equation (t in hours): $V = 0.0013574 \times t + 28.4508$

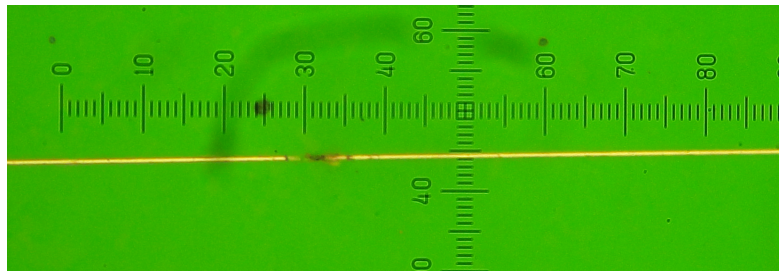


Figure 4.12: Microscope image of the damage due to electromigration

increase in the potential was the result of that. A part of the track is missing, but there is still a direct connection. However, the current density at the location of the damage is higher than before, so fatal damage will occur faster. This can be observed between 1600s and 1900s: the line breaks down after some spikes. These spikes show the physical movement of the track due to the electric field, but the first two movements did not result in the fatal breakdown. A picture using a regular light microscope has been made to verify the breakdown. This picture is shown in figure 4.12.

The second Al-TiN wafer (ID: 1528) was too subjected to an electromigration test. Due to the fabrication nature of this wafer, the $1\mu\text{m}$ could not be used, as in the other electromigration tests. The widest and first to widest track have been used during the test. The current that has been supplied to the widest track was at first 30mA , but reduced to 20mA (a current density in the aluminium of about $33.3 \frac{\text{mA}}{\mu\text{m}^2}$) due to the exceeding of 30V . 20mA is much higher than the first electromigration tests and it resulted in a large potential difference due to the self-heating

(as shown in figure D.5) and fast results. The aluminium was damaged under the titanium nitride, resulting in large potential steps as shown in figure 4.13. From this can be said that the measured voltage never is constant over time, this is due to the electromigration too. The electrons are moving fast, taking aluminium ions with them, creating narrower tracks.

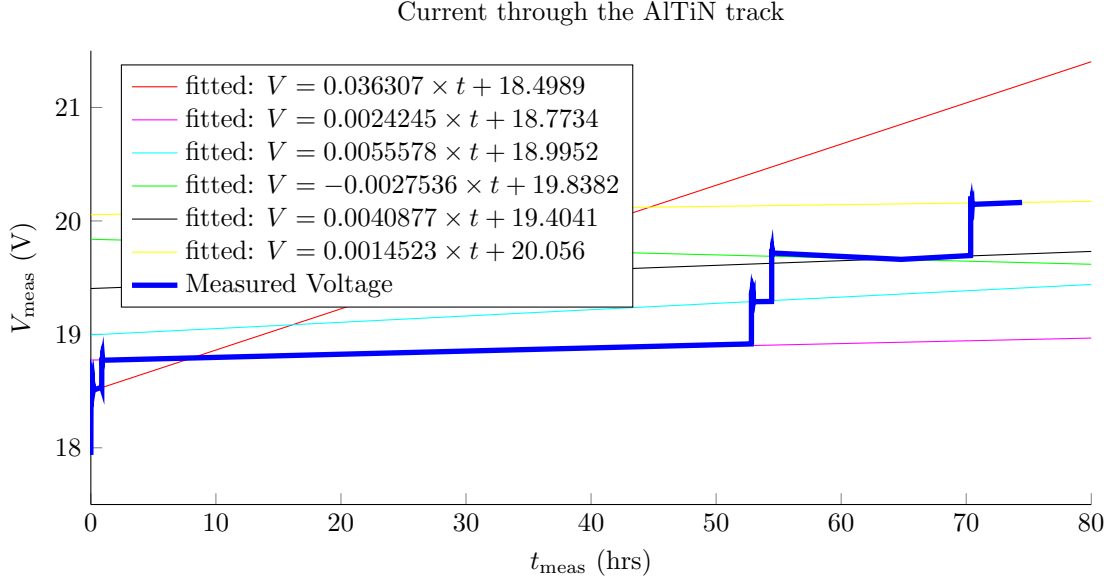


Figure 4.13: The measured voltage of the $5\mu\text{m}$ Al-TiN track with curves of the parts that can be fitted with a first order polynomial. A current of 20mA was supplied to this track. A measurement with 30mA that took 26 hours was done in advance, but it is not shown in this figure (it is shown in figure D.6). This measurement was done at 37°C .

The track was checked visually with a microscope after this test. There was, however, no significant visual damage to the track, because the (damaged) aluminium is covered with titanium nitride.

4.6 Electric field

The electric field distribution in the saline solution is dependent on some factors: the potential of the metal, the dimensions of the electrode (or track in this case), the thickness of the isolation layer on top of the metal layer (which is missing for the test die) and the dielectric constant of the saline solution. Furthermore, the location of the metal track relative to the die is a factor. The track can be completely embedded in the silicon, which might create a very directional electric field, or the top of the track can be aligned with the top of the silicon (planar). These two options require the wafer to be etched and the silicon to be undoped (not conducting) or that an extra isolation layer deposition is needed. The last option (protruded) is that the track is placed on the surface of the wafer, as the test die.

The three options proposed in the previous paragraph are not feasible to measure in real life, but are ideal to simulate. These simulations have been done using *Comsol Multiphysics 4.2a* [40]. A cross section (2D) of a stiff probe (see section 2.3.1) has been taken as the model for

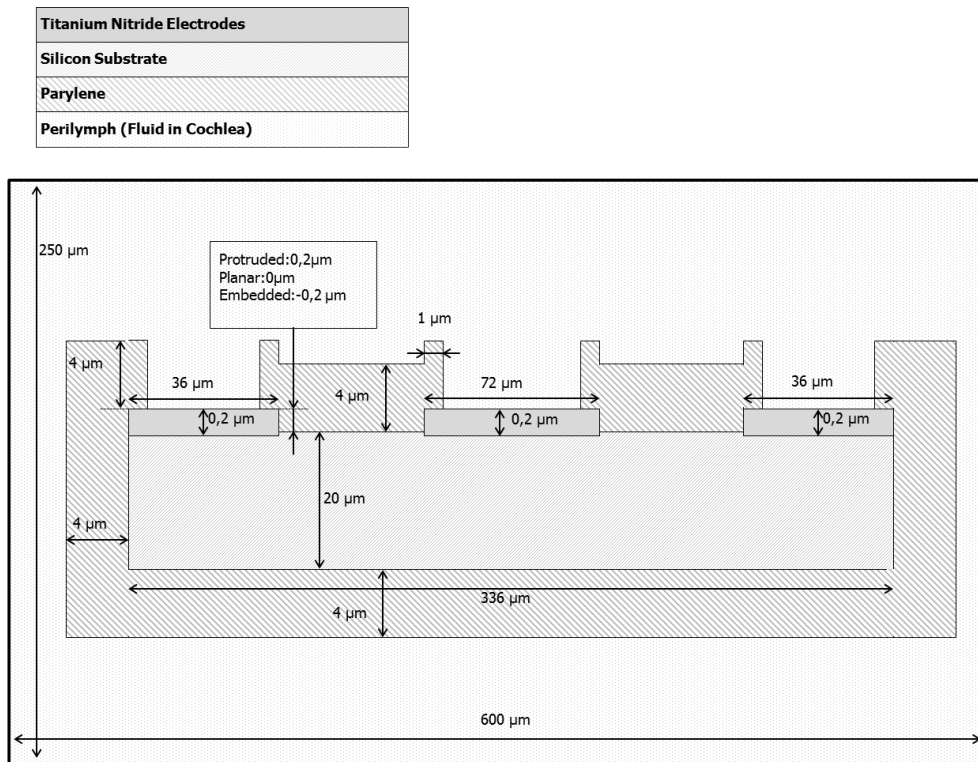


Figure 4.14: The scaled model of a cross section of the stiff probe that has been used to simulate the electric field

simulating. This cross section involves one complete electrode site in the centre and two halve electrodes at the sides, like shown in figure 4.15. The electrode array continues at both sides, but is modelled here as an isolating layer that covers the sides. The complete model with dimensions is shown in figure 4.14.

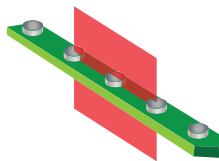


Figure 4.15: Unscaled model of the end of the stiff probe. The red square marks the cross section that has been used for the simulation

This model involves Parylene [41], an isolating material that can be deposited on electronics or other materials. It is biocompatible and can be processed using CMOS-compatible techniques. The substrate is the undoped silicon as mentioned above, it will not conduct any electricity. The metal used in the electrodes is Titanium Nitride, but for this Comsol simulation it does not matter what material is used. It is a static simulation, so no current is flowing and the domain that is put on a potential consists of all edges of the electrode. The model of the electrode array is put in perilymph, which is modelled as a box with a certain relative permittivity and conductivity. All of the materials have

these parameters in order to do the simulation and they are listed in table 4.3.

The simulations have been done using the AC/DC module of Comsol Multiphysics 4.2a, specifically the *Electric Currents (ec)* physics. This physics has some predefined nodes: current

Table 4.3: Material parameters used in the Comsol simulation

Material	Electrical Conductivity σ (S/m)	Relative Permittivity ϵ_r
Silicon (undoped)	$4.3 \cdot 10^{-4}$	11.7
Titanium Nitride	$5 \cdot 10^3$	100
Perilymph	2	50
Parylene (HT)	$5 \cdot 10^{-20}$	2.2

conservation, electric insulation and initial values. The electrode array was set up in the monopolar configuration (see section 2.2), so one electrode is stimulated and there is an extracochlear electrode. The latter is modelled as a grounded bottom boundary, i.e. a ground node is added. A potential of $544mV$ is put on the centre electrode to evaluate the electric field using an electric potential node.

To see the difference between the three options (embedded, planar and protruded) a *parameter sweep* is used. The parameter sweep simulates the three options in one go, creating the possibility to extract figures with the three results in one graph. The dimensions of the model are shown in figure 4.14. The dimension that has been used for the parameter sweep is marked with the box with three options.

Before a decent simulation can be done, a mesh with sufficient elements needs to be created. Meshing of models with high aspect ratios, like the one described here, can be problematic, because the difference between the smallest dimension ($200nm$) and the largest ($600\mu m$) is very big. This means that both relatively large elements and very small elements need to be created. That is why a free triangular mesh is chosen with a maximum edge size of $40.2\mu m$, a minimum size of $5nm$, a maximum element growth rate of 1.2, resolution of curvature of 0.3 and a resolution of narrow regions of 1. In that way the relatively thin electrodes and the regions around the corners are sufficiently meshed. The final mesh is shown in figure 4.16. It can be observed that the electrodes are meshed with a lot of elements and the elements increase in size when they are further from the array due to the growth rate. Minimum element size gives the option of having sufficient meshing at the corners. Narrow regions like the electrodes are meshed correctly, because the resolution of narrow regions is 1, it is a factor between 0 and 1, where 1 gives the highest resolution. There are no curved boundaries, so the resolution of curvature (also a factor between 0 and 1) does not contribute to this model.

The simulation is done using a stationary solver with a parametric sweep of the three options. The configuration of the solver is kept with its default values. When the simulation has finished, there are some ways to extract the data. One is the model with an overlay of the electric field and the potential. This is shown in figure 4.17. This shows only one step of the parametric sweep, the protruded version in this case. In order to compare the electric field distributions of the three versions a 2D graph is created. The data that is used in this graph is the potential of the perilymph at $30\mu m$ from the surface of the silicon substrate. This graph is shown in figure 4.18 and it is clear that the difference in potential distributions is very small. The disadvantages of the extra processing steps needed to etch the substrate determine what design is chosen: the protruded version.

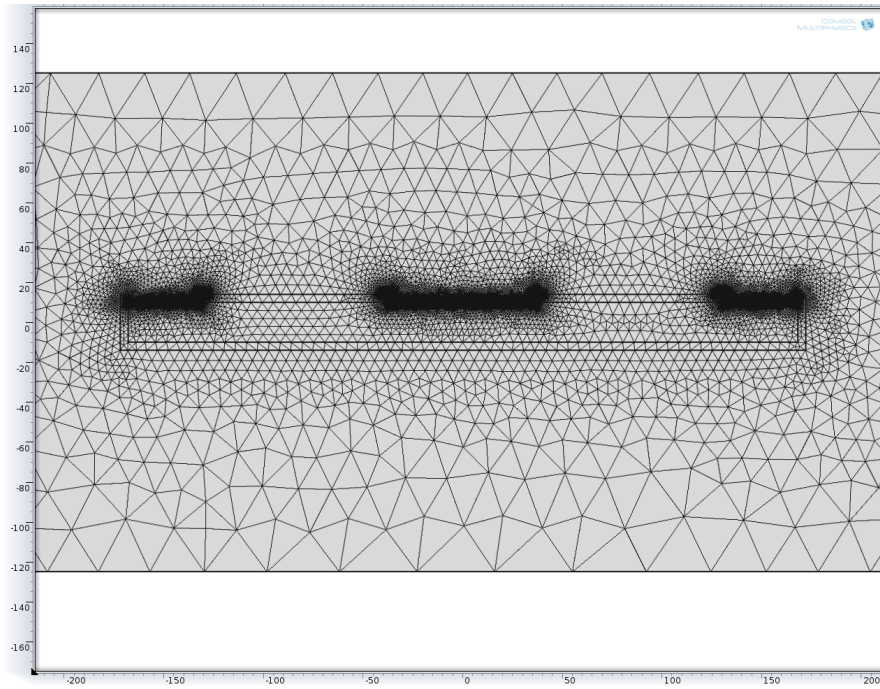


Figure 4.16: The mesh of the model with correct aspect ratios.

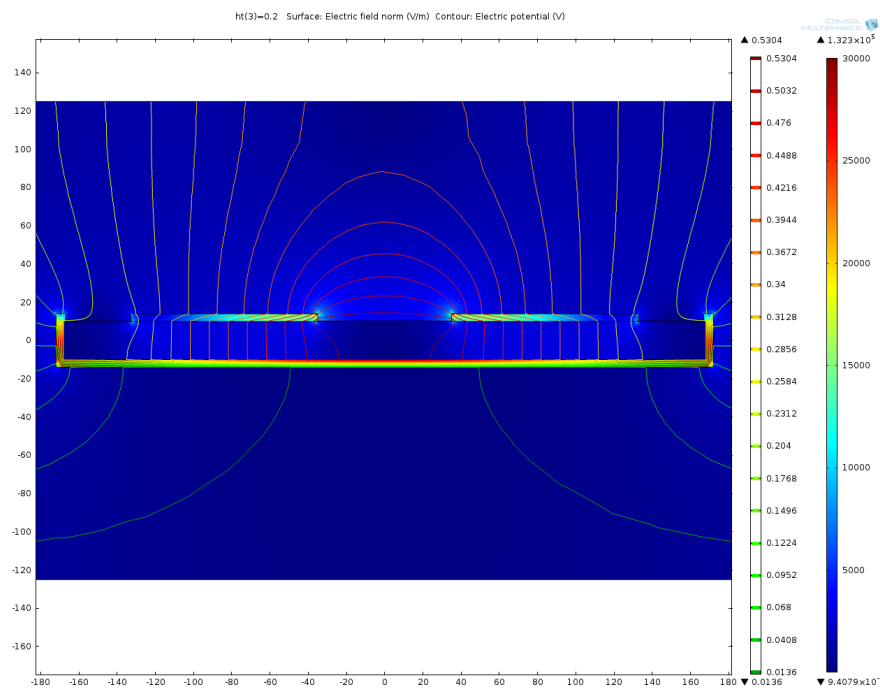


Figure 4.17: Plot of the electric field (surface color) and the potential (contour lines) of the protruded design

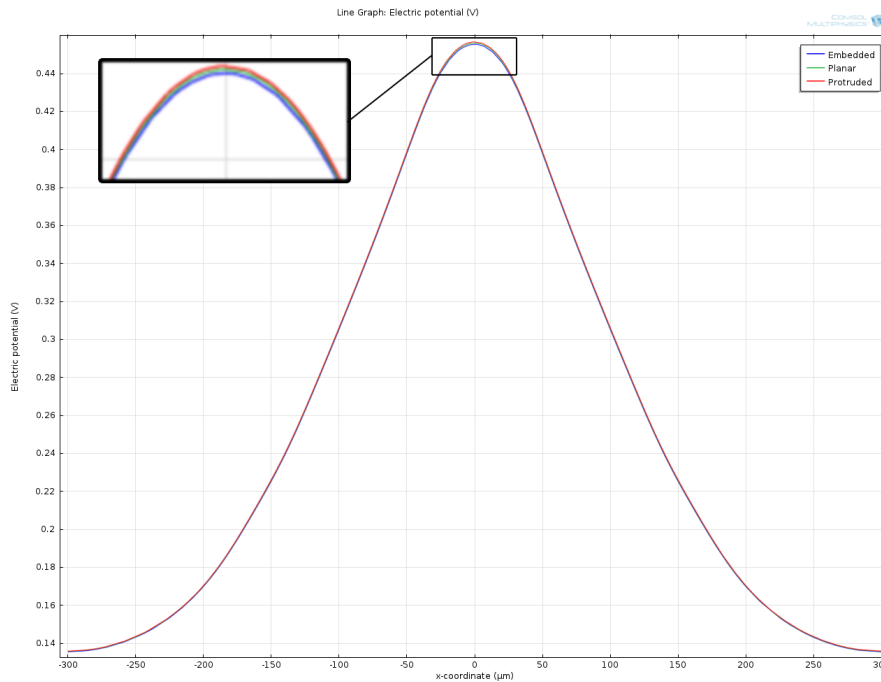


Figure 4.18: *The potential of the perilymph at $30\mu\text{m}$ from the surface of the silicon substrate for the three different designs*

4.7 Voltammetry

Due to the lack of a (reliable) voltammetry setup it was not possible to do a cyclic voltammetry measurement. The small changes in potential require a reliable and highly accurate test environment. It was possible to do a somewhat simpler test, which is described in the next section.

4.8 Endurance

The endurance test is done to observe the reliability of a material in saline solution, since they need to operate in the perilymph of the cochlea. A couple of tests have been done:

1. The impedance of a track of the test die is analysed while being exposed to the saline solution.
2. The impedance of the saline solution is measured while different potential waveforms are applied to a track.
3. The impedance of the interface between the track and an electrode is measured.

All of these tests mimic situations that can happen in real life and failure due to corrosion is likely to occur during the tests. Fatal damage can be detected by measuring the impedance of the track. An intact track can be modelled as a resistor in parallel with a capacitor, but a damaged track is a full capacitor, due to the lack of a conducting path. The impedance of the saline solution might give an indication of a change in dissolved products like the metal of the track. Finally, the test with the interface between the track and electrode is a kind of voltammetry, because a current flows from the test die to an electrode.

The saline solution is created by mixing 9 grams of kitchen salt (NaCl) with 1 liter of demineralized water. This mimics the amount of sodium ions in perilymph. The glass container on top of the test die holds 1 ml of a fluid. The saline solution does not cover all of the tracks on the test die, the glass container and its glue cover the 4 outer lines. The $1\mu\text{m}$, $1.5\mu\text{m}$, $4.5\mu\text{m}$ and $5\mu\text{m}$ tracks are not exposed to the saline solution. These are not considered during measurements, the $3\mu\text{m}$ is used most of the times.

The first two tests have been done using the *HP 4194A Impedance/Gain Phase Analyzer* at room temperature, using a short integration time ($500\mu\text{s}$), no averaging and a sweep from 100Hz to 40MHz . Furthermore, a *HP 33120A Function/Arbitrary Waveform Generator* and an *Agilent 34401A 4 1/2 Digit Multimeter* is used for the second and the third test. All of the instruments are controlled using GPIB and Labview.

The first test, measuring the impedance of a track over time, results in one interesting graph. This Bode plot is shown in figure 4.19. It shows the difference between a TiN track in air and in saline solution. The interface between the saline solution and the track introduces an extra parallel capacitor with resistance. This particular test consists of 664 unique measurements and was run for 8 days. All of the results of this test are shown in figure D.7.

The saline solution evaporated during the test and the complete container was empty after about 3 days. The idea was that this evaporation could be compensated by adding some demineralized water when the container got almost empty. The salt does not evaporate, so the amount of salt should stay the same. However, when the water was added, the setup started to leak. The salt got everywhere on the test die, sometimes damaging the bond wires. Damage to the bond wires results in a total breakdown, because they are essential components of the test setup. There was an attempt to seal the area around the glass container, including the bond wires, with Glob-Top [42]. Its low surface tension makes sure that the bond wires do not break when it cures. After curing the Glob-Top, another problem arose: the track got damaged severely after some impedance measurements. Complete parts were wiped away, like shown in figure 4.20. It shows a titanium track close to the inside border of one track. All of the tracks were severely damaged at one side of the test die. The cause of this failure is unknown, but it could have something to do with an electrostatical force introduced by the Glob-Top. These breakdowns are responsible for limiting the lifetime of a test setup to a maximum of one week.

The impedance of the saline solution has also been observed for a week. The addition of a material in the saline solution could introduce a shift in the impedance spectrum. This material might be the metal used on the test die. The bode plot of this measurement is shown in figure 4.22. 1014 measurements have been done until the test setup broke down as explained in the previous paragraph. The figure does show a difference in impedance over time, but this only indicates the evaporation of the water until there is no fluid left. This is observed after about 4 days (marked by the light blue lines), the complete test took 8 days. Some demineralized water was supplied after one day, this resulted in a small decrease of the absolute value of the impedance.

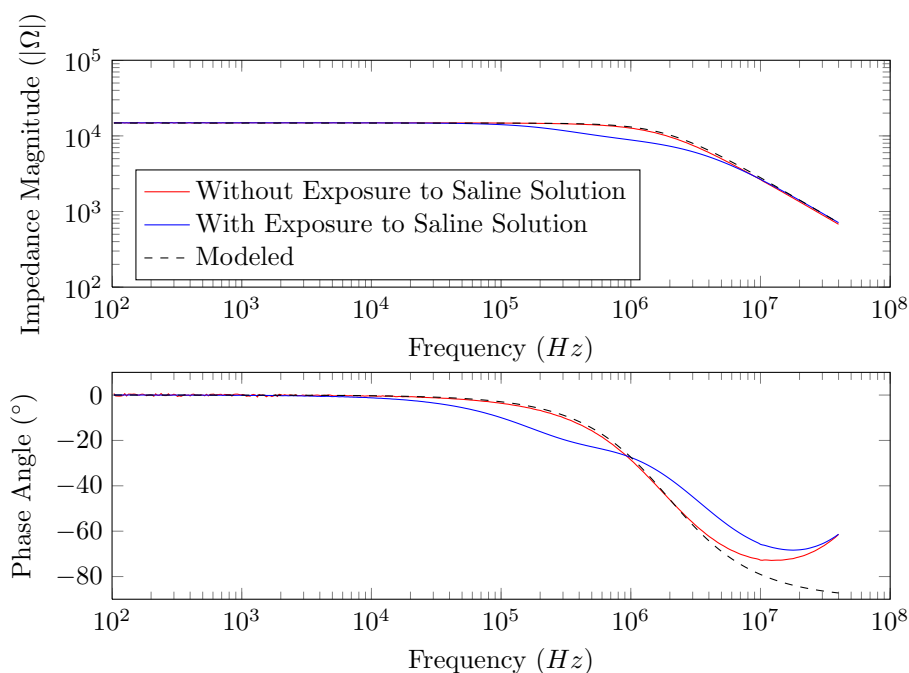


Figure 4.19: Bode plot of the **Titanium Nitride** $3.5\mu\text{m}$ track with and without exposure to saline solution. Also the modelled resistor with capacitor in parallel of the unexposed track is shown.

The metal on the test die, titanium nitride in this case, was stressed extra by applying a potential. After every measurement (about 5 minutes) the waveform of this potential changed. The following waveforms were used during the test:

- Sine
- Square
- Triangle
- Sawtooth (Ramp)

The peak to peak voltage was set to $5V$ and the resulting RMS current is shown in figure 4.23. The test was done at room temperature and this introduces some differences in the measurement due to temperature changes. Most of the times the temperature at night is lower than during the day. The lower last part starts (from 130 hours to the end) at the same time as the complete evaporation of the saline solution.

The current was not completely zero during the measurements, so the track survived the test. No conclusion can be drawn from the impedance spectrum due to the evaporation.

The last test of the three options given in the beginning of this section was done to check if it is possible to pass current from the electrode to the track. This has been done using the function generator and the multimeter. A sine wave was applied between the track (Aluminium in this case) with a peak to peak voltage of $5V$. The resulting RMS current is shown in figure 4.21.

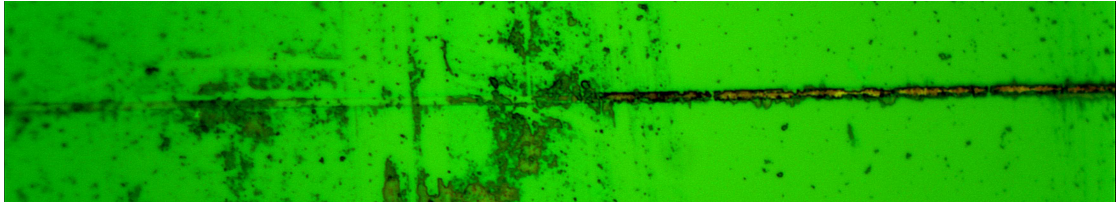


Figure 4.20: Microscope picture of a titanium test die with glass container that has been sealed with Glob-Top after exposure to saline solution and an impedance measurement.

The graph shows that the test was run for about 4 days and that it was possible to pass current from the electrode to the track. The reservoir was regularly refilled during the measurement.

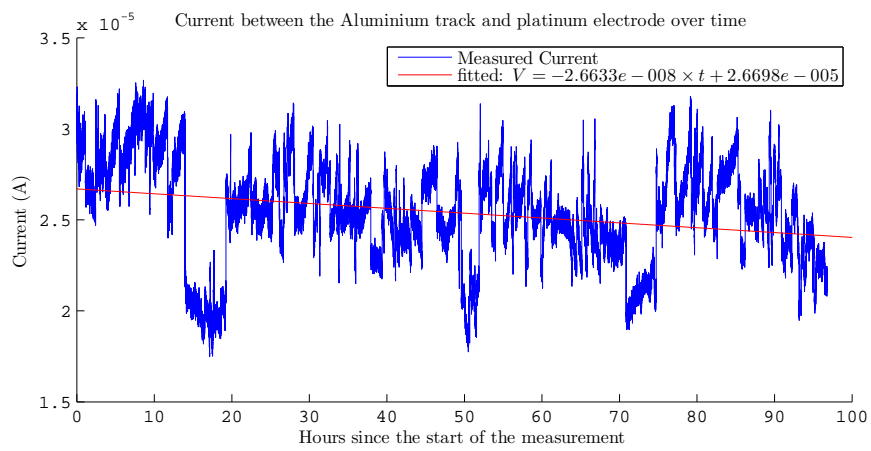


Figure 4.21: The RMS current through the interface Al-saline solution-platinum electrode over time.

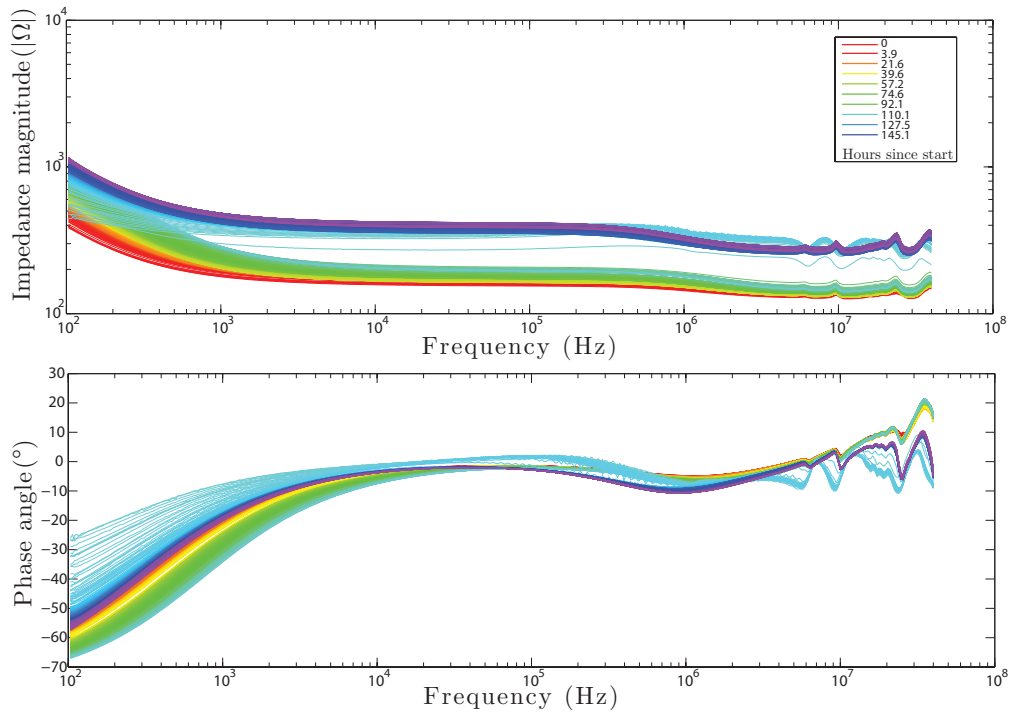


Figure 4.22: Impedance spectrum of the saline solution over time while there are different waveforms applied to the Titanium Nitride track. The red line marks the first measurement, whereas the purple marks the last, as shown in the legend.

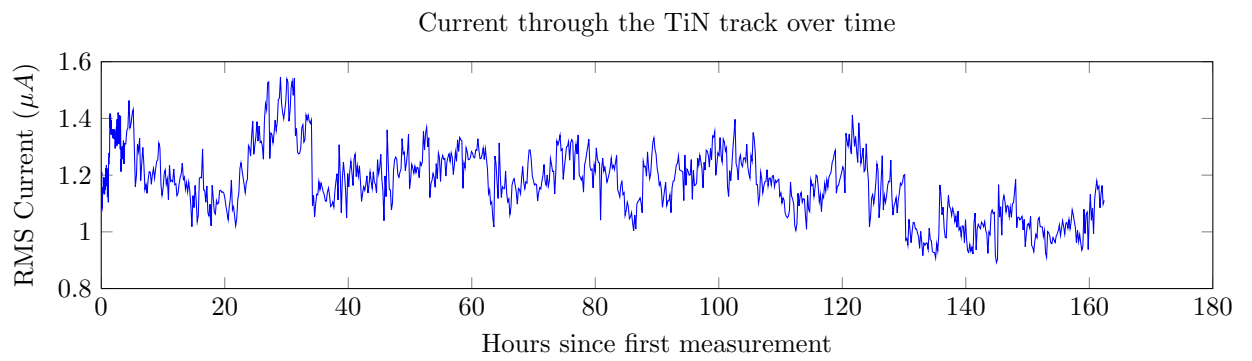


Figure 4.23: The measured current through the $4\mu\text{m}$ titanium nitride track over time during the impedance measurement of the saline solution.

4.9 BiCMOS

The BiCMOS measurements were performed on the die shown in appendix C and it is fabricated as described in section 2.5. The parameters that need to be drawn from the measurements are mentioned in section 3.3.

The measurements were done using a controllable probe station with four probes. These are connected to an *Agilent 4156C Precision Semiconductor Parameter Analyzer* which is also connected to a computer using GPIB. The probe station can be moved in the x-, y- and z-direction using a joystick or its movements can be programmed. The software that is used for the measurements is called *ICCap*.

Three different wafers have been measured, the interconnect metal of two is titanium nitride and one is aluminium. The wafers have also been measured before and after the annealing steps. The TiN wafers were annealed two times, one at standard annealing temperature and one at a temperature of 700°C . The Al wafer was annealed once.

The next subsections describe the different devices of the wafer. The basic structures, Greek Cross and Kelvin Cross, are shown first. These results can be used to discuss the characteristics of the transistors, which are described after that. The oscillator is mentioned in the final subsection.

4.9.1 Sheet resistance

The sheet resistance is measured using the greek cross structures as shown in figure C.2. These structures make it possible to measure the sheet resistance of the different layers of the wafer. A current is passed from the top left pad to the bottom left pad and the potentials of the top right and bottom right pads are measured. The current flows through the centre cross from the top to the left. There is a small difference between the right and bottom due to the cornering current and this results in a measurement of resistance. The sheet resistance can be calculated with equation 4.1 [39]. R_S is the sheet resistance and R is the measured resistance.

$$R_S = \frac{\pi R}{\ln(2)} \quad (4.1)$$

The current is passed using a voltage sweep of V_{force} from -0.5V to 0.5V . The current through that terminal is measured and is called I_{force} . The potentials of the two measuring terminals are measured by keeping the current zero. The result of the sheet resistance measurement is shown in figure D.9a. It shows a noisy result and this could be due to an incorrect accuracy setting. It was, however, possible to fit a line and the sheet resistance is shown in the legend. The greek cross was not only created using the interconnect layer, but also with other layers or combinations of layers as shown in figure C.2. These are also shown in the figures described in this section.

Figure D.9b shows the sheet resistance of a titanium nitride die after the first annealing step. The results are summarized in table 4.4. The reason for showing the graph of another die is simply the large variance in results. Die 9_9 (X_Y) had even worse measurement results before annealing than die 5_9. This could be due to a bad connection between the probes and the interconnect layer. The aluminium wafer did not have as many problems as the titanium nitride. The sheet resistance graph of the aluminium wafer is shown in figure D.10. The sheet

resistance is much lower than that of titanium nitride and the contact resistance (see section 4.9.2) to the SN and SP layers is also lower. The sheet resistance values of the devices other than the Greek Cross of the IC layer should be the same, but the contact resistance is different. The sheet resistance of the SP-NW device has also been measured, but there was no contact between the V_{force} and ground terminal. That was for both aluminium and titanium nitride devices and before and after every annealing step.

The annealing of the titanium nitride at 700°C resulted in very high sheet resistances ($> 10^5\Omega$). This was probably due to the growth of an isolation layer on top of the metal layer which made any contact between the probe and the pad impossible. Trying to break this (isolation) layer by scratching it with the probe and applying a high voltage did still not result in a working device. No further measurements have been done with this wafer.

Table 4.4: Sheet resistance measurement results extracted from figures D.9 and D.10

	R_s of the IC layer (Ω)	R_s of the SN layer (Ω)	R_s of the SN-SP layer (Ω)
TiN before annealing	4.6	0.81	$1.6 \cdot 10^2$
TiN after annealing	3.7	1.7	3
Al before annealing	0.0055	0.12	0.089
Al after annealing	0.00044	0.06	0.031

4.9.2 Contact resistance

The contact resistance is a measure for the resistance between two materials, in this case between the interconnect and the shallow n-type (SN) and shallow p-type (SP) layers. A contact resistance exists due to a bandgap difference between two contacting materials. It can be measured by using a Cross Bridge Kelvin Resistor, as shown in figure C.3. The structure is much like the Greek Cross, only now the current goes from one material to the other in the centre of the cross. The contact resistance can be calculated using the following equation [43]:

$$R_k = R_c + R_{\text{geom}} \quad (4.2)$$

Where R_k is the measured resistance, R_c is the resistance due to the voltage drop of the actual contact and R_{geom} is the resistance due to the voltage drop around the contact opening. Equation 4.2 can be expanded to the next equation:

$$R_k = \frac{\rho_c}{A} + \frac{4R_{sh}\delta^2}{3W_xW_y} \left(1 + \frac{\delta}{2(W_x - \delta)}\right) \quad (4.3)$$

With A the surface of the contact ($30 \times 30\mu\text{m}^2$), ρ_c as the contact resistance, R_{sh} as the sheet resistance of the underlying layer (SN or SP) and δ is the width of the region between the contact opening and the edge of the sidewall of the layers, which is ideally 0, but in this case $5\mu\text{m}$. W_x is the width of the cross section (not the contact opening) in the x-direction and W_y is that for the y-direction, both $40\mu\text{m}$. This results in a R_{geom} of 0.0027Ω for the contact resistance from the interconnect layer to the not annealed SN layer, 0.0013Ω for the annealed SN layer, 0.0020Ω for the not annealed SP layer and $6.92 \cdot 10^{-4}\Omega$ for the annealed SP layer. The sheet resistance measurements of the aluminium wafer have been used, because these data are more consistent.

The results of the contact resistance measurements are shown in table 4.5 and figures D.11 and D.12 for titanium nitride and aluminium, respectively. The titanium nitride wafer shows noisy and inconsistent results again, like the sheet resistance measurements. Figure D.11b is one of the figures that shows that no current flows at all. This results in a very steep fit line, i.e. a high contact resistance. The aluminium measurements are less noisy, but the variance between devices is quite big. The reason of this big variance is not known.

Table 4.5: Summary of results of figures D.11 and D.12

	R_c to SP (Ω)	R_c to SN (Ω)
TiN die 5_9 before annealing	2.6	0.0048
TiN die 6_9 before annealing	2.4	1.4
TiN die 7_9 before annealing	3.4e3	1.8e2
TiN die 9_6 after annealing	6.8	0.0022
TiN die 6_9 after annealing	4.3	0.0035
TiN die 9_9 after annealing	24	0.0085
Al die 9_7 before annealing	0.7	0.0085
Al die 9_8 before annealing	0.53	0.0091
Al die 6_9 before annealing	0.56	0.011
Al die 9_7 after annealing	0.2	0.0075
Al die 9_8 after annealing	0.21	0.0081

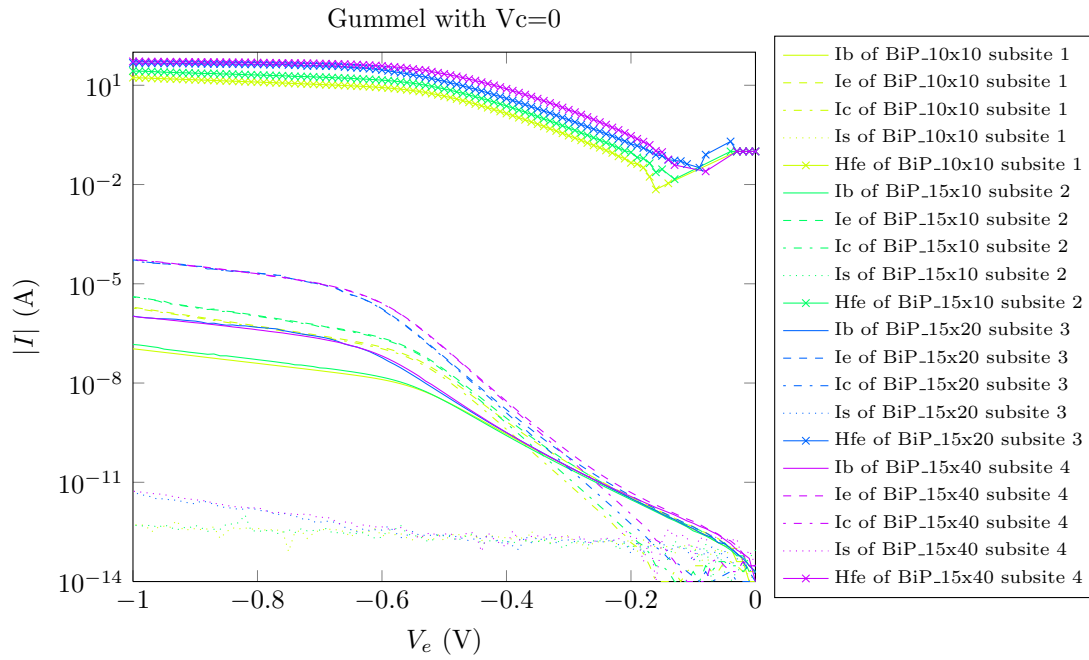
4.9.3 NPN transistor

The npn transistor has been created with multiple contact opening sizes, as shown in figure C.4. A cross section of the device is shown in figure 2.14a. The increase in dimensions should theoretically result in an increase of current through the transistor [44].

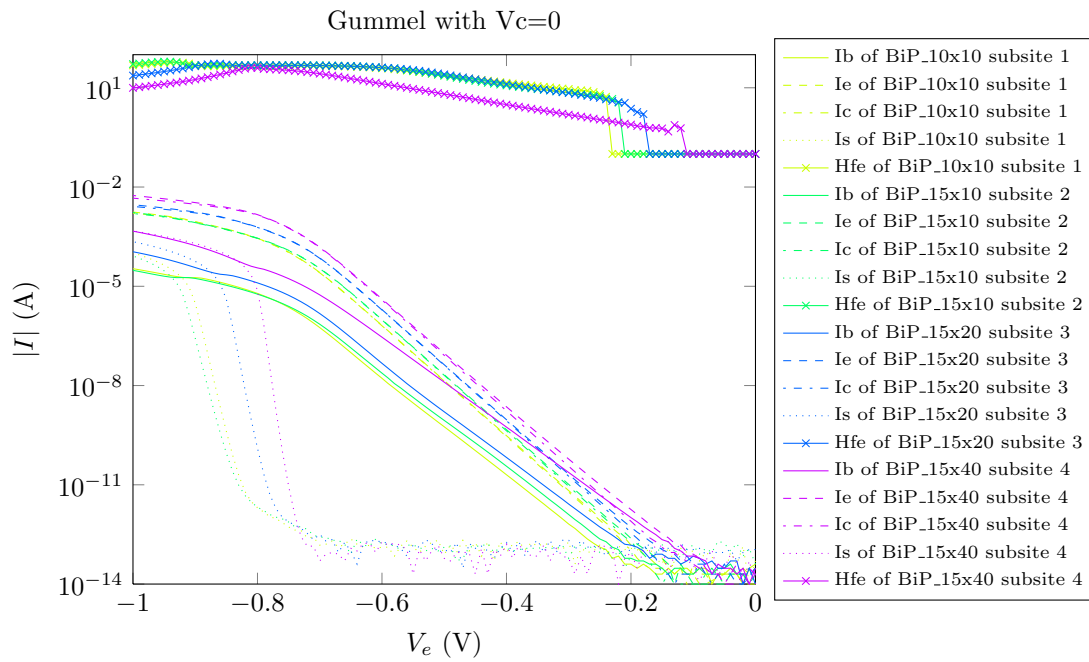
The previous sections have shown that there is a variation between devices and that the measurements of titanium nitride were noisy. This section shows that it is possible to create an npn transistor with silicon nitride as the isolation layer and compares aluminium and titanium nitride as gate material.

Figure 4.24a shows the Gummel plot of the titanium nitride wafer after annealing. The measurement has been done by keeping the base and collector voltage zero. The emitter voltage is forced from 0 to $-1V$. All the currents are measured and shown in figure 4.24a. Figure 2.15a shows the gummel plot of the device with a base size of $15 \times 40 \mu m^2$, but it has silicon oxide as the isolation layer and aluminium as the interconnect metal. The Gummel plot of the aluminium wafer with silicon nitride as the isolation layer material is shown in figure 4.24b. Both figures show that it is possible to create an npn transistor with TiN or Al as interconnect and SiN as the isolation.

The high (contact) resistance of titanium nitride is responsible for the lower current levels than those of aluminium. This also causes the base current I_b to get higher than the collector current (I_c) for emitter voltages (V_e) close to zero. The substrate current (I_s) is low for both devices, only the aluminium transistor has an increased current for emitter voltages close to $-1V$.



(a) Gummel Plot of the npn transistors on the annealed titanium nitride wafer



(b) Gummel Plot of the npn transistors on the annealed aluminium wafer

Figure 4.24: Gummel plots of the titanium nitride and aluminium wafer with silicon nitride as the isolation layer.

4.9.4 NMOS transistor

The layout and cross section of the NMOS transistor are shown in figures C.5 and 2.14c, respectively. Like the npn transistors the NMOS transistor has been designed with different dimensions. Ten different devices have been fabricated with a channel width of $20\mu m$ and $60\mu m$. The channel length increases from $0.5\mu m$ to $10\mu m$. Multiple devices have been measured, but the transistor with a channel length of $2\mu m$ and a width of $20\mu m$ is shown for clarity reasons.

Plots of the currents in the device for a changing gate voltage (V_G) and for a changing drain voltage (V_D) describe the characteristics of a MOS transistor, as described in section 3.3. The transient plots of a V_G sweep from $-5V$ to $5V$ are shown in figure 4.25. Figures 2.15d and 2.15e show the characteristics of the same device, but created with silicon dioxide and aluminium.

Figure 4.25a shows the gate voltage sweep graph of the titanium nitride wafer, which describes a perfectly working NMOS transistor. However, the small extra increase in drain (I_D) and source (I_S) current between a V_G of $-2V$ and $0V$ indicates the existence of an additional transistor. This transistor exists due to the high surface charge of the silicon nitride. It creates an extra channel around the gate which is permanently on. Figure 4.25b shows the V_G sweep of the aluminium wafer. The gate and substrate current, respectively I_G and I_{sub} , are low, as they should be. The source and drain current should also be low for a V_G lower than $0V$, but they are not. This is also due to the silicon nitride, because the device shown in figure 2.15d has better characteristics. To eliminate the extra channel created by the high surface charge, the ring transistor has been implemented too. The gate completely surrounds the drain, so no additional channel can be created. The V_G sweep does show the existence of an additional element nevertheless. The characteristics of the aluminium wafer did improve a lot. These graphs are shown in D.13.

Figure 4.26 shows the relation between the drain voltage and the drain current for different gate voltages. The graphs indicate too that the transistor works. The higher sheet and contact resistance of the titanium nitride is responsible for the lower currents through the device. These plots of the NMOS ring transistors are shown in D.14.

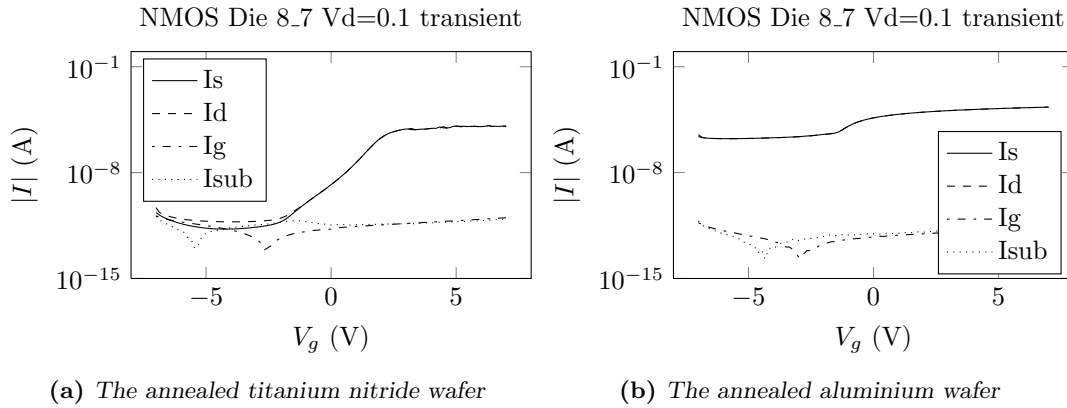
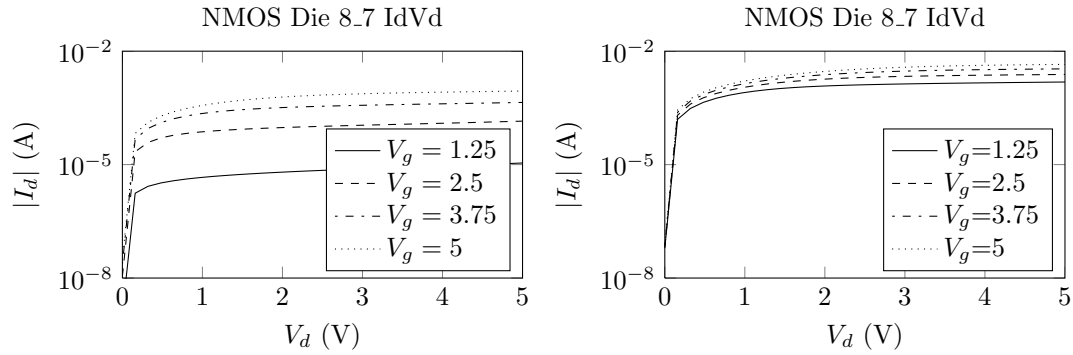


Figure 4.25: Transient plots of the NMOS transistor with a gate size of $20 \times 2\mu m^2 (W \times L)$



(a) The annealed titanium nitride die 8.7

(b) The annealed aluminium die 8.7

Figure 4.26: The drain current I_d for a drain voltage V_d and gate voltage V_g sweep of the NMOS transistor with the following dimensions $W = 20\mu m$ $L = 2\mu m$

4.9.5 PMOS transistor

The PMOS transistor is of course the complementary version of the NMOS transistor. The same plots can be produced from the PMOS. The layout, cross section and reference characteristics are shown in figures C.6, 2.14b and 2.15f, respectively.

Figure 4.27 shows the two graphs of the gate voltage sweep. The trapped surface charge in the silicon nitride is also visible here, because the voltage required to turn on the transistor is much larger than with the silicon oxide as the isolation layer. This is also the reason of the strange results shown in figure 4.28. It is, however, possible to create a moderately good working PMOS transistor with this process.

The PMOS has also been implemented in the ring-form, like the NMOS transistor, as shown in figure C.8. The characteristics are shown in figures D.15 and D.16. Especially the drain voltage sweep shows some more neat results than those shown here.

The high surface charge could be minimized by implanting extra positive charge carriers in the surface of the wafer. This needs to be investigated further.

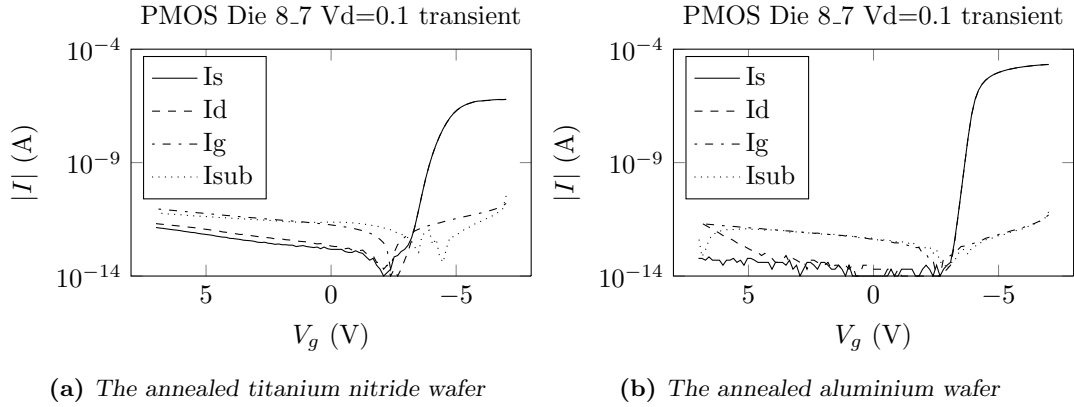


Figure 4.27: Transient plots of the PMOS transistor with a gate size of $20 \times 2 \mu\text{m}^2 (W \times L)$

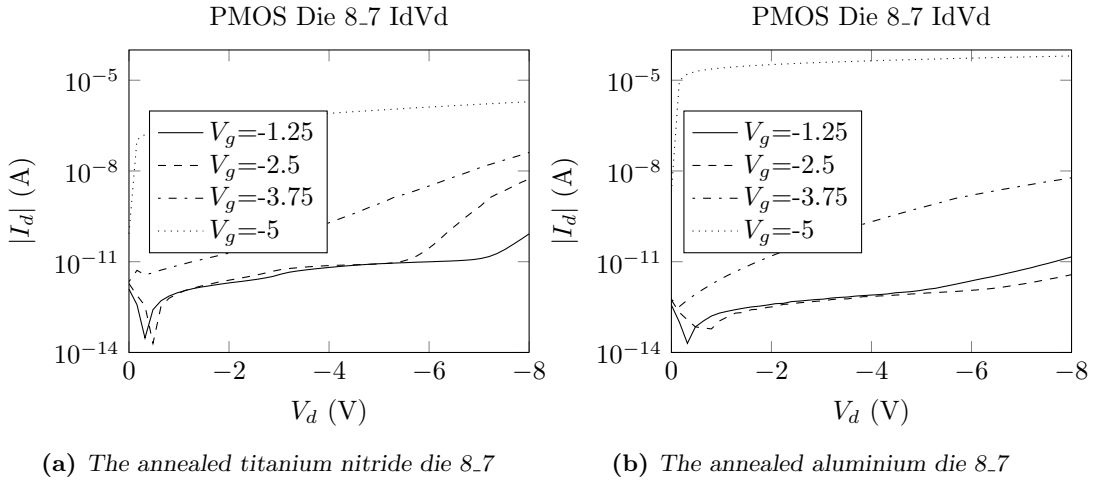


Figure 4.28: The drain current I_d for a drain voltage V_d and gate voltage V_g sweep of the PMOS transistor with the following dimensions $W = 20 \mu\text{m}$ $L = 2 \mu\text{m}$

4.9.6 Inverter

As stated in section 3.3, the inverter should at least work to have a possibility to use the BiCMOS process for larger circuits. The inverter layout is shown in figure C.9 and it is composed of an NMOS and PMOS transistor.

The input voltage V_{in} is swept from 0V to 10V. These values are also applied to the V_{ss} and V_{dd} terminals, respectively. The output voltage and current are shown in figure 4.29. The high surface charge is again responsible for the non-centralized location of the high-to-low section, due to the shift in the threshold voltage. Furthermore, the current in the aluminium inverter is much higher than in the titanium nitride version, because the resistance of the aluminium is still lower than that of titanium nitride.

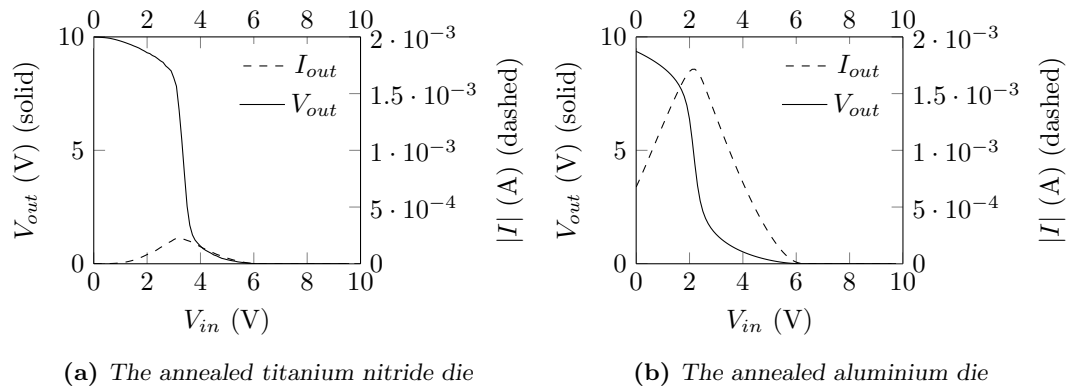


Figure 4.29: Inverter characteristics of die 8.7 with a channel length of $2\mu\text{m}$

4.9.7 Oscillator

The last device that has been tested was the oscillator. The 5-stage oscillator is shown in figure C.10. It has been measured with an oscilloscope, while the V_{DD} terminal is put on $5V$, and the screen shot is shown in figure 4.30. The resulting frequency is 25.71MHz with a peak-to-peak voltage of 644mV .

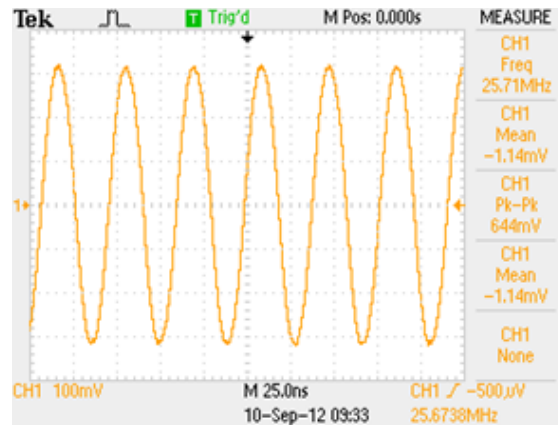


Figure 4.30: The 5-stage oscillator with titanium nitride as interconnect

Chapter 5

Conclusions and future work

The creation of electrode arrays built with CMOS compatible techniques is one step closer after the work that has been described in this thesis. There is, however, still a long way to go until these devices can be used in real Cochlear Implants. This chapter shows what has been achieved and what needs to be done regarding the metals of the electrode array.

The test setup with the 9 parallel lines as shown in figure 4.1 works for simple characterisation of the metals. It is suited to do some reliability tests and measurements with the metal, but another die with real electrode shapes and an isolation layer needs to be designed and manufactured to measure parameters like the charge injection capacity. Such a die contains structures described in section 2.3 and different electrode shapes and sizes. They need to be large enough to deliver enough charge to trigger the hair cells of the nerve endings. The designer of these electrodes must also keep in mind that the amount of electrodes available will increase dramatically compared to the CI's used nowadays, so other stimulation techniques can be used. It is possible then to divide the current over multiple electrodes, limiting the current density per channel.

The glass container made it possible to add a saline solution to the setup, this was however not very reliable. The first steps toward building a more reliable setup have been done, but it was not realizable within the time scope of this thesis. The idea is that the glass container is not used anymore, but that the complete pcb with the test die is submerged in a saline solution. The bond wires and visible parts of the pcb need to be coated in some kind of resin that will not only protect the wires from the saline environment but also has a control over the surface tension of the resin. It will be harder to detect other species in the saline solution, but problems like evaporation and leakage failure will be solved since the proposed setup has a larger amount of fluid.

Not only the setup needs to be changed to do more reliable measurements, the saline solution used in the experiments were not as the standards. Tablets of phosphate buffered saline (PBS) would be an ideal solution to this. It helps to maintain a constant pH during the experiments which mimics the conditions of the human body. This is especially suitable for doing voltammetry measurements, which are important tests for characterizing the electrode arrays. This thesis did not describe these measurements, due to the absence of a voltammetry setup.

The source of the damage as shown in figure 4.20 is unknown. This can be explained by the combined effect of the glob-top, silicone glue, silicone primer, glass, silicon nitride, the titanium (nitride) and the impedance measurement. This needs to be studied to prevent this delamination

from happening in the future.

After characterizing the metals and choosing the most appropriate metal, there should be in-vitro and in-vivo tests. First, the electrode array is exposed to cochleae from dead animals like guinea pigs or cats. These tests are needed to evaluate the placement and biocompatibility with long term stability of the electrode array in the saline environment of cochlea. The final design has to be demonstrated for in-vivo tests in guinea pig cochleae. The regulations and planning for these tests need to be determined at the medical centre in Leiden (LUMC) and are outside the scope of this thesis.

This thesis only describes three metals: aluminium, titanium and titanium nitride. None of these are currently allowed in CI's for human use. The current metal that is used in CI is platinum and/or platinum iridium. These materials are able to be sputtered on a wafer, but the material properties of sputtered platinum (iridium) are different from regular platinum (iridium). They differ in such a way that they might not be able to be used in CI, but that needs to be verified. The use of these already approved metals will speed up the introduction of electrode arrays built with CMOS compatible techniques as described in this thesis.

The resistivity of titanium nitride is very high, which makes it not suitable for longer lines. There is a method to reduce the resistivity of titanium nitride by changing some parameters during the vapour deposition process, by combining low pressure organometallic chemical vapour deposition (OMCVD) and rf plasma oxidation [45]. The width of the track can also be made wider, but this will limit the amount of tracks that can be placed parallel to each other. That is one of the reasons that there is a need for active components in the electrode array. This means that some tracks will need to carry signals with frequencies much higher than audible tones, because more information needs to be delivered over less lines. The capacitive behaviour might distort this information when the bandwidth of the signals is higher than the cutoff frequency. The source of this (parasitic) capacitive behaviour could be a combination of the following factors: the capacitor from the track to the substrate, a contact capacitance from the bond wire to the bond pad or the connection to the impedance analyser. The true source needs to be found and minimized as much as possible.

Another factor that will play a much larger role in the design of active electrode arrays is the power dissipation. The infra-red measurements that have been done in this thesis do not apply to a CI without transistors, due to the absence of DC currents. Short bursts of charge balanced pulses will not increase the temperature much, but the final design must of course be validated with respect to the self-heating of the device. A large variance of signals can be supplied to the electrode array to evaluate the maximum temperature of the device. If the temperature rise is as much as described in section 4.3, then it is not suitable for implantation. It has to be noted that the final design will have an isolation layer along with an biocompatible coating such as Parylene on top of the metal, reducing the dissipated heat to the environment.

As with the self-heating, electromigration will not play a large role in non-active electrode arrays, due to the absence of large DC currents. The titanium nitride did, however, not break down, while the aluminium did. The tests with the aluminium (Al) covered with titanium nitride (TiN) show that the Al still breaks down under the TiN for larger current values which are normally not employed for CI's. From the experiments performed, it was not possible to damage TiN using the current values that were achievable using the equipment. That is an advantage of the harder TiN. Longer or accelerated tests have to be done to confirm the electromigration properties of the TiN.

The Comsol simulations showed that the location of the track does not influence the electric

field distribution much. The extra processing steps needed to etch the trench for the track make it even less beneficial. There are more parameters that influence the electric field and these can be changed to create a more directional electric field. Simulations are suited well to evaluate these parameter changes and the electric field of a combination of electrodes. It is also possible with the ‘Corrosion’, the ‘Chemical Reaction Engineering’ and the ‘Electrodeposition’ module of Comsol to simulate the chemical reactions in the saline solution. The learning curve of software like Comsol is however quite long.

The BiCMOS measurements have shown that it is possible to create npn, NMOS and PMOS transistors with TiN and silicon nitride. This versatile process is a very good candidate for the final design of the future electrode array. There are some deficiencies that need to be solved, like the surface charge of the silicon nitride. This might be compensated by the addition of positive charge, but that will change the device parameters. Other solutions can be considered, like another isolation layer material or other methods to compensate the surface charge.

The contact and sheet resistance of the TiN are high enough to create noisy results. The compliance and accuracy of the measurement setup was inappropriate. Furthermore, the variance between the devices is very big. The source of this variance needs to be studied and eliminated as much as possible. The contact resistance might be reduced by introducing a barrier layer in the contact openings. The barrier layer will make the work function difference smaller between the doped substrate and the interconnect.

The measurements have all been done on a rigid silicon substrate, but the flexible probe will have a flexible polyimide substrate. It is an option to combine silicon and polyimide, by placing the active components on silicon which will be placed on a regular interval, so that the electrode array stays flexible. It will also increase the stiffness, since only polyimide cannot contribute solely to the entire stiffness of the device. Polyimide flexibility will influence both the material and electrical properties: cracks in the metal can occur due to flexing and the dielectric properties of the polyimide are different from silicon nitride. All of the measurements that have been done with the silicon substrate will need to be done with the flexible substrate to evaluate the differences.

This thesis did not describe the possible circuitry needed on the electrode array using the transistors that are described in this thesis. A communication protocol needs to be developed to address a certain electrode and decoder and stimulator circuitry must be designed for the electrode array. The stimulator circuit is in the development phase by a PhD student at the ‘Biomedical Electronics Group’ of the same faculty [46]. This development will take time, but the implementation of active components in the electrode array will be the biggest development since the first CI by Graeme Clark.

In conclusion it can be said that this thesis shows the possible development options towards building electrode arrays with CMOS compatible techniques. More investigation and compatibility tests are to be performed to explore its usability for the future cochlear implants.

Appendix A

Material properties

A.1 Cochlear fluids

Table A.1: *Chemical Composition of Cochlear Fluids [32]*

	Scala Tympani Perilymph	Scala Vestibuli Perilymph	Scala Media Endolymph	Cerebrospinal Fluid
Sodium (mM)	148	141	1.3	149
Potassium (mM)	4.2	6.0	157	3.1
Chloride (mM)	119	121	132	129
Bicarbonate (mM)	21	18	31	19
Calcium (mM)	1.3	0.6	0.023	-
Protein (mg/dl)	178	242	38	24
pH	7.3	7.3	7.4	7.3
Potential (mV)	0	< 3	85	0

A.2 Metals

Table A.2: Material properties of the three metals that have been tested [47]

Property	Titanium Nitride	Titanium	Aluminium
Systematic Name	Nitridotitanium	Titanium	Aluminium
Molecular Formula	NTi	Ti	Al
Molecular Weight	61.89	47.88 +/- 3	26.98154
Crystalline form, properties and index of refraction	yel-bronze, cub	α hex, tr β cub 838, silv gray	silv wh duct met, cub
Density or spec. gravity	5.22	4.5	2.702
Melting point $^{\circ}C$	2930	1660 +/- 10	660.37
Boiling point $^{\circ}C$	n/a	3287	2467
Solubility in cold water (grams per 100 cc)	i	i	i
Solubility in hot water (grams per 100 cc)	i	i	i
Other solvents	sl s hot aq reg + HF	s dil a	s alk, HCl, H ₂ SO ₄ , i conc HNO ₃ h ac. a

Abbreviations			
a	Acid	hex	Hexagonal
ac. a	Acetic acid	i	Insoluble
aq reg	Aqua Regia	met	Metal or metallic
alk	Alkali	n/a	Not available
conc	concentrated	s	Solute
cub	Cubic	silv	Silver
dil	Dilute	sl	slightly
duct	Ductile	tr	Transition point
h	hot	wh	White
yel	Yellow		

Appendix B

Anatomical terms

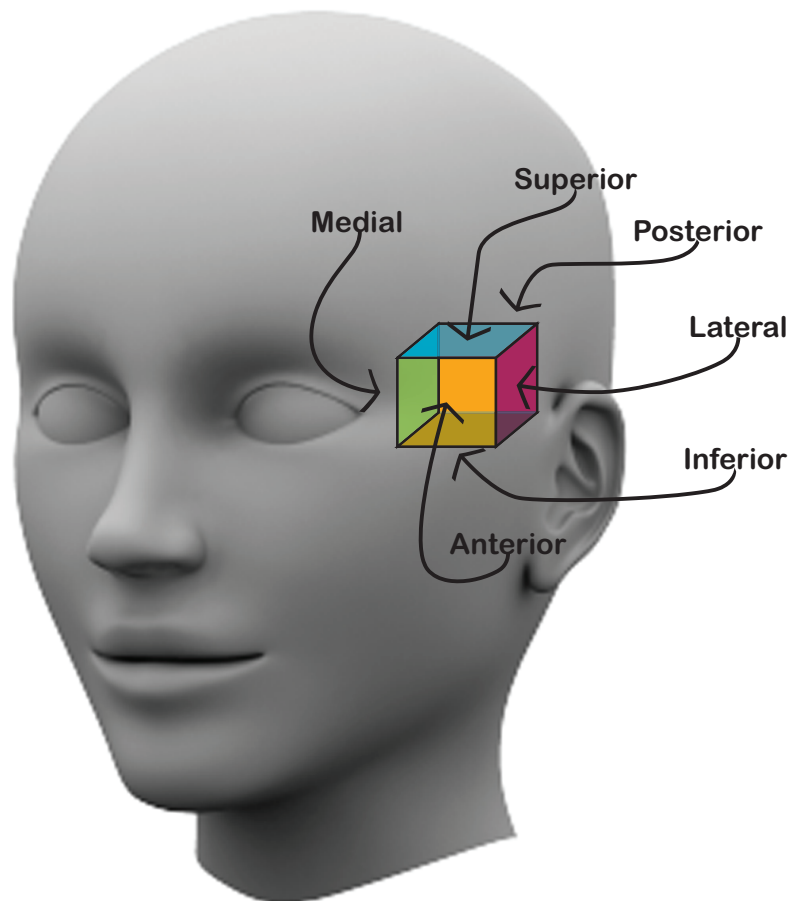


Figure B.1: 3D model of the human head with a cube that describes the six different anatomical terms used. The opposite surface relations are: Superior (Blue)-Inferior (Brown), Medial (Green)-(Right or Left, left in this case) Lateral (Purple), Anterior (Yellow)-Posterior (Red)

Appendix C

BiCMOS process layout

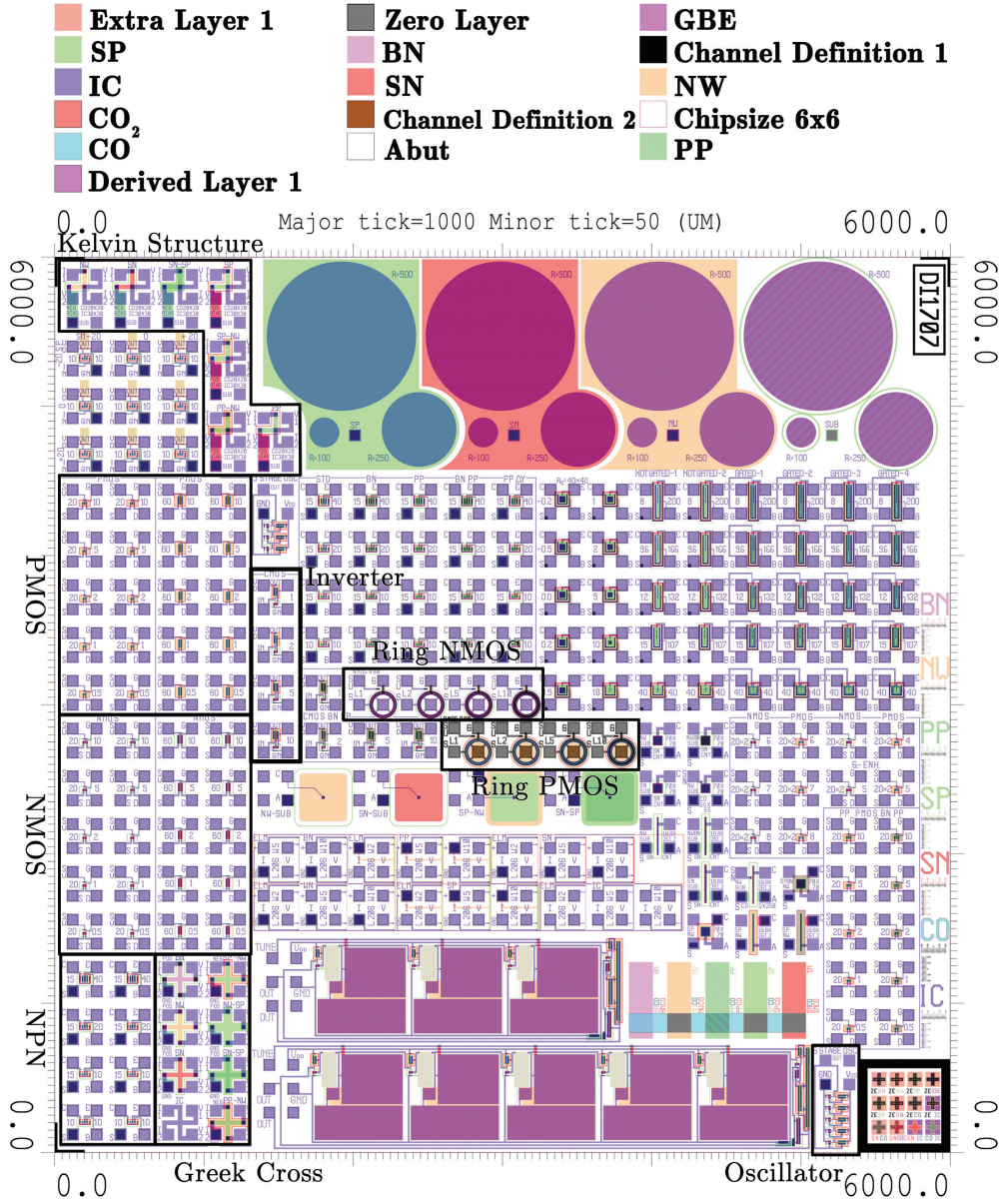


Figure C.1: The complete layout of one of the dies on the BiCMOS wafer. A die is $6 \times 6 \text{mm}^2$ and the regular pattern of the contact pads makes it easy to do automated measurements with a probe station.

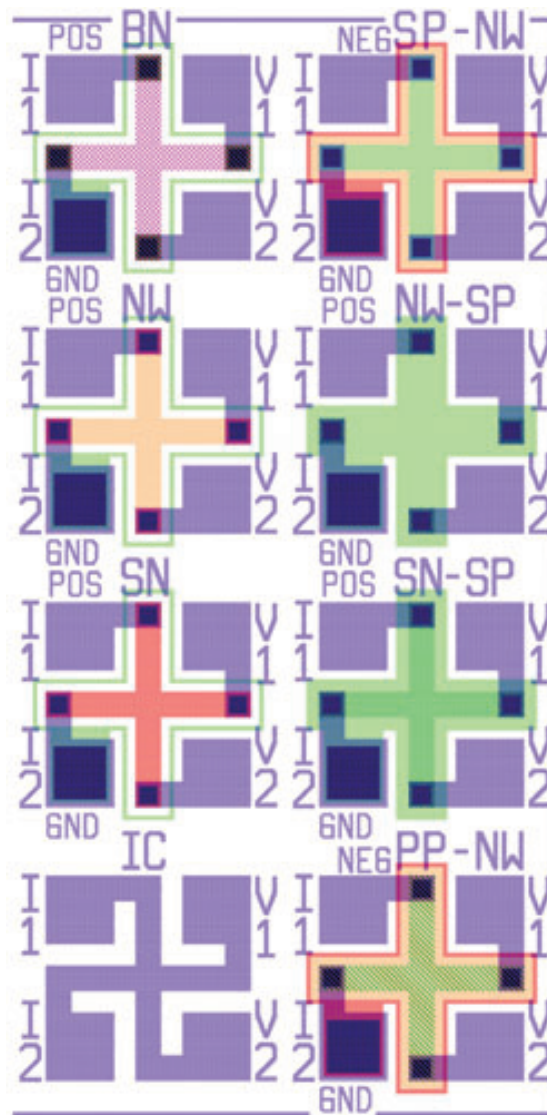


Figure C.2: Greek Cross

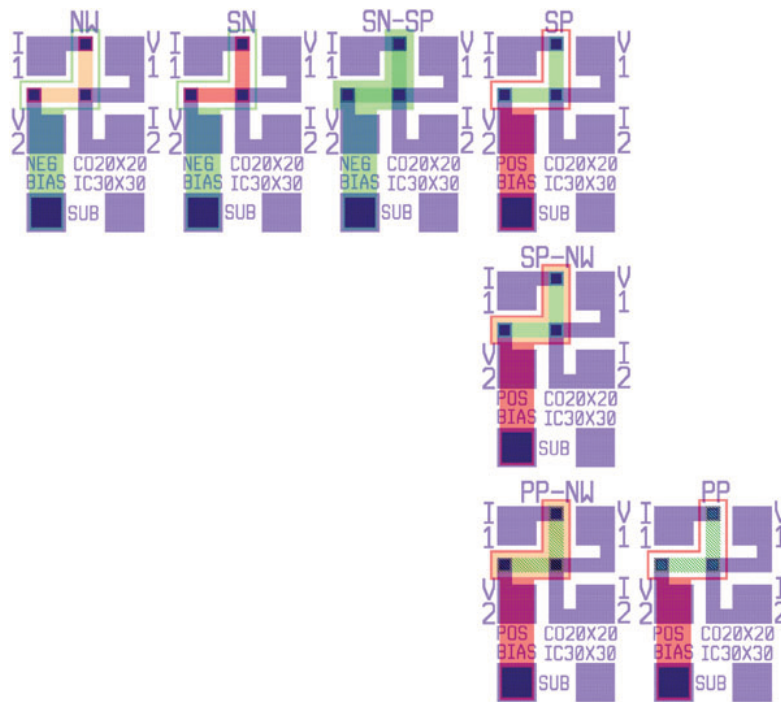


Figure C.3: Kelvin structures for contact resistance measurements

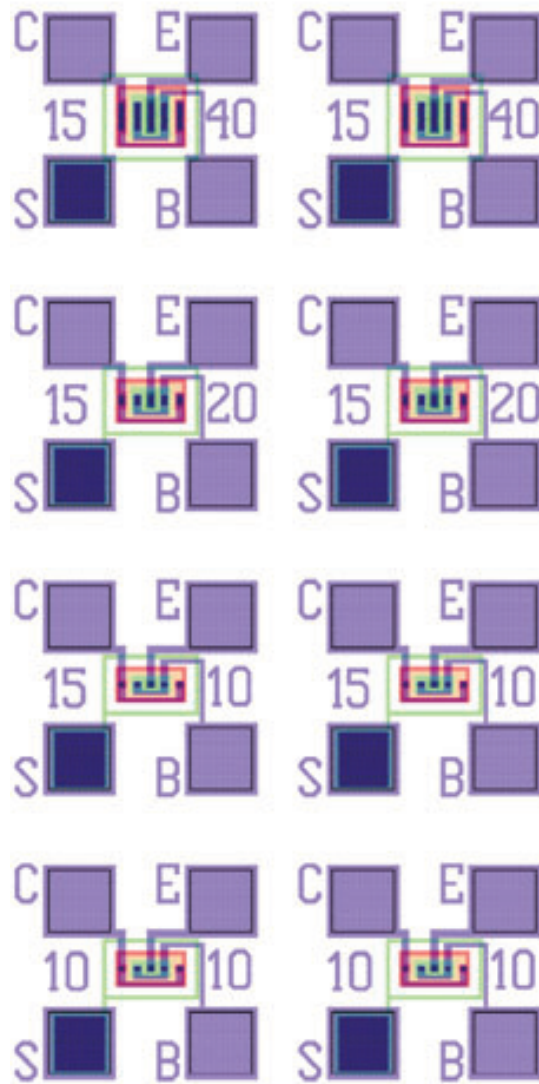


Figure C.4: Bipolar npn transistor

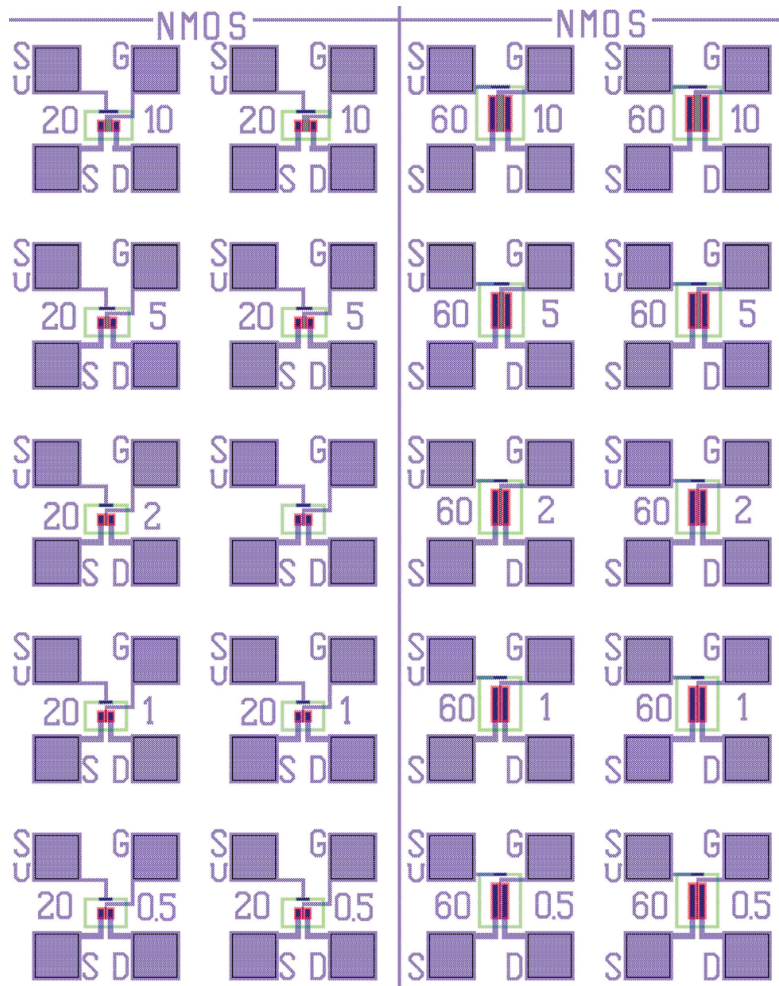


Figure C.5: NMOS transistors

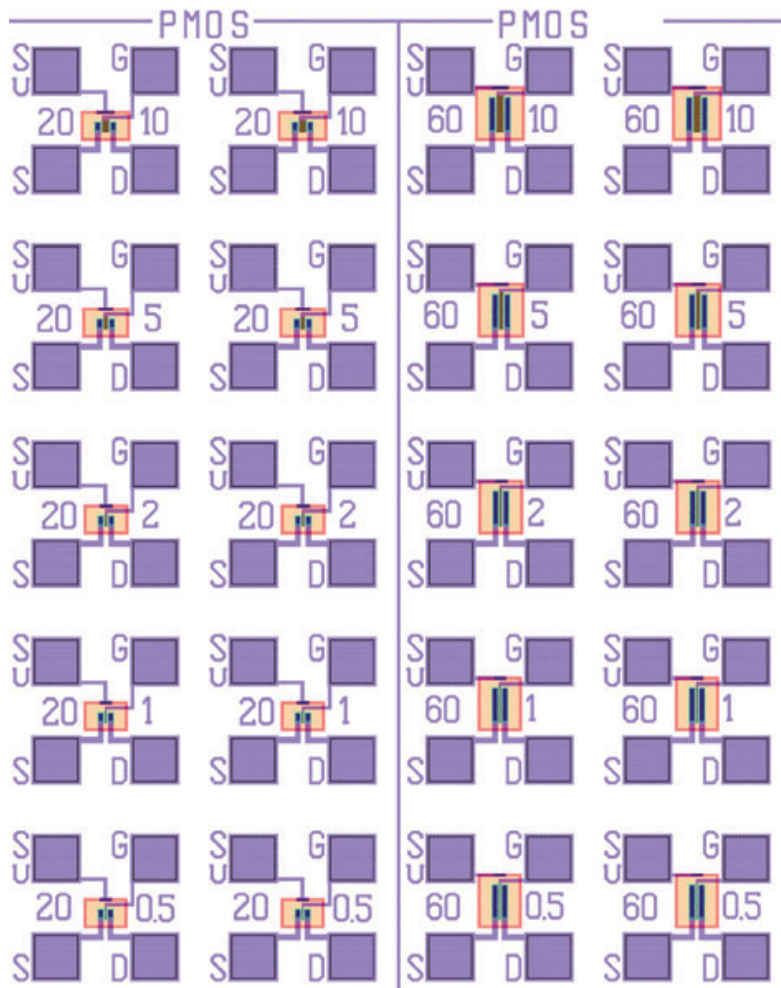


Figure C.6: PMOS transistors

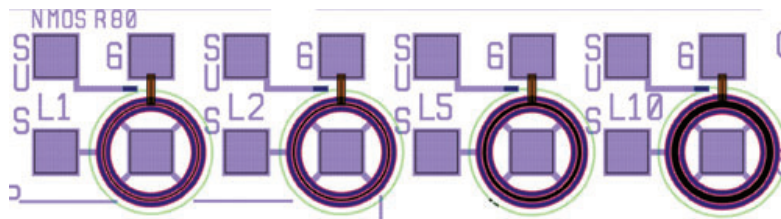


Figure C.7: Ring NMOS transistors

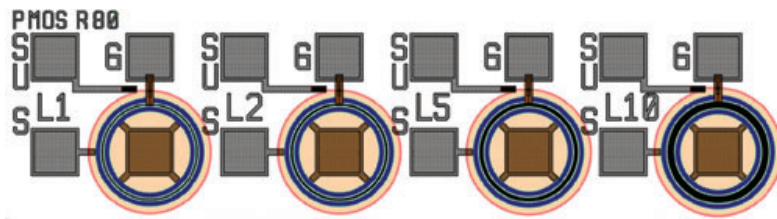


Figure C.8: Ring PMOS transistors

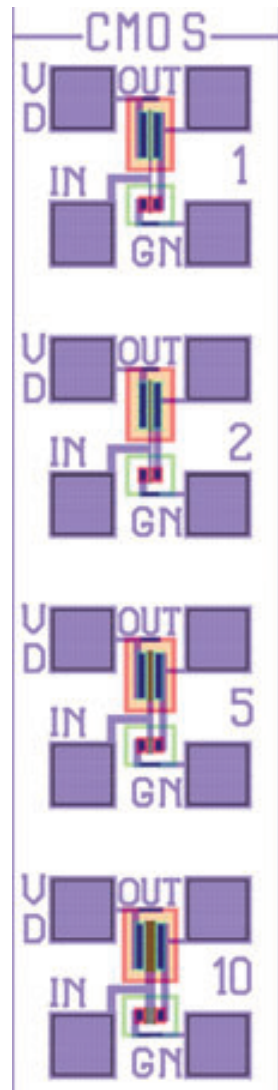


Figure C.9: Inverters

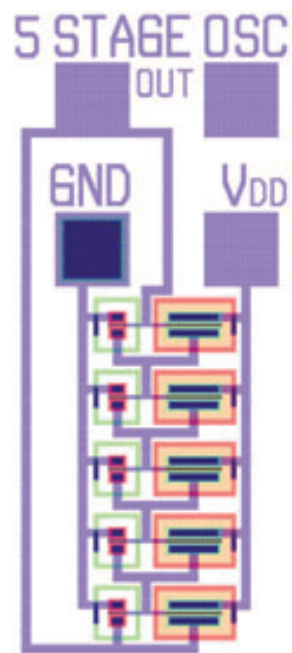
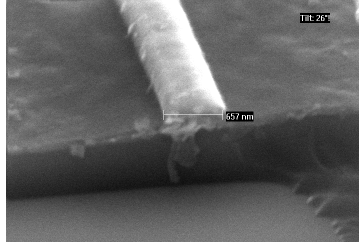


Figure C.10: 5 stage oscillator

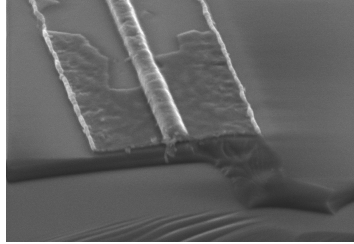
Appendix D

Additional figures for chapter 4

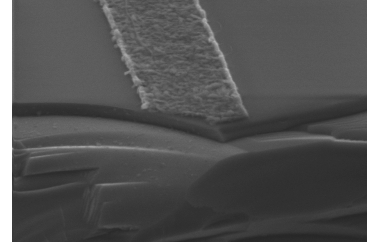
D.1 Al-TiN delamination



(a) SEM picture of an Al line covered with TiN. The Al should be $5\mu\text{m}$ wide, but is just 657nm .



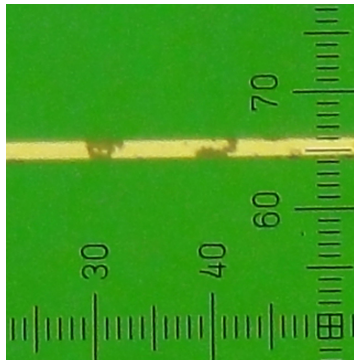
(b) Zoomed out version of (a). It shows the delamination of the TiN.



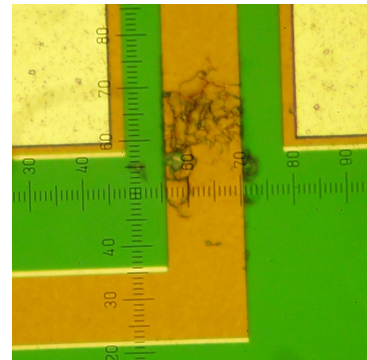
(c) This SEM picture should show an Al line of $1\mu\text{m}$ wide covered in TiN, but the Al is not there and the TiN is delaminated on some places (not in this picture)



(d) Regular microscope picture of the Al line that should be $5\mu\text{m}$ wide (black line in the middle, which in the top picture is visible on the right and in the bottom picture on the left), but is smaller and the TiN is severely damaged.



(e) Picture of the line that should contain a $1\mu\text{m}$ Al line, but is not there.



(f) A piece of the 'Greek cross' that shows some cracks in the TiN

Figure D.1: Pictures of the Al-TiN wafer that shows some adhesion problems

D.2 TCR graphs

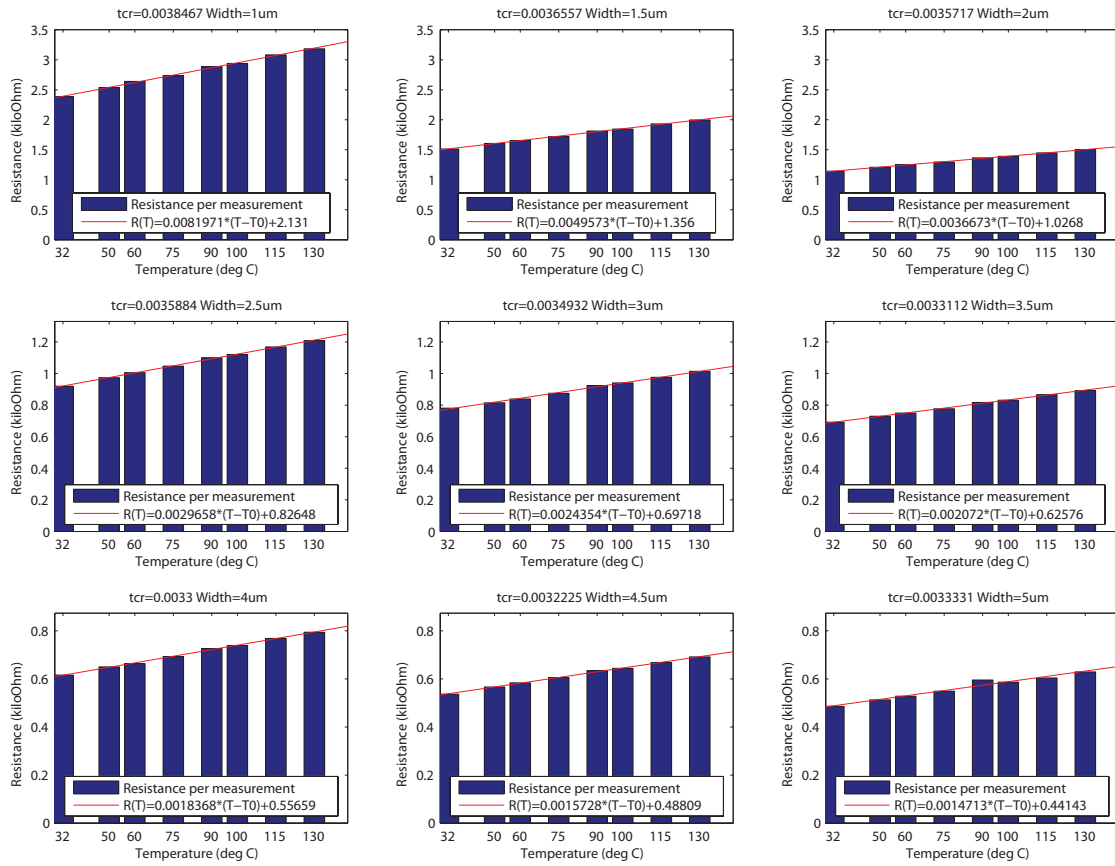


Figure D.2: The TCR of Aluminium test die number 2

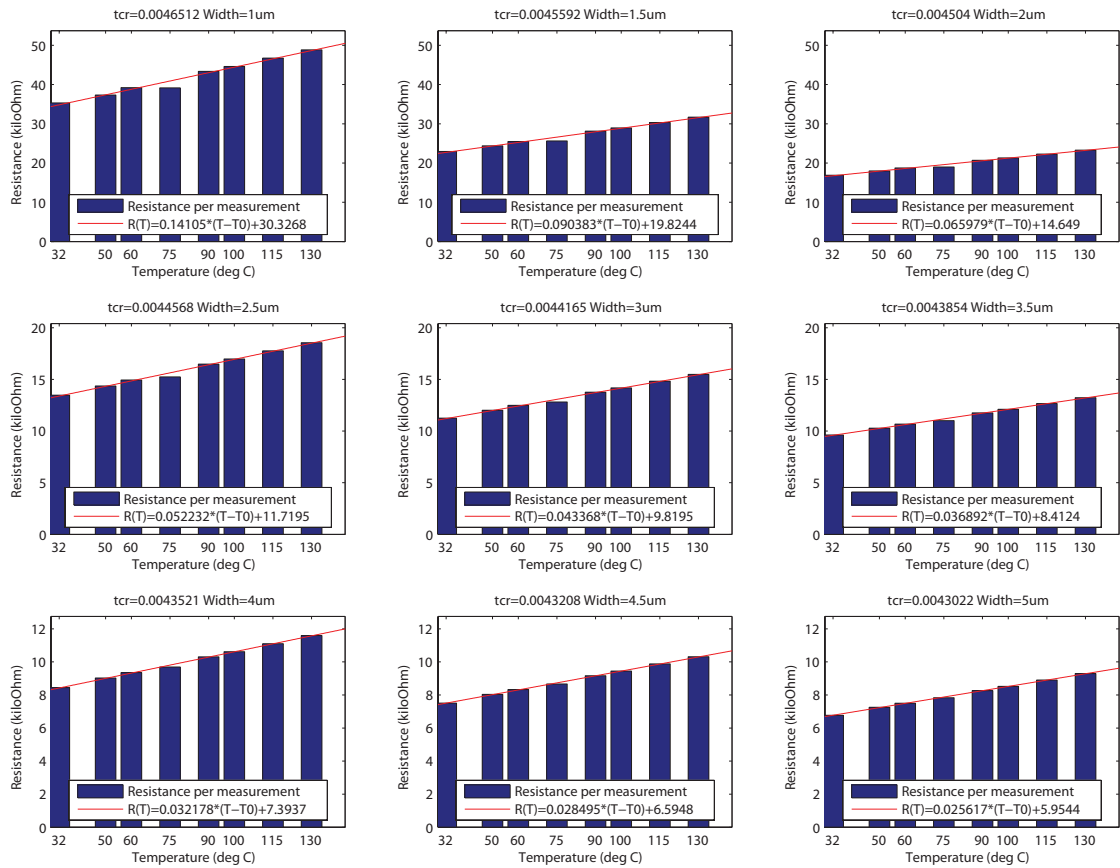


Figure D.3: The TCR of Titanium test die number 1

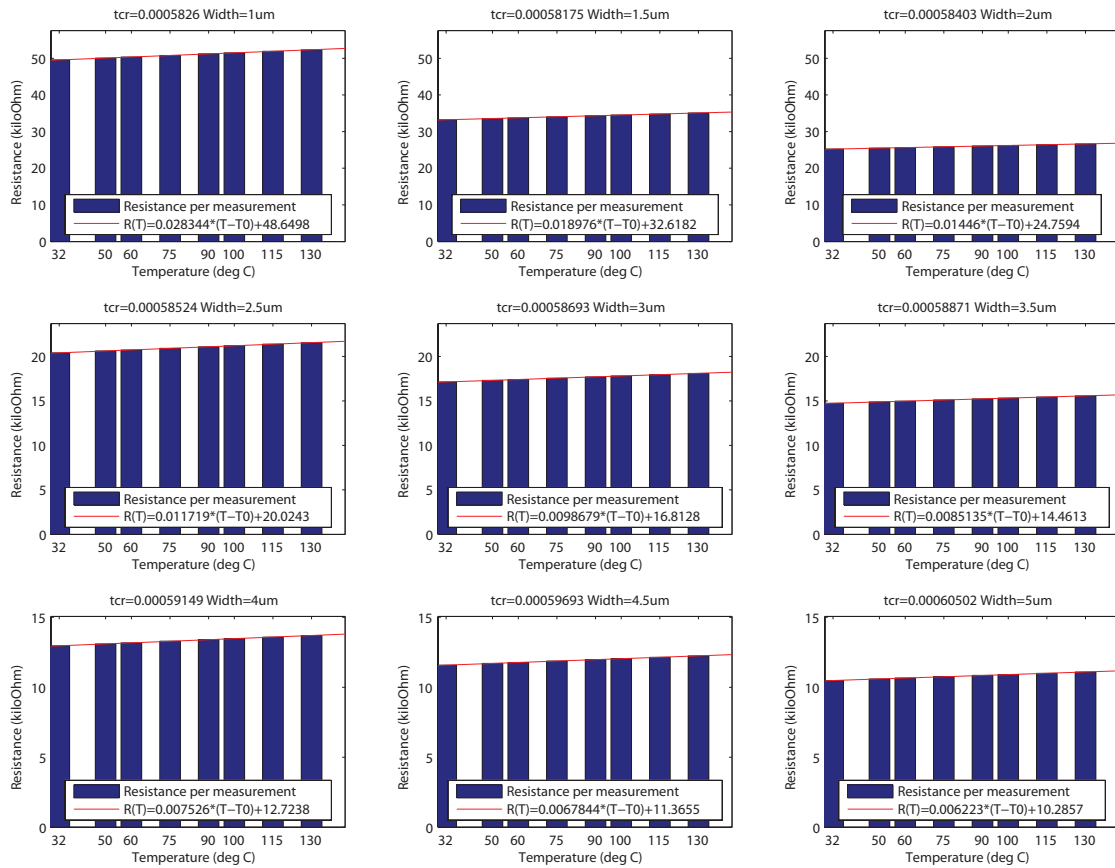


Figure D.4: The TCR of a Titanium Nitride test die

D.3 Electromigration

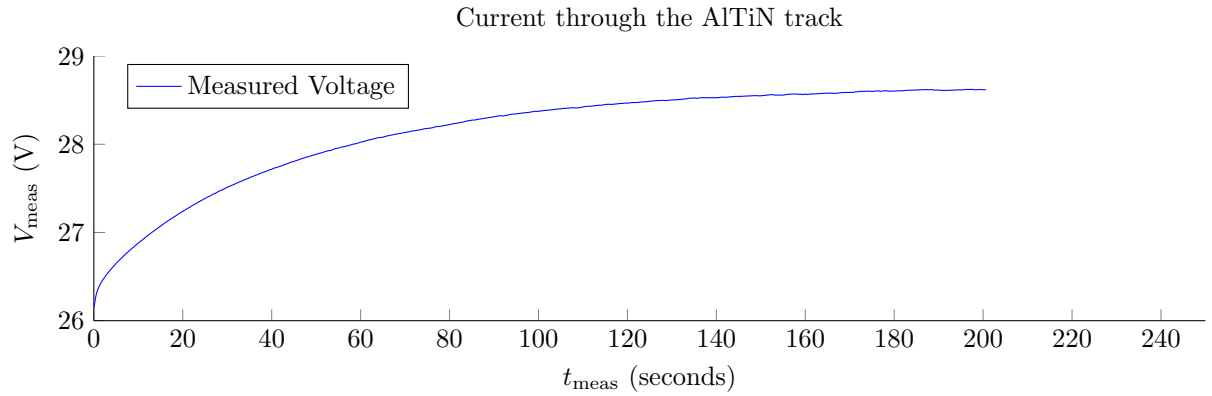


Figure D.5: The rise in potential due to self-heating of the widest $5\mu\text{m}$ Al-TiN track. A current of 30mA was supplied to this track.

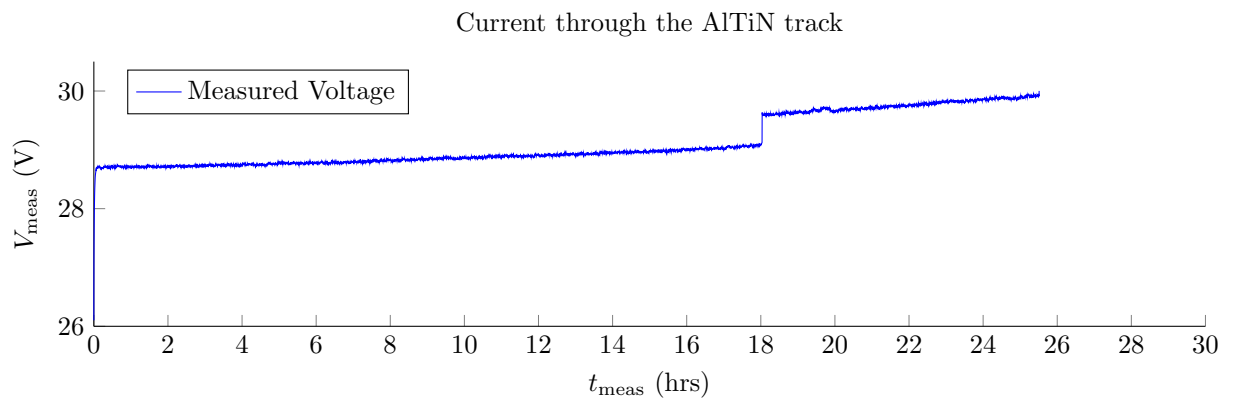


Figure D.6: The potential of the widest $5\mu\text{m}$ Al-TiN track over time. A current of 30mA was supplied to this track.

D.4 Endurance test

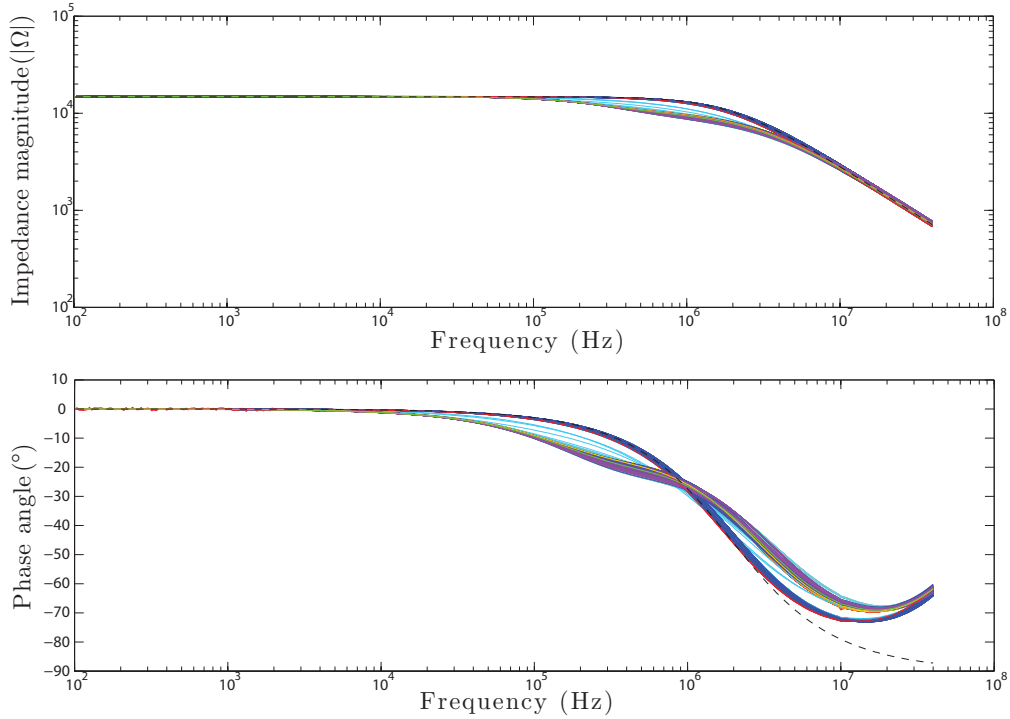


Figure D.7: Bode plot of all 664 measurement steps of a Titanium Nitride track of $3.5\mu\text{m}$ wide which is exposed to saline solution. Every 5 minutes a measurement was done during 8 days. The red line marks the first measurement and the last is purple, like shown in figure D.8. The saline solution was added after the first measurement. The glass container got empty during the test (after 3 days), but was filled up after 6 days. The empty period is marked by the dark blue lines and the light blue lines mark the almost empty period. The dashed line is the modelled resistor with capacitor in parallel, like in figure 4.19

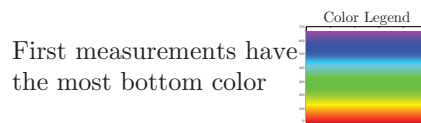
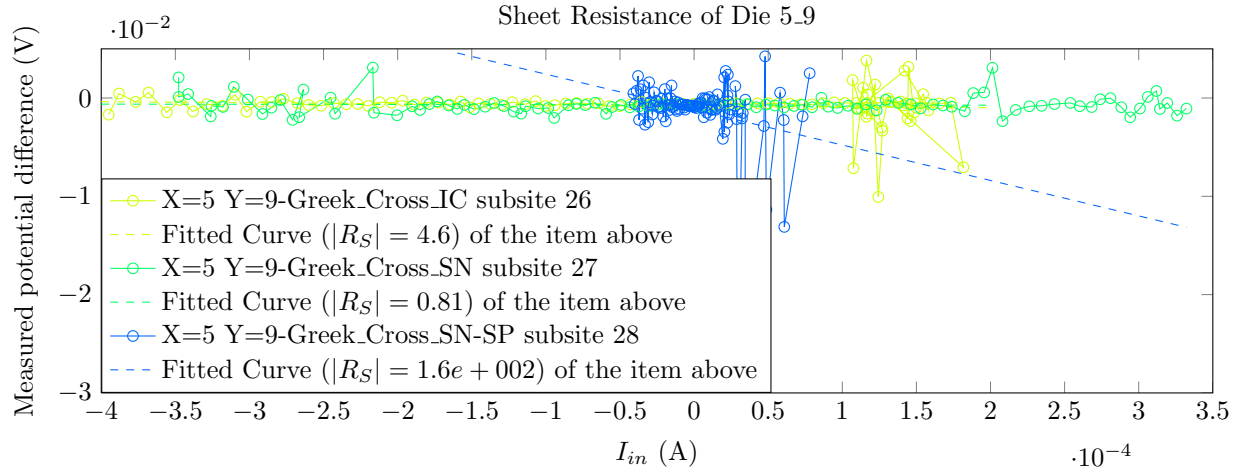
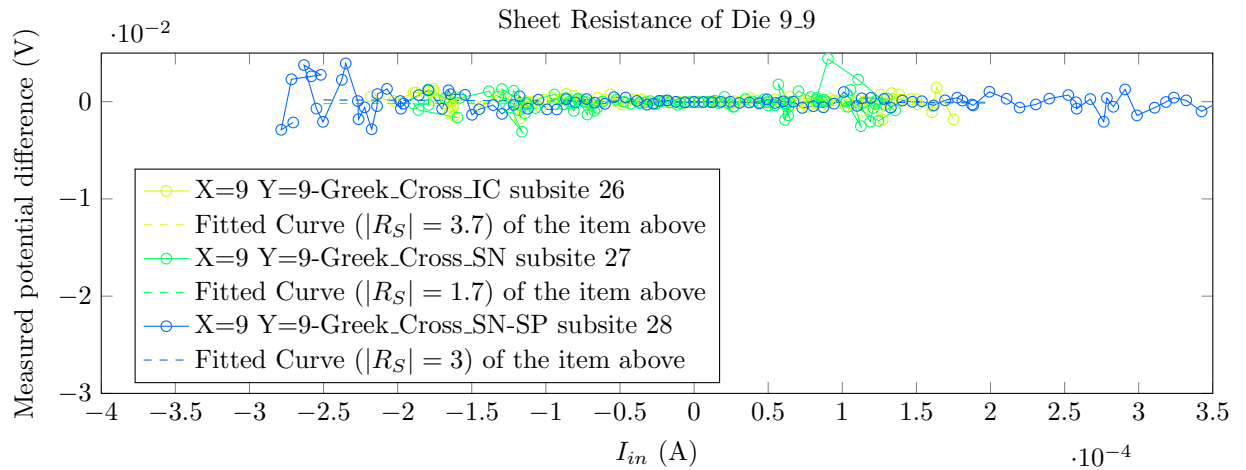


Figure D.8: Legend of D.7

D.5 BiCMOS

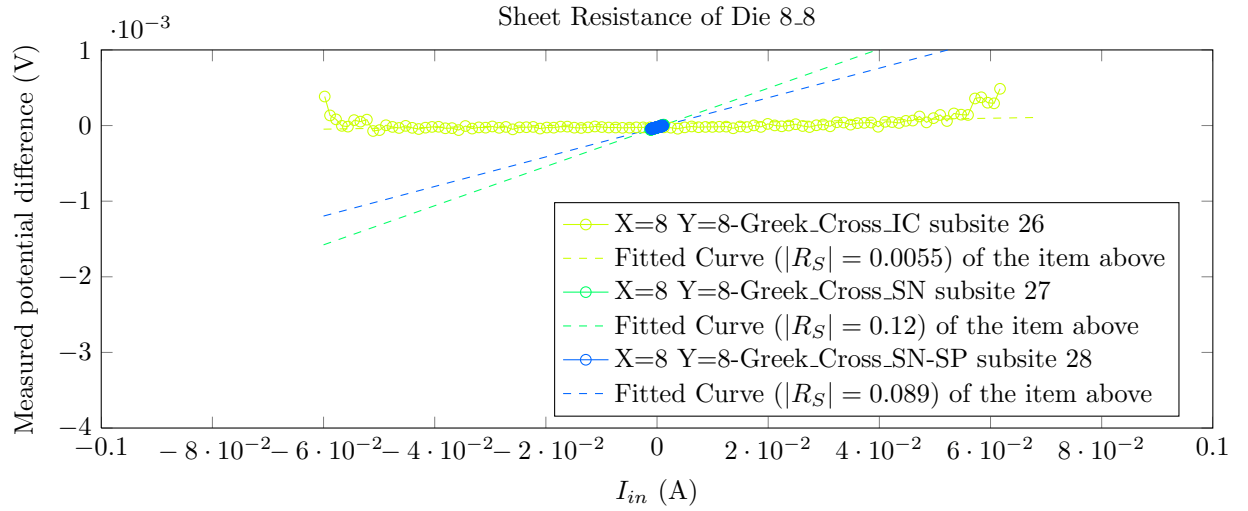


(a) Sheet Resistance Measurements of the die at coordinate $x=5$ and $y=9$ of a Titanium Nitride Wafer before annealing.

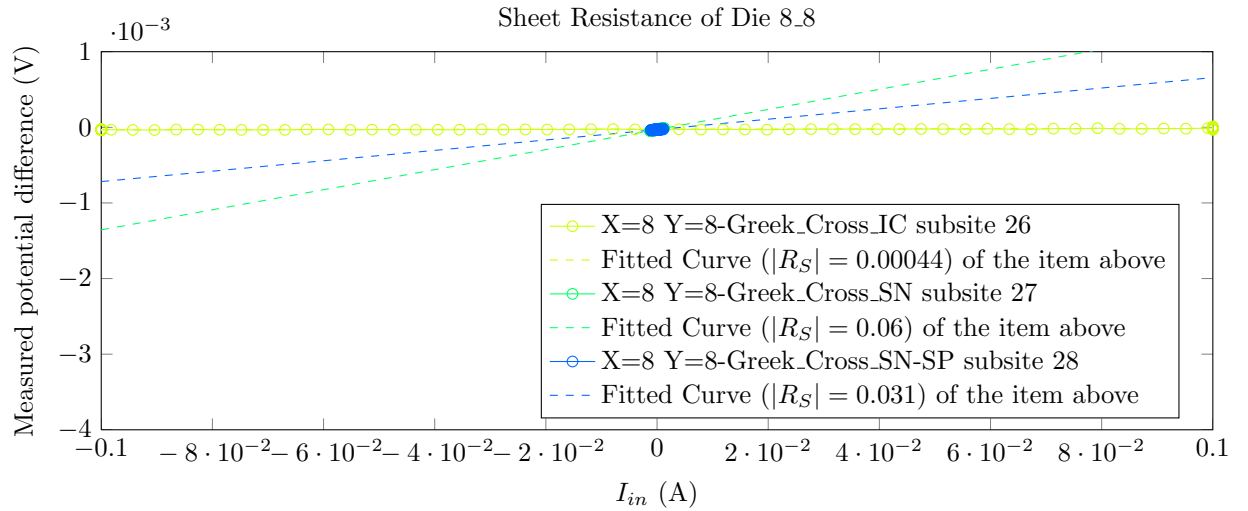


(b) Sheet Resistance Measurements of the die at coordinate $x=9$ and $y=9$ of a Titanium Nitride Wafer after its first annealing step. Note: The fit lines are hidden behind the measurement data.

Figure D.9: Sheet Resistance Measurements of titanium nitride dies before and after annealing

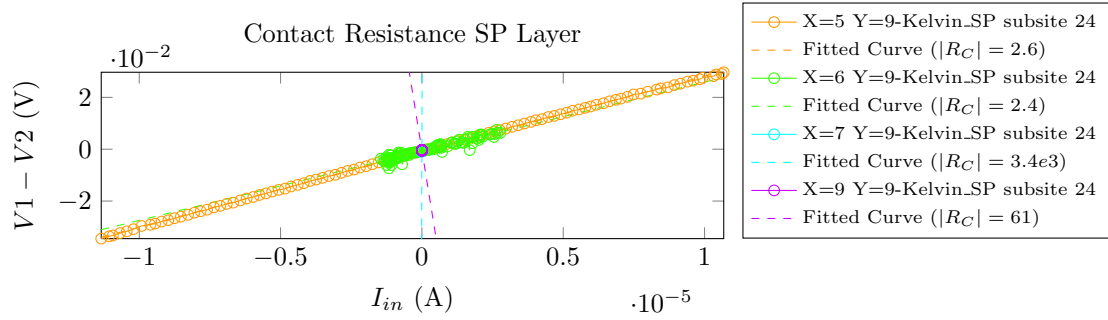


(a) Sheet Resistance Measurements of the die at coordinate $x=8$ and $y=8$ of an Aluminium Wafer before annealing.

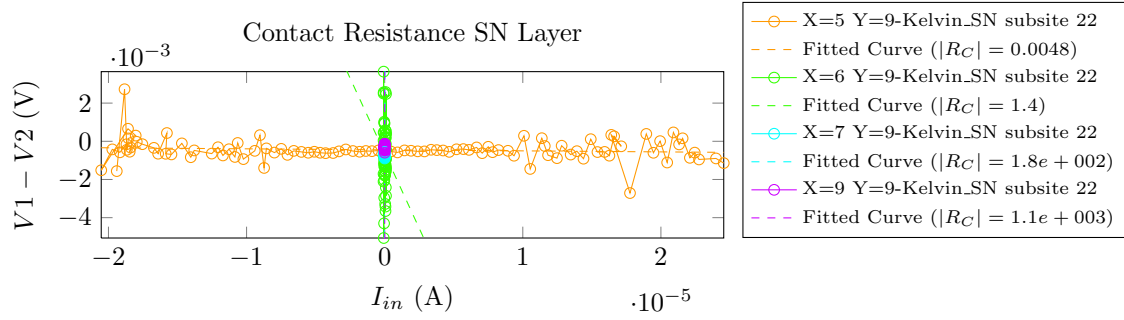


(b) Sheet Resistance Measurements of the die at coordinate $x=8$ and $y=8$ of a Aluminium Wafer after its annealing step.

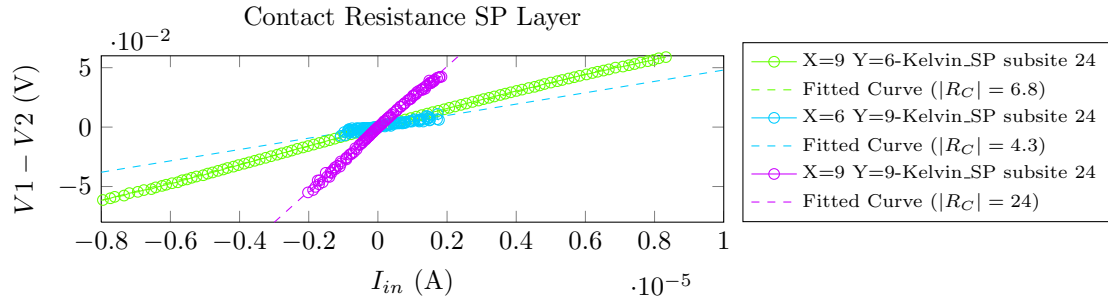
Figure D.10: Sheet Resistance Measurement of some Aluminium dies before and after annealing



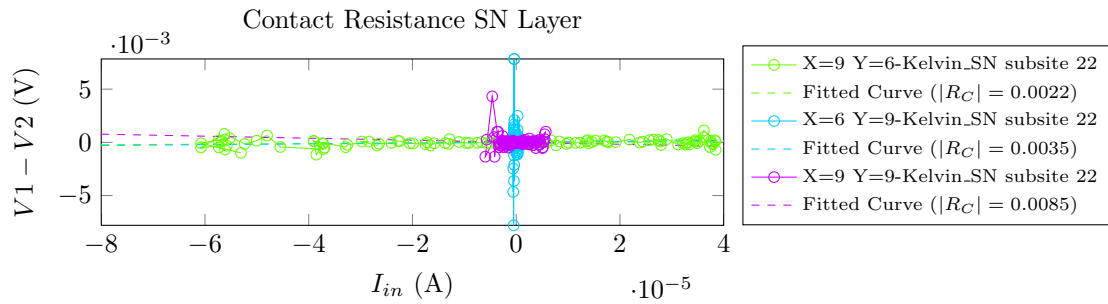
(a) Contact resistance of the TiN to the SP layer before annealing



(b) Contact resistance of the TiN to the SN layer before annealing

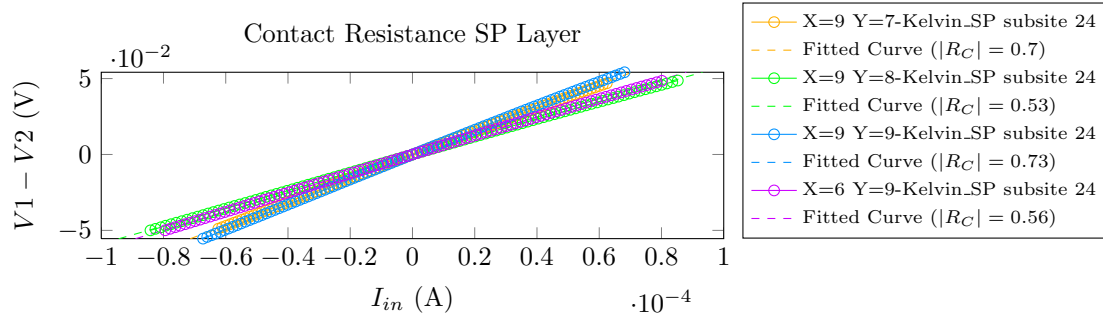


(c) Contact resistance of the TiN to the SP layer after annealing

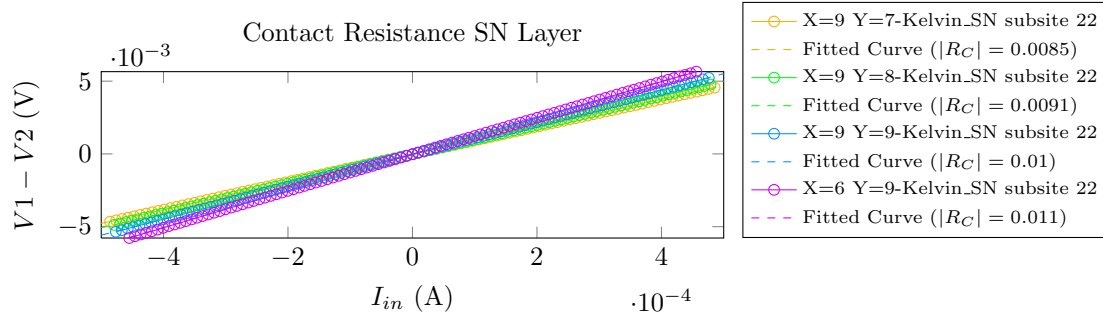


(d) Contact resistance of the TiN to the SN layer after annealing

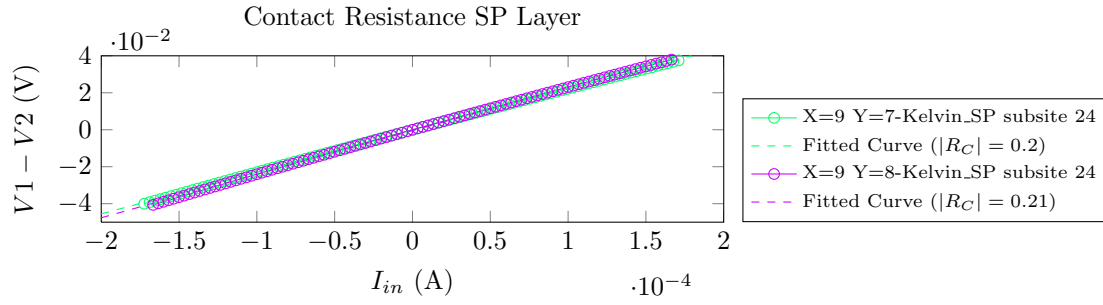
Figure D.11: Contact resistance measurements of titanium nitride to the SN and SP layer



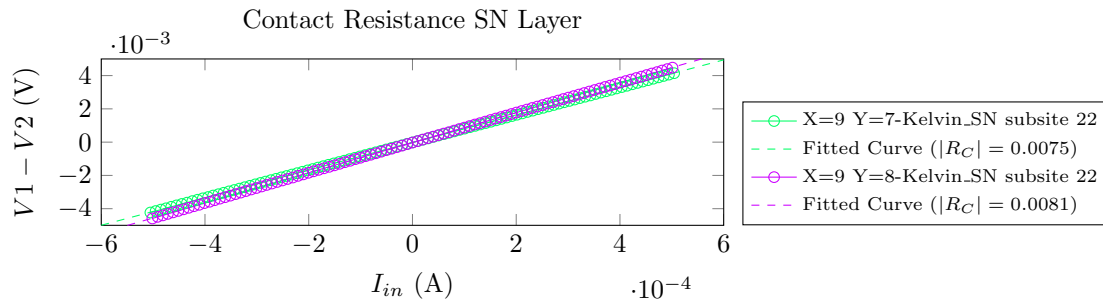
(a) Contact resistance of the aluminium to the SP layer before annealing



(b) Contact resistance of the aluminium to the SN layer before annealing



(c) Contact resistance of the aluminium to the SP layer after annealing



(d) Contact resistance of the aluminium to the SN layer after annealing

Figure D.12: Contact resistance measurements of aluminium to the SN and SP layer

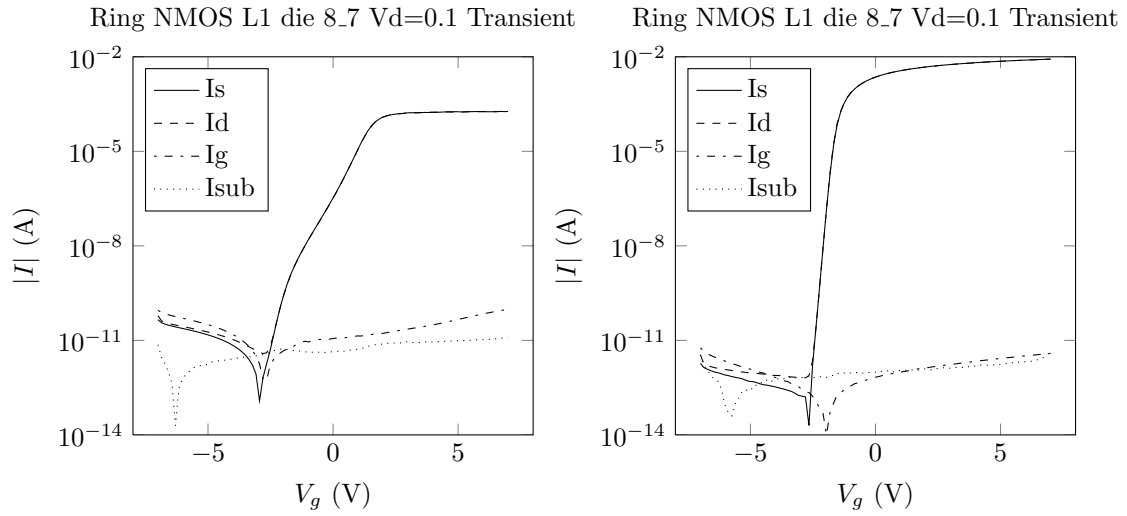


Figure D.13: Gate voltage V_G sweeps of the NMOS ring transistor

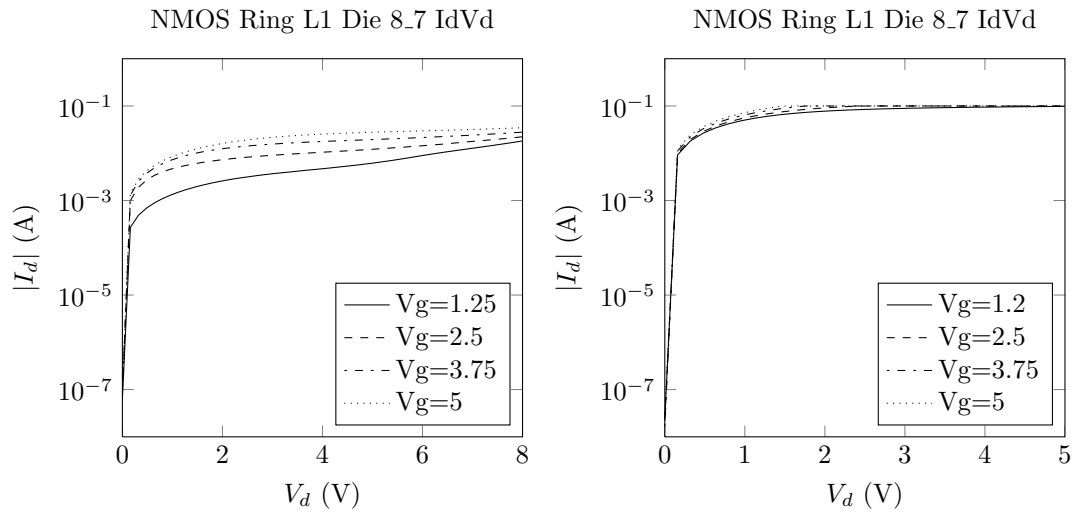


Figure D.14: The drain current I_d for a drain voltage V_d and gate voltage V_g sweep of the NMOS Ring transistor with a gate length of $1\mu\text{m}$ (L1)

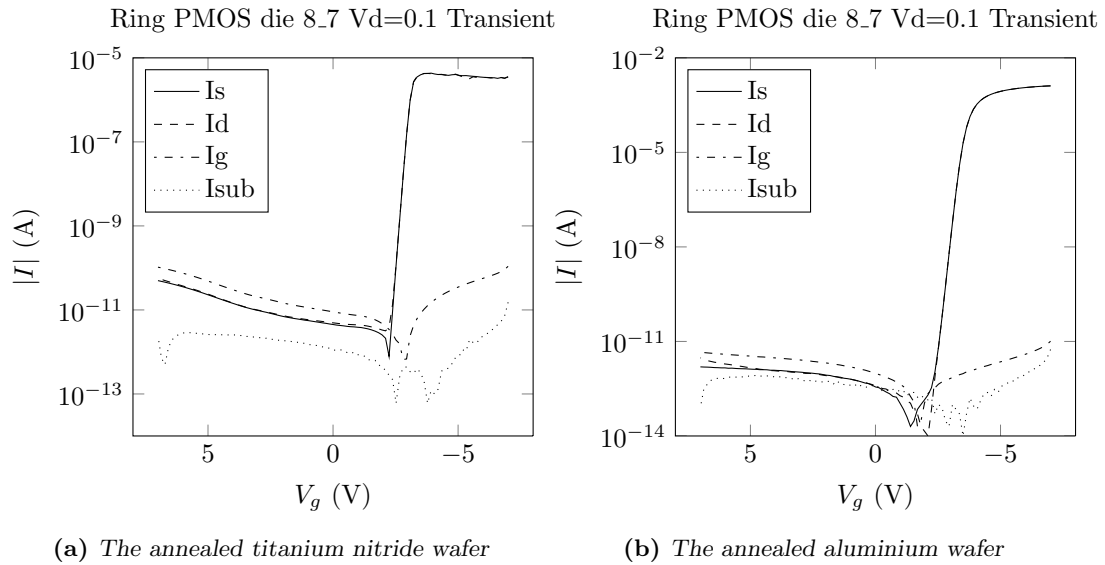


Figure D.15: Transient plots of the ring PMOS transistor with a gate length of $1\mu\text{m}$ (L1)

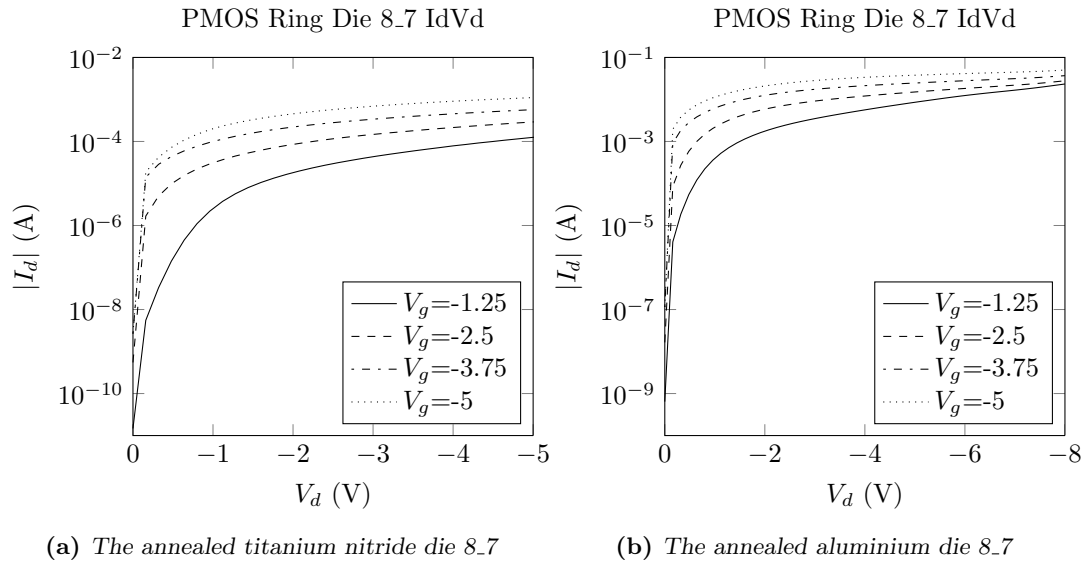


Figure D.16: The drain current I_d for a drain voltage V_d and gate voltage V_g sweep of the ring PMOS transistor with a gate length of $1\mu\text{m}$ (L1)

Bibliography

- [1] N. Bauman and H. Hetherington, “Hearing Aid Museum,” 2012.
- [2] G. Clark, *Cochlear implants : fundamentals and applications*. New York: Springer-Verlag New York, Inc., 1 ed., 2003.
- [3] H. Gray, *Anatomy of the Human Body*. New York: Bartleby.com, Inc, 20 ed., 2000.
- [4] B. H. Tortora, Gerard J;Derrickson, *Principles of Anatomy and Physiology Volume 1*. John Wiley & Sons, (Asia) Pte Ltd., 12 ed., 2009.
- [5] P. Kumar and M. Clark, *Clinical Medicine*. London: Elsevier Ltd., 7 ed., 2009.
- [6] A. N. Salt, “Cochlear Fluids Composition,” 2013.
- [7] A. R. Moller, *Cochlear and brainstem implants*. Richardson, Texas, USA: S. Karger AG, 1 ed., 2006.
- [8] MED-EL Website, “Cochlear Implants for Hearing Loss — MED-EL,” 2013.
- [9] S. F. Cogan, “Neural stimulation and recording electrodes.,” *Annual review of biomedical engineering*, vol. 10, pp. 275–309, Jan. 2008.
- [10] B. Lithgow, “Cochlear implant threshold changes at high electric stimulus pulse rates,” in *Proceedings of the 2nd International Conference on Bioelectromagnetism (Category Number 98TH8269)*, (Caulfield), pp. 117–118, IEEE, 1998.
- [11] B. S. Wilson, “Cochlear implants: Current designs and future possibilities,” *The Journal of Rehabilitation Research and Development*, vol. 45, pp. 695–730, Dec. 2008.
- [12] D. Zhou and R. Greenberg, “Electrochemical characterization of titanium nitride micro-electrode arrays for charge-injection applications,” in *Proceedings of the 25th Annual International Conference of the IEEE Engineering in Medicine and Biology Society (IEEE Cat. No.03CH37439)*, (New York, NY), pp. 1964–1967, IEEE, 2003.
- [13] M. Patan, T. Shah, and M. Sahin, “Charge injection capacity of TiN electrodes for an extended voltage range.,” in *Annual International Conference of the IEEE Engineering in Medicine and Biology Society.*, vol. 1, (New York, NY), pp. 890–892, IEEE, Jan. 2006.
- [14] N. P. Aryan, M. I. H. B. Asad, C. Brendler, S. Kibbel, G. Heusel, and A. Rothermel, “In vitro study of titanium nitride electrodes for neural stimulation.,” *Conference proceedings : ... Annual International Conference of the IEEE Engineering in Medicine and Biology Society. IEEE Engineering in Medicine and Biology Society. Conference*, vol. 2011, pp. 2866–9, Jan. 2011.

- [15] C. Nunes Kirchner, K. H. Hallmeier, R. Szargan, T. Raschke, C. Radehaus, and G. Wittstock, "Evaluation of Thin Film Titanium Nitride Electrodes for Electroanalytical Applications," *Electroanalysis*, vol. 19, pp. 1023–1031, May 2007.
- [16] J. J. Briaire, *Cochlear Implants From Model to Patients*. 2008.
- [17] P. J. Abbas, C. J. Brown, and C. P. Etlar, "Electropysiology and Device Telemetry," in *Cochlear Implants* (S. B. Waltzman and J. T. J. Roland, eds.), ch. 8, pp. 96–109, New York: Thieme Medical Publishers, Inc, 2 ed., 2006.
- [18] Fujifilm Electronic Materials, "Polyamic Acid. Durimide ® 100," 2012.
- [19] J. T. J. Roland, T. C. Huang, and A. J. Fishman, "Cochlear Implant Electrode History, Choices, and Insertion Techniques," in *Cochlear Implants* (S. B. Waltzman and J. T. J. Roland, eds.), ch. 9, pp. 110–125, New York: Thieme Medical Publishers, Inc, 2 ed., 2006.
- [20] P. J. Rousche, D. S. Pellinen, D. P. Pivin, J. C. Williams, R. J. Vetter, and D. R. Kipke, "Flexible polyimide-based intracortical electrode arrays with bioactive capability.," *IEEE transactions on bio-medical engineering*, vol. 48, pp. 361–71, Mar. 2001.
- [21] R. A. Serway, *Principles of Physics*. Fort Worth, Texas: London: Saunders College Pub, 2 ed., 1998.
- [22] M. Marelli, G. Divitini, C. Collini, L. Ravagnan, G. Corbelli, C. Ghisleri, A. Gianfelice, C. Lenardi, P. Milani, and L. Lorenzelli, "Flexible and biocompatible microelectrode arrays fabricated by supersonic cluster beam deposition on SU-8," *Journal of Micromechanics and Microengineering*, vol. 21, p. 045013, Apr. 2011.
- [23] S. a. Boppart, B. C. Wheeler, and C. S. Wallace, "A flexible perforated microelectrode array for extended neural recordings.," *IEEE transactions on bio-medical engineering*, vol. 39, pp. 37–42, Jan. 1992.
- [24] A. L. Owens, T. J. Denison, H. Versnel, M. Rebbert, M. Peckerar, and S. A. Shamma, "Multi-electrode array for measuring evoked potentials from surface of ferret primary auditory cortex.," *Journal of neuroscience methods*, vol. 58, pp. 209–20, May 1995.
- [25] M. Peckerar, S. a. Shamma, M. Rebbert, J. Kosakowski, and P. Isaacson, "Passive micro-electrode arrays for recording of neural signals: A simplified fabrication process," *Review of Scientific Instruments*, vol. 62, no. 9, p. 2276, 1991.
- [26] T. Taychatanapat (CCMR), "<http://www.ccmr.cornell.edu/facilities/winners07feb/thiti.html>," 2007.
- [27] D. Pierce and P. Brusius, "Electromigration: A review," *Microelectronics Reliability*, vol. 37, pp. 1053–1072, July 1997.
- [28] H. Veendrick, *Deep-Submicron CMOS ICs*. Eindhoven, Netherlands: Kluwer BedrijfsInformatie b.v. - Deventer, the Netherlands, 1 ed., 1998.
- [29] I. a. Blech, "Electromigration in thin aluminum films on titanium nitride," *Journal of Applied Physics*, vol. 47, no. 4, p. 1203, 1976.
- [30] J. Black, "Electromigration-A brief survey and some recent results," *IEEE Transactions on Electron Devices*, vol. 16, pp. 338–347, Apr. 1969.

- [31] a. Kusy, "An equivalent network for resistance and temperature coefficient of resistance versus temperature and composition of thick resistive films," *Journal of Applied Physics*, vol. 62, no. 4, p. 1324, 1987.
- [32] P. Wangemann, "Supporting sensory transduction: cochlear fluid homeostasis and the endocochlear potential.," *The Journal of physiology*, vol. 576, pp. 11–21, Oct. 2006.
- [33] U. van Rienen, J. Flehr, U. Schreiber, S. Schulze, U. Gimsa, W. Baumann, D. G. Weiss, J. Gimsa, R. Benecke, and H.-W. Pau, "Electro-Quasistatic Simulations in Bio-Systems Engineering and Medical Engineering," *Advances in Radio Science*, vol. 3, pp. 39–49, May 2005.
- [34] D. B. Hibbert, K. Weitzner, and P. Carter, "Voltammetry of Platinum in Artificial Perilymph Solution," *Journal of The Electrochemical Society*, vol. 148, no. 1, p. E1, 2001.
- [35] R. G. Compton and C. E. Banks, *Understanding Voltammetry*. London: Imperial College Press, 2 ed., 2011.
- [36] DrHuang.com, "www.kensingtonwellbeing.com.au/science/chemistry/electrochemistry," 2009.
- [37] CPWR - The Center for Construction Research and Training, "www.silica-safe.org," 2012.
- [38] N. Lawand, P. French, J. Briaire, and J. Frijns, "Thin Titanium Nitride Films Deposited using DC Magnetron Sputtering used for Neural Stimulation and Sensing Purposes," *Procedia Engineering*, vol. 47, pp. 726–729, Jan. 2012.
- [39] S. Smith, *Sheet Resistance and Electrical Linewidth Test Structures for Semiconductor Process Characterisation*. Doctor of philosophy, University of Edinburgh, 2003.
- [40] N. S. Lawand, J. V. Driel, and P. J. French, "Electric Field Density Distribution for Cochlear Implant Electrodes," in *2012 COMSOL Conference in Milan*, (Milan), pp. 1–4, Comsol, 2012.
- [41] L. Wolgemuth, "Parylenes : Advanced Polymers for Medical Devices," in *Medical Plastics 2006 Conference in Copenhagen, Denmark*, (Copenhagen), pp. 1–4, Hexagon, 2006.
- [42] J. Kelly, "Improving Chip Board Assembly," 2004.
- [43] N. Stavitski, S. Member, J. H. Klootwijk, H. W. V. Zeijl, B. K. Boksteen, A. Y. Kovalgin, and R. A. M. Wolters, "Cross-Bridge Kelvin Resistor (CBKR) Structures for Measurement of Low Contact Resistances," in *10th Annual Workshop on Semiconductor Advances for Future Electronics and Sensors (SAFE)*, (Veldhoven), pp. 551–554, SAFE, 2007.
- [44] R. C. Jaeger, *Introduction to Microelectronic Fabrication*. Auburn, Alabama: Prentice Hall, 2 ed., 2001.
- [45] M. Danek, M. Liao, J. Tseng, K. Littau, D. Saigal, H. Zhang, R. Mosely, and M. Eizenberg, "Resistivity reduction and chemical stabilization of organometallic chemical vapor deposited titanium nitride by nitrogen rf plasma," *Applied Physics Letters*, vol. 68, no. 7, p. 1015, 1996.
- [46] W. Ngamkham, M. N. van Dongen, and W. A. Serdijn, "Biphasic stimulator circuit for a wide range of electrode-tissue impedance dedicated to cochlear implants," in *ISCAS 2012*, (Seoul, Korea), pp. 1083–1086, IEEE, 2012.

- [47] R. C. Weast, "The Elements and Organic Compounds," in *CRC Handbook of Chemistry and Physics* (M. J. Astle and W. H. Beyer, eds.), ch. B, Boca Raton, Florida: CRC Press, Inc., 67 ed., 1986.